Environmental selection effects of Sunyaev Zel'dovich selected clusters of galaxies and instrumentation dedicated to the photometric study of large scale structure

Ralf Kosyra

München 2016

Environmental selection effects of Sunyaev Zel'dovich selected clusters of galaxies and instrumentation dedicated to the photometric study of large scale structure

Ralf Kosyra

Dissertation
an der Fakultät für Physik
der Ludwig–Maximilians–Universität
München

vorgelegt von
Ralf Kosyra
aus München

München, den 04. April 2016

Erstgutachter: Prof. Dr. Ralf Bender
Zweitgutachter: Prof. Dr. Thomas Preibisch
Tag der mündlichen Prüfung: 12. Juli 2016

Contents

Zusammenfassung

Galaxienhaufen sind die massivsten und jüngsten virialisierten Objekte in unserem Universum. Das Verständnis ihrer Anzahldichte, ihrer Verteilung im Raum sowie der Struktur ihrer baryonischen und dunklen Materie ermöglicht es uns, tiefe Einblicke in die Kosmologie sowie in die Entstehungs- und Entwicklungsgeschichte der großräumigen Struktur des Universums zu gewinnen. Dies erfordert präzise Methoden und Instrumente zur Detektion und zur Massenbestimmung von Galaxienhaufen.
Diese Arbeit besteht aus zwei Teilen: der erste Teil beschäftigt sich mit der Kalibrierung des Wendelstein Wide Field Imager (WWFI) für das 2m Wendelsteinteleskop, der speziell für die Beobachtung von Galaxienhaufen entwickelt wurde. Die Beiträge meiner Arbeit zur Kalibrierung des WWFI (siehe Kapitel 3 und Kosyra et al. [2014])sind:
(i) Messung der elekronischen Systemeigenschaften wie Gain, Charge Transfer Effizienz und dem Verhalten persistenter Ladungen.
(ii) Messung der optischen Systemeigenschaften wie der Quanteneffizienz, und Bestimmung der Gesamteffizienz des Systems.
(iii) Vorhersage instrumenteller Magnituden von Sternen mit Hilfe stellarer Spektren und den Ergebnissen von (ii).
Es stellt sich heraus dass diese Art der Vorhersage instrumenteller Helligkeiten (iii) gut möglich ist. Folglich ist auch die Bestimmung von Galaxiefarben mit hinreichender Genauigkeit gewährleistet, was insbesondere für die Charakterisierung von Galaxienhaufen mit photometrischen Methoden und mittels des Gravitationslinseneffektes von entscheidender Bedeutung ist.
Der zweite Teil dieser Dissertation befasst sich mit Galaxienhaufen, die mit Hilfe des Sunyaev-Zel'dovich (SZ) Effektes detektiert wurden. Der SZ-Effekt beschreibt die spektrale Verzerrung des kosmischen Mikrowellenhintergrundes durch inverse Compton-Streuung am heißen Gas im Inneren eines Haufens. Das Ziel ist die Untersuchung möglicher umgebungsabhängiger Selektionseffekte, die die Massenbestimmung SZ-selektierter Haufen verfälschen könnten. Oben genannter Effekt könnte beispielsweise durch Strukturen entlang der Sichtlinie verursacht werden, welche das SZ-Signal verstärken. Eine weitere denkbare Ursache sind Radio-Punktquellen im Hintergrund, welche die Signalextraktion erschweren. Hierfür berechne ich die Haufen-Gruppen Zweipunkt-Korrelationsfunktion unter Verwendung eines Katologs SZ-selektierter Haufen (des *Planck* PSZ1 Union Katalogs) und eines Katalogs optisch selektierter Galaxiengruppen (des *RedMaPPer* SDSS DR8 Katalogs). Ich vergleiche die Ergebnisse mit einem Sample rein optisch selektierter Haufen sowie mit theoretischen Vorhersagen.
Gegensätzlich zur Hypothese umgebungsunabhängiger Selektion, finde ich eine durchschnittliche Korrelation für Hintergrundstrukturen von -0.049 auf Winkelskalen von $\lesssim 40'$ mit einer Signifikanz von $\sim 4\sigma$. Folglich werden *Planck*-Haufen in Regionen mit unterdurchschnittlicher Gruppendichte im Hintergrund mit höherer Wahrscheinlichkeit entdeckt. Dieser Selektionseffekt hat nahezu keine Auswirkungen auf Massenbestimmungen mittels des SZ-Effektes oder Röntgen-Beobachtungen. Allerdings beeinflusst er Messungen des schwachen Gravitationslinseneffektes, da dieser von der Summe aller Strukturen entlang der Sichtline verursacht wird.

Abstract

Clusters of galaxies are the largest and most recently formed virialized structures in the Universe. Understanding their number density, their distribution in space and the structure of their baryonic mass and dark matter allows us to use them as probes for studying cosmology as well as the evolutionary history of large scale structure. This requires reliable and accurate methods and instruments to detect them and measure their masses.
This work consists of two parts: in the first part I discuss the calibration of the Wendelstein Wide Field Imager (WWFI) for the 2m Wendelstein telescope, which is dedicated to optical observations of galaxy clusters.
My contributions to the calibration of the WWFI (see chapter 3 and Kosyra et al. [2014])are:
(i) Measurement of the electronic system parameters as the gain, charge transfer efficiency and the behavior of persistent charges.
(ii) Measurement of the optical system parameters as the quantum efficiency, and determination of the total efficiency of the system.
(iii) Prediction of instrumental magnitudes of stars using stellar spectra and the results from (ii).
I find good predictability of instrumental magnitudes using the method from (iii). Consequently, galaxy colors can also be determined accurately, which is of particular importance for characterizing galaxy clusters with photometric methods and gravitational lensing.
The second part of this dissertation is dedicated to galaxy clusters detected by the Sunyaev Zel'dovich (SZ) effect, which describes the distortion imprinted on the spectrum of the cosmic microwave background by inverse Compton scattering in the hot gas of the intra cluster medium. The main goal is to investigate potential environmental selection effects of SZ selected galaxy clusters, as these could bias mass measurements. Aforesaid effect might be caused by structures along the line of sight that add to the SZ signal, or by radio point sources in the background that complicate signal extraction. To achieve this goal, I calculate the cluster-group two point correlation function from a catalog of SZ-selected clusters (the *Planck* PSZ1 union catalog) and a catalog of optically selected groups (the *RedMaPPer* SDSS DR8 catalog). I compare the results to a pure sample of optically selected clusters, as well as to theoretical predictions. In contrast to the hypothesis of environment independent selection, I find a mean correlation for background structures of -0.049 on angular scales of $\lesssim 40'$, significantly non-zero at $\sim 4\sigma$. Consequently, *Planck* clusters are more likely to be detected in regions where the density of groups in the background is lower than average. This selection has nearly no effect on SZ or X-ray mass estimates, but does affect weak lensing measurements, as the latter is sensitive to the sum over all structures along the line of sight.

Chapter 1

Preface

Observing the night sky has ever since been a very exciting and challenging task. Humankind has been inventing tools to improve the ability to observe the celestial sphere since many centuries. First telescopes came up in the 17^{th} century during the renaissance era and played a major role in the scientific revolution. At that time, photons were still detected by the human eye, which lacks the ability to take images with long exposure times. The invention of capture media, like photographic plates in the 19^{th} century, enabled astronomers to observe even fainter objects as well as larger fields of view. In the 1990s, charge coupled devices (CCDs, invented in the 1970s) replaced photographic plates as the most commonly used detector in astronomical observations. The much higher quantum efficiency of CCDs as well as the much faster access to the results (among many other advantages) allowed astronomers to push the limit even further and to observe the most distant of extragalactic objects.

1.1 The cosmic microwave background

As we observe objects farther away with our modern instruments, we also look further into the past as the travel time of the light increases. Consequently, as we live in an expanding universe, we look at times when the extent of the Universe was much smaller than it is today, and thus, its density and temperature were much higher. Approximately 380,000 years after the *Big Bang* when the size of the Universe was less than 0.001 of its current size, the Universe became cool enough for the first neutral atoms to be

formed. As a result, photons decoupled from matter due to the lack of free electrons scattering photons. The photons from this epoch of recombination can still be observed today as the cosmic microwave background (CMB), which is isotropic at the 10^{-5} level. It has a temperature of approximately 2.7 K, resulting from the redshift due to the cosmic expansion. The small anisotropies match with what would be expected if quantum fluctuations of matter in a very small space had been blown up to the size of the Universe we observe today. These variations are the seeds for bottom-up structure formation, as additional matter is attracted to overdense regions by gravitational force, causing the inhomogeneities to grow and form first stars and later on galaxies, galaxy groups and galaxy clusters.
The latter are the central objects of interest in this dissertation. As clusters of galaxies mainly consist of dark matter, I will describe it briefly.

1.2 Dark matter and dark energy

During the last few decades, cosmologists found that baryons contribute to the energy budget of the Universe only at the 5% level [e.g. Komatsu et al., 2011, Larson et al., 2011]. Observing the rotation profiles of nearby galaxies revealed that the rotational velocity remains constant on the outskirts rather than declining as expected from Keplerian dynamics. This was at first discovered by Rubin and Ford [1970] in M31, raising a very fundamental question: is there an invisible matter component that interacts only gravitationally? Which kind of constituents is this dark matter made of? There have been several attempts to answer these questions during the last decades. Doroshkevich et al. [1981] proposed dark matter would consist of light neutrinos, but this idea was again ruled out a few years later by White et al. [1983] who predicted galaxy clustering in the Universe. This led to the so-called *cold dark matter* (CDM) scenario, where the kinetic energy of the dark matter particles was much smaller than their rest energy at the time when matter decoupled from radiation. The hypothesis that dark matter is mainly composed of Massive Compact Halo Objects (MACHOs), which have a mass of $\sim M_{\odot}$, was disproved by microlensing observations [Alcock et al., 2000, Riffeser et al., 2008]. In today's scenario, dark matter is thought to be (mostly) smoothly distributed.
However, dark matter is not the dominant contribution to the total amount of energy in the Universe. Einstein introduced a cosmological constant Λ in

his field equations [Einstein, 1916], which acts as a repulsing force that counteracts gravity and keeps the Universe static[1]. Hubble [1929] discovered that galaxies at larger distances recess with higher velocity, proving the expansive nature of the Universe. Hubble's discovery led Einstein to revoke his cosmological constant, as by that time the Universe was assumed to be static. Later on, Riess et al. [1998] and Perlmutter et al. [1998] found that the expansion of the Universe is accelerating. To explain this acceleration, one had to introduce either an alternative theory of gravity or add an additional energy component to the Universe. Einstein's cosmological constant was revived, but at that time it was not clear (and still isn't) whether it is really constant or depends on time. The true nature of this so-called "dark energy" is still the subject of ongoing research. Recent studies (e.g. Planck Collaboration et al. [2014]) revealed that dark energy is the dominant component in the Universe, contributing 68.3% to the total energy of the Universe, while dark matter contributes to 26.8%. When talking about a universe containing dark energy and cold dark matter, as it is mostly accepted nowadays, we call it a ΛCDM universe.

1.3 Observational cosmology with galaxy clusters

On the high mass end of structures in the Universe we find clusters of galaxies with masses around $\sim 10^{14}$ to $10^{16} M_{\odot}$. The contribution from galaxies to their total mass is quite small (2-5%), larger contributions come from the hot intra-cluster gas (10-15%) and from the dark matter halo (80-90%). Galaxy clusters emerge from density peaks in the large-scale matter distribution. These arise from a gravitationally amplified noise field of early quantum fluctuations. Therefore, the number density of clusters as well as their spatial distribution can be used to derive parameters of a standard cosmological model.
There is a large diversity of different methods for observing clusters of galaxies. The most important of these are:

1. The Sunyaev-Zel'dovich effect [Sunyaev and Zeldovich, 1972] describes

[1]The Universe does not necessarily collapse in absence of a cosmological constant. The fate of the Universe is decided by the density parameter Ω, which will be introduced in chapter 2.1.1

the distortion of the spectrum of the CMB, imprinted by Inverse Compton scattering at the electrons of the hot intra-cluster medium (ICM). The spectrum is distorted in a way that the flux decreases at frequencies below a characteristic frequency (217 GHz) and increases above that value.

2. Using photometric observations in optical wavebands, clusters can be identified by searching for overdensities of red elliptical galaxies.

3. The X-ray Bremsstrahlung emission from the hot ICM can be observed.

4. The space-time curvature caused by massive objects can bend or deflect light rays on their way to an observer, causing distorted or even multiple images of objects in the background of a galaxy cluster. This effect, called gravitational lensing, can not only trace the baryonic but also the dark matter component of a massive object.

In this work I will focus on the methods 1 and 2, both from an observer's and from an instrument builder's point of view. The Ludwig-Maximilians-Universität München operates an astronomical observatory on the summit of Mt. Wendelstein in the Bavarian Alps. In August 2011, the integration of the new 2m Fraunhofer robotic telescope in a new 8.5m dome has started. This also includes the development of a variety of new, competitive scientific instruments. The Wendelstein Wide Field Imager (WWFI) is a photometric imager with a 64 Megapixel CCD featuring a field of view of 0.7° in diameter, dedicated mainly to the observation of galaxy clusters and groups. The large field of view is needed for example for weak gravitational lensing analyses, as this technique requires the measurement of colors and shapes for a large number of background galaxies. The WWFI started operating in summer 2013 and is observing clusters of galaxies in the northern hemisphere since then. The process of calibrating the WWFI in the laboratory and with first on-sky observations is one of the two main topics of this thesis.
The second part of this thesis is dedicated to galaxy clusters detected by their Sunyaev-Zel'dovich effect. As the beam size of a typical radio telescope is quite large, of the order of a few arcmin, SZ-surveys are potentially prone to selection effects caused by objects along the line of sight in the foreground or background, as the signals from these objects are not easily discriminated from the signal from the cluster of interest. The aim of this project is to test for environmental selection effects of SZ-selected clusters and characterize their impact on mass measurements by various methods.

1.4 Outline of this Thesis

This work is split into two main parts: after a description of the underlying cosmological model and an introduction to the Wendelstein Telescope in chapter 2, I describe the design, calibration and commissioning of the Wendelstein Wide Field Imager in chapter 3. I give an overview of the mechanical and electronic design of the instrument and also describe the software and electromagnetic interference protection. Furthermore I detail the calibration of the detector in our laboratory as well as the first observations, data reduction and commissioning, including zero point and throughput estimations. Finally I compare our camera to the ESO-WFI and OmegaCAM, two similar wide field imagers. The methods and results from this chapter have also been published in Kosyra et al. [2014].
In chapter 4 I present the analysis of environmental selection effects of SZ selected clusters of galaxies, conducted by computing the two point correlation function of clusters detected by the *Planck* satellite [Planck Collaboration et al., 2013a] and optically selected galaxy groups detected by the *RedMaPPer* algorithm [Rykoff et al., 2014] in the SDSS DR8 footprint. The analysis and results presented in this chapter have been published in Kosyra et al. [2015].
In chapter 5 I conclude and give an overview of ongoing WWFI observations as well as future perspectives on upcoming science projects with the WWFI.

Chapter 2

Introduction

2.1 Theoretical background

2.1.1 Cosmology

There is consensus among scientists (Jones and Lambourne [2004], Singh [2005], Silk [2009] among others) that our Universe originated from a hot dense state, cooling down as it continuously expands. Since the *Big Bang*, the starting point of the cosmic expansion 13.7 Billion years ago, the Universe cooled down from a temperature of initially $\sim 10^{30}$ Kelvin to 2.73 Kelvin as it is observed nowadays. During the era of *inflation*, the Universe expanded exponentially by a factor of $\sim 10^{26}$ in a time period of less than 10^{-30}s, while stretching all scales to cosmic dimensions. Roughly 380,000 years after the *Big Bang* (at redshift $z \sim 1100$) the Universe had cooled down to a few thousand Kelvin, allowing first hydrogen and helium atoms to be formed. This time span is referred to as the era of *recombination*. At this point, the opaque Universe became transparent to electromagnetic radiation due to the lack of free electrons causing Thomson scattering. Shortly thereafter, photons decoupled from matter, forming the cosmic microwave background that can still be observed today.
First stars (*Population III* stars) formed from the primordial hydrogen and helium [Abel et al., 1998, Baraffe et al., 2001, Marigo et al., 2001]. The ultraviolet radiation from those very hot and massive stars [Schaerer, 2002] combined with the high energetic radiation from first quasars led to the *reionization* of the Universe [Gnedin and Ostriker, 1997, Tumlinson et al., 2002], which occurred when the Universe was between 400 million and 1

billion years old (in the redshift range $z \sim 15...6$, Zaroubi [2013]). At this point, the matter density was low enough for the Universe to not become opaque again[1]. Since then, larger structures such as galaxies, galaxy groups and galaxy clusters have been forming.

The Homogeneous Universe

Cosmological observations on scales of several hundred Mpc [Jones and Lambourne, 2004] support the *cosmological principle*, which states that the Universe is homogeneous and isotropic on large enough scales. The dynamics of the Universe is described by the theory of General Relativity, which relates the curvature of spacetime and its metric tensor directly to the energy and momentum of matter and radiation. Consequently, spacetime and matter/energy content are not independent from each other, but connected by Einstein's field equations (see Einstein [1916]):

$$G_{\mu\nu} = \frac{8\pi G T_{\mu\nu}}{c^4} - \Lambda g_{\mu\nu}, \tag{2.1}$$

where G is the gravitational constant, c is the speed of light, $g_{\mu\nu}$ is the metric tensor, $G_{\mu\nu}$ is the Einstein Tensor (representing the curvature of spacetime) and $T_{\mu\nu}$ is the energy-momentum tensor. Einstein introduced the cosmological constant Λ, which acts as a repulsive force and counteracts gravity, in order to satisfy the view of a static universe at that time. Robertson [1935] and Walker [1937] independently introduced a metric describing the spacetime in a homogeneous and isotropic expanding universe. The Robertson-Walker metric solves Einstein's field equations and is given by:

$$ds^2 = c^2 dt^2 - a^2(t) \left[d\chi^2 + f_{\mathrm{K}}^2(\chi)(d\theta^2 + \sin^2\theta d\phi^2) \right] \tag{2.2}$$

with four space time coordinates: the timelike coordinate t and the three spacelike coordinates χ, θ, ϕ, which are given here in spherical coordinates. The *scale factor* $a(t)$ considers the expansion of the Universe. The factor $f_{\mathrm{K}}(\chi)$ is a function of the curvature of the Universe K (shown e.g. in Raine and Thomas [2001]):

[1]The Universe became sparser, not only due to the expansion but also owing to the formation of the first stars, which "took away" a large amount of matter from the intergalactic medium. Thus the transparency before reionization was due to neutrality, while the transparency after reionization comes from sparsity.

$$f_{\mathrm{K}}(\chi) = |K|^{-1/2} \sinh\left(|K|^{1/2}\,\chi\right) \equiv \begin{cases} K^{-1/2}\sin\left(K^{1/2}\chi\right) & K > 0 \\ \chi & K = 0 \\ -K^{-1/2}\sinh\left[(-K)^{1/2}\,\chi\right] & K < 0 \end{cases} \tag{2.3}$$

with $\frac{1}{\sqrt{K}}$ being the curvature of space. For vanishing curvature $K = 0$ the geometry is Euclidean (flat), for positive curvature $K > 0$ the geometry is spherical (closed) and for negative curvature $K < 0$ the geometry is hyperbolic (open). The curvature K depends on the total density of the Universe. The quantities $g_{\mu\nu}$ and ds in equations 2.1 and 2.2 are connected by $ds^2 = g_{\mu\nu}\mathrm{d}x^\mu \mathrm{d}x^\nu$ where $\mathrm{d}x^\mu$ and $\mathrm{d}x^\nu$ are the space and time coordinates. Inserting the Robertson-Walker metric (eq. 2.2) into Einstein's field equations (eq. 2.1) and using the energy-momentum tensor $T_{\mu\nu}$ of a perfect fluid, we can derive the Friedmann equations (Friedmann [1922]):

$$H^2(t) := \left(\frac{\dot{a}}{a}\right)^2 = \frac{8\pi G}{3}\rho - \frac{Kc^2}{a^2} + \frac{\Lambda}{3} \tag{2.4}$$

$$\left(\frac{\ddot{a}}{a}\right) = -\frac{4\pi G}{3}\left(\rho + \frac{3p}{c^2}\right) + \frac{\Lambda}{3} \tag{2.5}$$

which describe the evolution of the scale factor $a(t)$ with time for given density ρ and pressure p of all matter, radiation and the cosmological constant Λ. A derivation of equations 2.4 and 2.5 is given for example in Raine and Thomas [2001].
The current value of the Hubble parameter $H(t)$ is expressed by

$$H_0 := H(t_0) = 71.0 \pm 2.5 \frac{\mathrm{km}}{\mathrm{sMpc}} \tag{2.6}$$

and is commonly called Hubble constant (for definition see Hubble [1929], the value is taken from Komatsu et al. [2011]).

Let's assume a flat universe (K=0) without a cosmological constant ($\Lambda = 0$). Then we can define a critical density using equation 2.4:

$$\rho_c = \frac{3}{8\pi G} H(t)^2 \tag{2.7}$$

which determines the geometry of the Universe. $\rho < \rho_c$ indicates an open (hyperbolic) universe, which expands infinitely, even in absence of dark energy. When $\rho = \rho_c$, the Universe is flat (Euclidean). A flat universe without dark energy will expand forever while the expansion rate asymptotically approaches zero. A closed (spherical) universe, indicated by $\rho > \rho_c$, expands until the scale factor reaches a maximum value and contracts again until it collapses into a so-called big crunch [Jones and Lambourne, 2004]. Consequently it has a finite lifetime.
We can state all densities in the Universe in units of the critical density,

$$\Omega = \frac{\rho}{\rho_c}. \tag{2.8}$$

Ω is the so-called density parameter. It can be calculated for three components of the Universe: matter Ω_m, radiation Ω_r and cosmological constant Ω_Λ. From equation 2.4 we get:

$$\Omega_m = \frac{8\pi G}{3H^2}\rho_m,\ \Omega_r = \frac{8\pi G}{3H^2}\rho_r,\ \Omega_\Lambda = \frac{\Lambda c^2}{3H^2} \tag{2.9}$$

and:

$$\Omega_K = 1 - \Omega_r - \Omega_m - \Omega_\Lambda. \tag{2.10}$$

Inserting the time derivative of equation 2.4 into equation 2.5, we obtain the conservation law in the expanding Universe:

$$\frac{d\rho}{dt} + \frac{\dot{a}}{a}\left(3\rho + \frac{3p}{c}\right) = 0, \tag{2.11}$$

which can be rearranged to find a relation between the density and the scale factor:

$$a^{-3}\frac{d\left(\rho a^3\right)}{dt} = -3\frac{\dot{a}}{a}\frac{p}{c^2}. \tag{2.12}$$

For pressureless matter the right hand side of equation 2.12 vanishes, so $\rho_m \propto a^{-3}$. Since radiation has a pressure of $p = \frac{\rho_r c}{3}$, $\rho_r \propto a^{-4}$. This behavior corresponds to the fact that radiation is redshifted as space expands, since the photon density decreases $\propto a^{-3}$ and the photon energy decreases $\propto a^{-1}$. With these definitions we can rewrite equation 2.10 (e.g. Peacock [1999]):

$$H(t)^2 = H_0^2\left(\frac{\Omega_r}{a^4} + \frac{\Omega_m}{a^3} + \frac{\Omega_K}{a^2} + \Omega_\Lambda\right) \tag{2.13}$$

It can be seen that radiation was dominant in the early Universe until matter took over and in recent times the Hubble parameter became governed by the cosmological constant, and thus became constant as well.
Recent observations of type Ia supernovae (Riess et al. [1998], Perlmutter et al. [1998]) found evidence that we live in a low-mass-density universe with a cosmological constant ($\Omega_m \approx 0.3$, $\Omega_\Lambda \approx 0.7$), but the true nature of the accelerated expansion of the Universe is still not revealed.

Cosmological distances

In an expanding universe with a finite speed of light the term *distance* needs special attention as the space itself expands as the light travels from one point to another, which causes the physical distance between two objects to be larger in an expanding universe than in a static one. We define the comoving distance as the distance that remains constant while the Universe expands during the finite light travel time (Dodelson [2003]):

$$\chi(z_1, z_2) = D_H \int_{z_1}^{z_2} \frac{dz'}{E(z')} \tag{2.14}$$

with

$$E(z) = \sqrt{\Omega_r(1+z)^4 + \Omega_m(1+z)^3 + \Omega_K(1+z)^2 + \Omega_\Lambda} \tag{2.15}$$

and the Hubble distance:

$$D_H = \frac{c}{H_0}. \tag{2.16}$$

Another important concept of distance in astronomy is the *angular diameter distance*, which is given by the ratio of an object's physical size l and the angle Θ under which it is observable in the sky:

$$D_a(z) = \frac{l}{\Theta} = \frac{\chi}{1+z} \tag{2.17}$$

The right equality in equation 2.17 is only valid when the size of the object is small compared to its distance from the observer, i.e. the distance can be given in one single redshift. In an expanding universe, the angular diameter distance does not increase monotonically with redshift as one would assume naively, but reaches a maximum at a certain redshift that depends on cosmology (in our Universe at $z \sim 1.5$) and decreases again with increasing redshift.

Consequently, the angular size Θ increases with redshift for $z \gtrsim 1.5$, which is the reason why distant galaxies are still resolved with modern instruments. Figure 2.1 shows the angular size in dependence of redshift for a flat universe with a cosmological constant for different values of Ω_m and Ω_Λ, where $\Omega_m + \Omega_\Lambda = 1$.

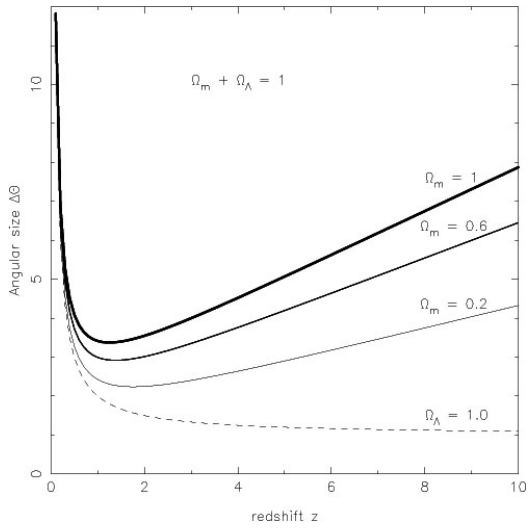

Figure 2.1: The relative angular size $\Delta\theta$ of an object as a function of redshift for a flat universe with a cosmological constant $\Omega_m + \Omega_\Lambda = 1$. Heavier lines correspond to larger values of Ω_m. Courtesy of the figure: `http://ned.ipac.caltech.edu/level5/March02/Sahni/Sahni4_5.html`

Another quantity that is commonly used in cosmology is the *luminosity distance* D_L, defined as radius of sphere in Euclidean space where the flux f emitted by an object with luminosity L would be the same as in an expanding universe,

$$f = \frac{L}{4\pi D_L} \Rightarrow D_L = \sqrt{\frac{L}{4\pi f}}. \tag{2.18}$$

Cosmological redshifts

The expansion of the Universe causes the wavelengths of photons to be increased (redshifted) as the distances are growing while the photons travel through the Universe. This effect, called *cosmological redshift*, is not to be

confused with the redshift due to the Doppler Effect, since the objects are not moving apart from each other due to their proper motion, but space itself is expanding. The cosmological redshift is defined as:

$$1 + z = \frac{\lambda_{\text{obs}}}{\lambda_{\text{em}}}, \tag{2.19}$$

where λ_{obs} is the wavelength of the photon as it is observed and λ_{em} is the wavelength of the photon emitted by an object at a cosmological distance. Consider the photon is emitted at scale factor $a(t)$ and observed today at scale factor $a(t_0) = 1$ then $\lambda_{\text{obs}} = \frac{\lambda_{\text{em}}}{a(t)}$, and the redshift can be written as:

$$1 + z = \frac{1}{a(t)}. \tag{2.20}$$

The redshift of an object can be measured by the displacement of known spectral features (i.e. absorption/emission lines).
When the Hubble constant and the contributions to the density parameter $(\Omega_m, \Omega_r, \Omega_\Lambda)$ are known, cosmological redshifts can be used to estimate the distance of extragalactic objects using equation 2.14. The most accurate method for obtaining redshifts is measuring the spectral energy distributions (SEDs) of extragalactic objects, and identifying features in it, such as known absorption or emission lines. The downside of this method is the very time-consuming process of observing and analyzing spectra. A less expensive method is to estimate the redshift of an object by photometric observations in several filters and consider these data as low resolution spectra. A common method for estimating photometric redshifts is the so-called template fitting method, whose basic idea is that all galaxies can be described by one of a number of galaxy SEDs in their rest frame. A set of model templates or empirical templates extracted from spectroscopic observations is used for the fitting process. Convolving each model SED with the total efficiency of the observing instrument (in each filter) yields the expected magnitude of the SED in the given filter. As the expected magnitudes also depend on redshift, this calculation is done on a discrete redshift grid. The expected fluxes and colors are then compared to the observed fluxes and colors in each filter and the redshift of the object as well as the best fitting models are determined by maximum likelihood calculation. An example of a code for photo-z calculation with the template fitting method is presented in Bender et al. [2001].

2.1.2 Structure formation

The Universe is homogeneous and isotropic on scales greater than $\sim$ 100 Mpc. On smaller scales, at the nodes of the cosmic web, one finds structures like galaxy clusters and groups and, at scales $\lesssim$ 1 kpc, globular clusters, stars and planets. One can now ask the question: what is the origin of these inhomogeneous structures forming out of the initially homogeneous Universe? According to our current understanding, the large scale structure (hereafter LSS) formed because of density fluctuations. But what is the origin of these inhomogeneities? The *inflation* theory (e.g. Guth [1981], Sato [1981]) is able to explain the homogeneity of the Universe on large scales, despite the lack of causal contact of distant regions[2], and provides a possible mechanism as the origin of the inhomogeneities that are the seeds of the structures we observe today. Before the era of inflation, all regions in the Universe were in causal contact with each other. During inflation, an exponential expansion took place and as a result the Universe enlarged to cosmic dimensions. The volume of the Universe grew by roughly $\sim$26 orders of magnitudes in less than 10^{-30}s, disrupting the causal contact between distant regions during that process. The homogeneity was conserved on large scales, but small quantum fluctuations were also enlarged to macroscopic scales. During the subsequent expansion of the Universe, the amplitude of these perturbations increased by gravitational instability. At the time when matter became dominant in the Universe, gravitational attraction between regions of high density led to the formation of virialized systems which merged into larger haloes[3], forming the LSS as observed today.

Additionally to giving an answer to the *horizon problem*, the theory of inflation also provides explanations to the *flatness problem* and the *monopole problem*. The *flatness problem* states that the total density of the Universe has to be fine-tuned to the critical value in order to result in a flat Universe, as it is observed. It is solved by the exponential growth of the scale factor a, while the energy density of the inflation field is constant [Guth, 1981]. The grand unified theories predict the generation of heavy magnetic monopoles at extremely high temperatures. Inflation theory solves this problem as the Universe cools down many orders of magnitude during the exponential ex-

[2]The lack of causal contact between distant regions despite the homogeneous CMB temperature is referred to as the *horizon problem*.

[3]Halo denotes the component that envelopes a galaxy or cluster consisting of dark matter. The halo mass typically exceeds the object's baryonic mass.

pansion [Guth, 1981].
In the following, I will show how small perturbations of an initially homogeneous density distribution evolve into the large structures that we find in the Universe today. According to the cosmological principle, the Universe can be described as a perfect fluid with density ρ and velocity field v. Therefore the continuity equation can be used for the description of the Universe [Raine and Thomas, 2001]:

$$\frac{\partial \rho}{\partial t} = \nabla \left(\rho \vec{v} \right). \tag{2.21}$$

This equation states the conservation of mass, meaning that the change in mass in a fluid contained in a volume element is equal to the mass streaming into minus the mass streaming out of the volume element.
The Euler equation connects the acceleration of a fluid with the pressure gradient and the potential:

$$\frac{\partial \vec{v}}{\partial t} + \left(\vec{v} \cdot \nabla \right) \vec{v} = -\frac{\nabla p}{\rho} - \nabla \Phi. \tag{2.22}$$

The left hand side of the Euler equation reads as the acceleration of a small fluid element (per unit volume). This is caused by the pressure gradient and the gravitational potential (right hand side), the latter is described by the Poisson equation:

$$\nabla^2 \Phi = 4\pi G \rho, \tag{2.23}$$

which states that density perturbations are caused by potential fluctuations. Let's consider a matter-dominated universe, as the Universe is today, and for simplicity, small perturbations $\delta\rho$, δv and $\delta\Phi$ from the initial values ρ_0, v_0 and Φ_0, which allow for a linearization of the underlying equations. After subtracting the unperturbed equations from the perturbed ones and some calculations (with an ansatz for the spatial distribution $\delta \propto e^{-i\vec{k}\vec{r}}$ and a proper wave vector $\vec{k}$; see Peacock [1999]), we obtain a differential equation for the evolution of density fluctuations:

$$\ddot{\delta} = \delta \left(4\pi G \rho_0 - c_s^2 k^2 \right), \tag{2.24}$$

where $c_s^2 = \frac{\partial p}{\partial \rho}$ is the sound speed and k is the wavenumber. The solutions of equation 2.24 refer to amplitudes that decay, oscillate or grow over time, depending on the right hand side (rhs). With these quantities at hand,

we define the Jeans length as the minimum wavelength of modes for which the amplitude is increasing exponentially with time (i.e. rhs of eq. 2.24 is positive):

$$\lambda > \frac{2\pi}{k} = c_s \sqrt{\frac{\pi}{G\rho_0}}. \tag{2.25}$$

In other words, the Jeans length can be understood as the scale length over which the pressure can compensate gravitational instabilities. In the early, radiation-dominated Universe before recombination[4], the sound speed is given by $c_s = \frac{c}{\sqrt{3}}$, and consequently the Jeans length changes by a factor of $\sqrt{\frac{3}{8}}$. This lower Jeans length and Silk damping (Silk [1968]), which describes the effect of photon diffusion erasing perturbations in the radiation-dominated Universe, have suppressed the growth of structures with masses below $\sim 10^{16} M_\odot$ (Jones and Lambourne [2004]) in the early Universe[5].
During the epoch of recombination, when the first neutral atoms formed, the radiation pressure due to the interaction of photons with free electrons dropped rapidly; thus the thermal gas pressure was the only force counteracting the gravitational collapse. This led to a decrease of the minimum mass at which overdense regions become unstable (Jeans mass) from $\sim 10^{16} M_\odot$ before recombination to $\sim 10^5 M_\odot$ after recombination [Jones and Lambourne, 2004].
In the matter-dominated Universe, the sound speed becomes a function of temperature:

$$c_s^2 = \frac{\partial p}{\partial \rho} = \frac{5kT}{3m}, \tag{2.26}$$

where m is the particle mass. Consequently the Jeans length decreases as the Universe expands, allowing the formation of smaller structures with time.
The hierarchical order of structure formation depends on the nature of the dark matter. In a hot dark matter scenario[6], larger masses are necessary to

[4]Strictly speaking, the era of recombination and matter-radiation equality are two different epoch, but since photons and baryons were coupled before recombination, this reasoning is still valid.

[5] Theoretically, structures with masses $\gtrsim 10^{16} M_\odot$ could have formed in the radiation dominated Universe, but on the other hand at these early times, the horizon distance was so small that the masses contained within the horizon never exceeded the limit of the Jeans mass [see Jones and Lambourne, 2004].

[6]In hot dark matter scenario, the kinetic energy of the dark matter was of the same

bind the relativistic particles. Consequently, the first structures to be formed are the most massive clusters with masses $\gtrsim 10^{15} M_\odot$ which then fragment into smaller structures like galaxies (top-down structure formation). In a cold dark matter scenario[6] on the other hand, the Jeans length and corresponding mass are much smaller, supporting the formation of sub-galactic structures like globular clusters initially, which then merge into galaxies (bottom-up structure formation).

Correlation function and power spectrum

The probability of finding galaxies, galaxy groups or clusters is not uniformly distributed, as the formation of structure is more probable in regions where the density is higher due to fluctuations. In these over-dense regions, the gravitational potential of matter slows down the expansion, increasing the density even further, while in under-dense regions the expansion is accelerated due to the lack of self-gravitation, and density is further decreased, creating voids. In order to characterize these fluctuations with statistical measures of the observed matter distribution, it is convenient to introduce the density contrast:

$$\delta(\vec{x}) = \frac{\rho(\vec{x}) - \langle\rho\rangle}{\langle\rho\rangle}, \tag{2.27}$$

with $\langle\rho\rangle$ being the mean density of the Universe. The density contrast is $-1 \leq \delta(\vec{x}) < 0$ in under-dense regions and $\delta(\vec{x}) > 0$ in over-dense regions.
One possible way of describing this clustering is the isotropic two point correlation function and its Fourier Transform, the power spectrum. The two point correlation function traces the amplitude of clustering as a function of separation. The probability to find an object at position $\vec{x}$ in a volume element dV is given by P. The probability to find another object at position $\vec{x}+\vec{r}$ in a volume element dV simultaneously would be P^2, if the probabilities were independent. The two point correlation function of density contrast corrects for the excess probability due to density fluctuations, introducing the enhanced probability $P_1^2 = P^2\,(1 + \xi(\vec{r}))$. The correlation function is thus described by the following equation (Peacock [1999], p. 497):

order of magnitude or higher than their rest energy at the time when matter decoupled from radiation. Likewise, in a cold dark matter scenario, the kinetic energy was much smaller.

$$\xi(\vec{r}) \equiv \langle \delta(\vec{x})\delta(\vec{x}+\vec{r}) \rangle \,. \tag{2.28}$$

The Fourier transform of the two point correlation function is the power spectrum of density fluctuations:

$$\xi(\vec{r}) = \frac{V}{(2\pi)^3} \int |\delta_k|^2 \, e^{-ik\vec{r}} d^3k, \tag{2.29}$$

where δ_k is the Fourier transform of δ. In an isotropic universe, the density perturbation spectrum does not have a preferred direction, so the power spectrum has to be isotropic. We can rewrite equation 2.29 as:

$$\xi(r) = \frac{V}{(2\pi)^3} \int P(k) \frac{\sin(kr)}{kr} 4\pi k^2 \, dk, \tag{2.30}$$

where

$$P(k) \equiv \left\langle |\delta_k|^2 \right\rangle \tag{2.31}$$

is the power spectrum. Since in the primordial Universe[7] there was no characteristic length scale, the primordial power spectrum takes the form of a power law:

$$P(k, z=0) = T^2(k) A \, k^n, \tag{2.32}$$

with amplitude A and scalar spectral index n. CMB measurements of Komatsu et al. [2009] have determined a value of $n = 0.96$. The transfer function $T(k)$, modeled by Eisenstein and Hu [1998], includes baryonic effects for predicting the evolution of density perturbations.
The power spectrum in today's Universe arises from the primordial power spectrum being influenced by a variety of physical processes: modes of short wavelengths are decaying while modes of long wavelengths are growing.
The time development of inhomogeneities can be described in linear approximation as:

$$P_{lin}(k, z) = D^2(z) P(k, 0), \tag{2.33}$$

where $D(z)$ is the linear growth factor (Hamilton [2001]). Note that both $T(k)$ and $D(z)$ depend on the dark matter model.
On scales below ~ 5 Mpc the linear approximation fails to predict the growth of structures, as collapsing structures begin to play a role here.

[7] The time period from the Big Bang until the recombination of electrons and nuclei is called primordial universe.

The mass function and the Press-Schechter Model

As stated in section 2.1.2, when the amplitude of perturbations is small, we are in a linear regime. Press and Schechter [1974] introduced a method for estimating the density of dark matter haloes using a spherical collapse model. We assume a random density fluctuation field $\delta(\vec{x})$ with fluctuations on all scales as described by the power spectrum $P_0(k)$ (eq. 2.31) and corresponding correlation function (eq. 2.28).
We consider a power spectrum described by a single, featureless power law:

$$P(k) \propto k^n. \tag{2.34}$$

We obtain the variance of the density field by introducing a filter function $f_R(\vec{x})$ with a characteristic length scale R, which is typically a Gaussian or top hat:

$$\sigma^2(R) = \int\int \xi(|\vec{x} - \vec{x}'|) f_R(\vec{x}) f_R(\vec{x}') d^3x d^3x', \tag{2.35}$$

where $\xi(|\vec{x} - \vec{x}'|)$ is the correlation function. In linear theory, gravitational collapse sets in as soon as the density exceeds the critical density, which has a value of $\delta_c = 1.68$ today and evolves with redshift as:

$$\delta_c(z) = (1 + z)\delta_c. \tag{2.36}$$

The filter function can also be used to smooth the density fluctuation field:

$$\delta_R(\vec{x}) = \int \delta(\vec{x}') f_R(\vec{x} - \vec{x}') d^3x'. \tag{2.37}$$

We also define the mass contained within the characteristic radius R of the filter function f_R as:

$$M = \frac{4}{3}\pi\rho_0 R^3, \tag{2.38}$$

where ρ_0 is the uniform background density. Now we need to calculate the abundance of regions with densities greater than the critical density δ_c, for an initially Gaussian density field. The formula is derived e.g. in Peacock [1999]:

$$f(M, z) = \sqrt{\frac{2}{\pi}} \left| \frac{d\sigma}{dM} \right| \frac{\rho_0}{M} \frac{\delta_c(z)}{\sigma(M)^2} \exp\left(-\frac{\delta_c(z)^2}{2\sigma(M)^2} \right). \tag{2.39}$$

It is evident that the number density of haloes decreases exponentially with M, as larger masses correspond to larger smoothing lengths and the number

of maxima with fixed amplitude δ_{min} decreases with increasing smoothing length. As the variance $\sigma(M)$ is a decreasing function of the mass, low mass structures are more frequent than high mass structures. There are less structures formed at higher redshift, as $\delta_c(z)$ increases with redshift, resulting in a bottom-up mass assembly.

Halo bias

Fluctuations in the number density of galaxy clusters are more evident than in galaxies' number density, which analogously cluster more strongly than the underlying matter distribution. The halo bias parameter b (see Bahcall and Soneira [1983]) is defined as the ratio of the density contrast of a certain type of objects (e.g. clusters) and the density contrast of the matter density field:

$$b(M) = \frac{\delta_{\mathrm{cl}}(M)}{\delta}. \tag{2.40}$$

The squared halo bias is then the ratio between the halo power spectrum and the linear matter power spectrum. The halo bias can be estimated by the approach from Mo and White [1996], in which the density perturbations are separated into short- and long-wavelength modes. The bias parameter can be assumed as scale-independent in the linear regime, but it is a strong function of cluster mass, as shown in for example in Mo and White [1996] and Tinker et al. [2010].
The mass function depends exponentially on the cosmological parameters, and consequently, galaxy clusters can be used as probes of cosmological models. Since the analytical work of Press and Schechter [1974] there has been a lot of effort to construct a refined halo mass function. A common approach is to count haloes in elaborated N-body simulations and construct a mass-dependent fitting formula for eq. 2.39 (Sheth and Tormen [1999], Jenkins et al. [2001], Tinker et al. [2008, 2010]).

Galaxy clusters

Clusters of galaxies are the most massive and the youngest known gravitationally bound structures in our Universe. Studying galaxy clusters is particularly interesting to cosmologists, as they trace directly the formation of the LSS. They consist of 50-1000 gravitationally bound galaxies, have typical masses of $\sim 10^{14} - 10^{16} M_{\odot}$, velocity dispersions of $\sim 800 - 1400 \mathrm{km\,s^{-1}}$,

radii of $\sim 1-3$Mpc and X-ray luminosities of $\sim 10^{43}-10^{45}\mathrm{erg\,s^{-1}}$. Clusters are typically found at redshifts $z < 1.0$. We can distinguish between regular clusters with a roughly spherical shape and a rising density profile towards the center, and irregular ones which vary in shape and might have no distinct center or even feature multiple overdense regions that can be identified as centers. Galaxy clusters are composed of:

- Galaxies, which contribute only $2-5\%$ to their mass, mostly early-type ellipticals populating the so-called *red sequence* in color magnitude space, a fact commonly exploited for optical cluster detection. Clusters typically feature a single Brightest Cluster Galaxy (BCG), which is commonly defined as the cluster center. Only $1-2\%$ of all galaxies are located in clusters (Murdin [2001]).

- Intra-cluster medium (ICM), which contributes $\sim 10-15\%$ to the total mass and consists of highly ionized baryonic matter with low density ($\sim 10^{-3}\mathrm{cm^{-3}}$) and high temperature ($\sim 10^{7}-10^{8}\mathrm{K}$). Thermal Bremsstrahlung processes in the hot ICM are responsible for the strong X-ray emission of the clusters in the wavelength region $0.1-100$Å. The ICM causes the interaction with CMB photons via the Inverse Compton Effect, causing a characteristic frequency shift in the CMB spectrum known as the Sunyaev-Zel'dovich effect (Sunyaev and Zeldovich [1972]), which will be discussed in section 2.1.3.

- Dark matter, which contributes $80-90\%$ to the cluster mass. Its distribution is best described by the Navarro-Frenk-White profile (Navarro et al. [1997]), which depends on the central density and scale radius.

Galaxy groups

Groups of galaxies are less rich and therefore less massive than galaxy clusters, but much more abundant. About $50-70\%$ of galaxies in the Universe reside in groups. They usually consist of 2-50 gravitationally bound galaxies, have typical masses of $\sim 10^{12}-10^{14}M_{\odot}$, lower velocity dispersions than clusters $\lesssim 500\mathrm{km\,s^{-1}}$, typical radii of smaller than 1.5 Mpc. More massive groups show X-ray luminosities of $\sim 10^{41}-10^{43}\mathrm{erg\,s^{-1}}$, while less massive groups tend to have no X-ray emission at all. Groups can be found at all redshifts, including $z > 1.0$, which tells us that they have been formed earlier than clusters. This statement is supported by the observational fact that

both early and late-type galaxies reside in groups. Due to the low velocity dispersions, galaxies in groups are much more affected by mergers then cluster galaxies: this fact strongly influences the evolution of group galaxies. Other than clusters, groups show a variety of different dynamical states from fully virialized to collapsing (i.e. our local group). The local group consists of about 40 members, where the Milky Way is the second largest and Andromeda (M31) the largest one.

Detection methods

Since galaxy groups and clusters are very massive and emit radiation nearly throughout the complete electromagnetic spectrum, a variety of different observational methods exists to detect them and measure their masses. We will give a brief overview of the most important detection methods here, including optical, X-ray and gravitational lensing. The description of the Sunyaev Zel'dovich effect is given in the separate section 2.1.3, since this effect is closely connected to the topic of this work.

Optical

One of the most common methods for cluster/group detection is the *matched filter* technique, which was introduced by Postman et al. [1996]. This method quantifies the spatial and luminosity distributions of cluster galaxies at different redshifts, and compares them to the distributions of foreground and background galaxies. The redshifts and richnesses[8] are estimated from the color and magnitude information of the member galaxies.
Another well developed method of optical cluster detection is the so-called *red sequence* method (Gladders and Yee [2005], Koester et al. [2007], Rykoff et al. [2014]), which exploits the fact that most cluster members are located on a narrow sequence in color-magnitude space, the *red sequence*. The aim of this method is to search for spatial overdensities of those galaxies. Figure 2.2 shows a color-magnitude diagram of the member galaxies of two SZ-selected clusters.
A recent implementation of red sequence cluster detection is the RedMaPPer algorithm (Rykoff et al. [2014], Rozo and Rykoff [2014], Rozo et al. [2014]), which we will describe in greater detail in section 4.2.

[8]The number of galaxies identified as members of a cluster is called the cluster's richness.

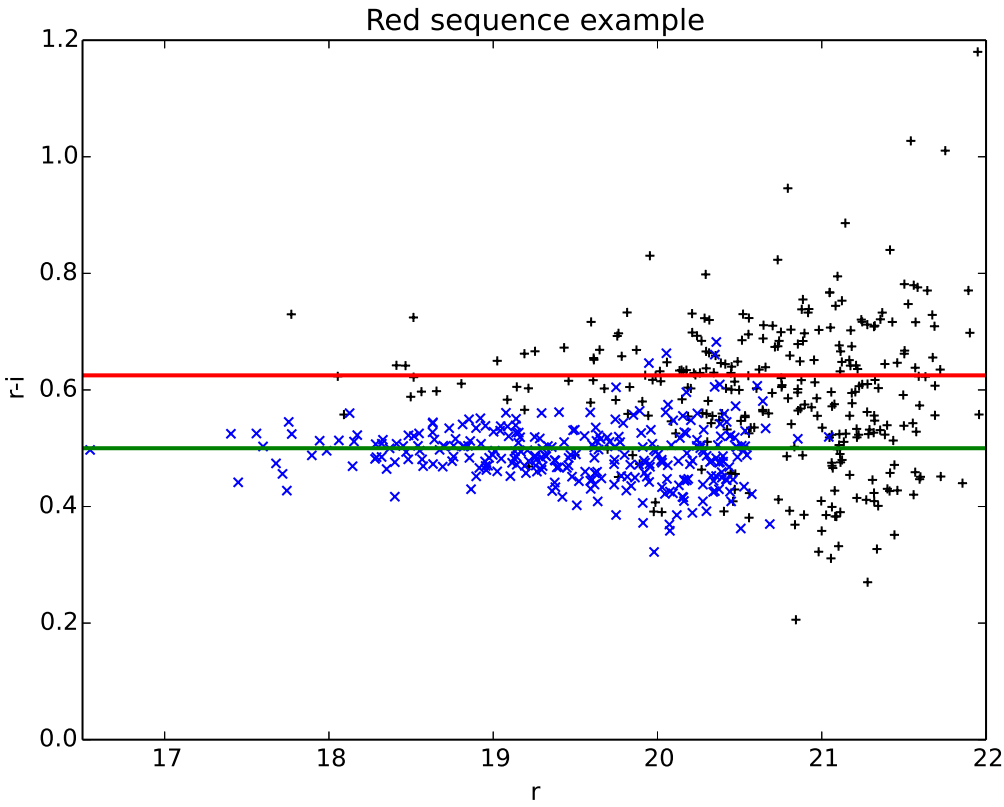

Figure 2.2: Color magnitude diagrams of two clusters of galaxies that have been detected by the *Planck* satellite, with redshifts 0.39 (black) and 0.23 (blue). The cluster members clearly inhabit a narrow sequence in color space, called the *red sequence*, which is commonly used for cluster identification. The red and green horizontal lines denote the expected color-position of the red sequence according to Rykoff et al. [2014], for the clusters at $z = 0.39$ and $z = 0.23$, respectively. The large scatter around this expected color is due to large photometric errors, the intrinsic scatter of the red sequence galaxies is much smaller, see Rykoff et al. [2014].

X-ray

Galaxy clusters and some (rich) galaxy groups are very bright in the X-ray regime of the electromagnetic spectrum due to the thermal Bremsstrahlung

in the hot ICM. X-ray observations suggest that conclusions about the dynamical state of the cluster can be drawn from the morphology of the gas. The X-Ray luminosity of clusters and (rich) groups is of the order of $\sim 10^{41} - 10^{45}\mathrm{erg\,s^{-1}}$. Modern X-Ray missions like XMM-Newton [Jansen et al., 2001, Finoguenov et al., 2007] and Chandra[9] [Weisskopf, 2001] have detection limits of the order of $\sim 10^{-15}\mathrm{erg\,cm^{-2}\,s^{-1}}$, allowing the detection of sources with fluxes $\sim 10^{41}\mathrm{erg\,s^{-1}}$. The hot gas in the ICM is assumed to be isothermal (and thus a Maxwellian velocity distribution), with a thermal velocity of the same order as the velocity dispersion of the galaxies. The following relation for the for the gas temperature holds (Rosati et al. [2002]):

$$k_B T \simeq \mu m_p \sigma_v^2 \simeq 6 \left(\frac{\sigma_v}{10^3 \mathrm{km\,s^{-1}}}\right)^2 \mathrm{keV}, \tag{2.41}$$

where m_p is the proton mass, μ is the mean molecular weight ($\mu = 0.6$ for a primordial composition of 76% hydrogen) and σ_v is the root mean square of the thermal gas velocity (the same as the galaxies' velocity). If we assume spherical symmetry and hydrostatic equilibrium, the gas pressure p can be related to its density ρ_{gas} as:

$$\frac{dp}{dR} = -\frac{GM(<R)\rho_{\mathrm{gas}}(R)}{R^2}. \tag{2.42}$$

By inserting the equation of state for a perfect gas $p = \frac{\rho_{\mathrm{gas}} k_B T}{\mu m_p}$ eq. 2.42 leads to an expression for the total mass M enclosed within the radius R:

$$M(<R) = -\frac{k_B T R}{G\mu m_p}\left(\frac{d\ln\rho_{\mathrm{gas}}}{d\ln R}\frac{d\ln T}{d\ln R}\right). \tag{2.43}$$

In order to determine the cluster mass from X-ray measurements, we approximate the gas density profile by the β-model (Cavaliere and Fusco-Femiano [1976]), which describes an isothermal gas in hydrostatic equilibrium by assuming a King dark-matter profile. The β-model is given by:

$$\rho_{\mathrm{gas}}(r) = \rho_0 \left[1 + \left(\frac{r}{r_c}\right)^2\right]^{-3\beta/2}, \tag{2.44}$$

where β is the ratio between the kinetic dark-matter energy and the thermal gas energy. Since the X-ray luminosity is proportional to the gas density

[9] http://www.chandra.harvard.edu/

squared ($L_X \propto \rho_{gas}^2 r^3$), X-ray observations are best suited for studying the inner regions of galaxy clusters. Kaiser [1986] described the cluster thermodynamics by a purely gravitational approach, finding a relation between cluster mass and X-ray luminosity: $M \propto L_X^{3/4}$. X-ray emission from clusters is associated only with the baryonic matter content, not with dark matter. This may cause a mass bias when comparing cluster masses derived from X-ray observations with masses obtained from other observables.
A possible source of systematic errors in X-ray studies is the assumption of spherical symmetry and (hydrostatic and thermodynamic) equilibrium, can lead to uncertainties when analyzing individual systems, especially for low mass objects.

Gravitational lensing

As mentioned before, galaxy clusters and groups consist of a small fraction of baryonic (luminous) matter, while the largest contribution is dark matter, which does not emit any electromagnetic radiation at all. This calls for a method of observing clusters based on their total masses, instead of their electromagnetic emission. Gravitational lensing exploits the fact that radiation from galaxies in the background of a cluster is deflected by the gravitational potential of the cluster itself. This effect causes the images of background galaxies to be distorted (weak lensing regime), or multiplied (strong lensing effect) in case of a strong gravitational field (i.e. near the cluster core). The estimated masses obtained by gravitational lensing are independent of the dynamical state of the object and of the composition of (baryonic and dark) matter.
The deflection angle $\hat{\alpha}$ is derived from the theory of General Relativity. It reads:

$$\hat{\alpha} = \frac{4GM}{c^2 \xi}, \tag{2.45}$$

where ξ is the closest distance of the light ray to the mass center of the deflector, M is the mass of the deflector, G is the gravitational constant and c is the speed of light. Measuring the deflection angle of a light ray passing the sun yields a value of $\sim 1.75''$, which is in agreement with the prediction from General Relativity. Since the predicted result from Newtonian Theory is smaller by factor 2, this was one of the first results confirming Einstein's Theory of General Relativity.

For the lensing formalism we introduce the notation from Bartelmann and Schneider [2001]. We use the so-called *thin-lens approximation*, which is valid if both the angular diameter distance between observer and deflector D_d and the angular diameter distance between deflector and source D_{ds} are small compared to the physical extent of the lens. This is the case in nearly all cosmological applications. We project the lens mass distribution to the lens plane, orthogonal to the line of sight. The surface mass density in the lens plane reads as:

$$\Sigma(\vec{\xi}) = \int \rho(\vec{\xi}, l) dl, \tag{2.46}$$

where $\rho(\xi, l)$ is the density and $\vec{\xi}$ is a two dimensional vector in the lens plane. The deflection angle is then given by integrating over the deflections of all mass elements in the lens plane:

$$\vec{\hat{\alpha}}(\vec{\xi}) = \frac{4G}{c^2} \int \Sigma(\vec{\xi'}) \frac{\vec{\xi} - \vec{\xi'}}{\left|\vec{\xi} - \vec{\xi'}\right|^2} d^2\vec{\xi'}. \tag{2.47}$$

The geometry of a typical lensed image is displayed in figure 2.3. By introducing the angular diameter distance from the observer to the source D_s (note that $D_s \neq D_d + D_{ds}$ due to the expanding nature of the Universe), we can define a reduced deflection angle:

$$\vec{\alpha} = \frac{D_{ds}}{D_s} \vec{\hat{\alpha}}, \tag{2.48}$$

and a relation between the true source position and the observed image position, the *lens equation*:

$$\vec{\beta} = \vec{\theta} - \vec{\alpha}(\vec{\theta}). \tag{2.49}$$

Since equation 2.49 is generally non-linear, it is possible to obtain multiple solutions for β for a single source, which means that one object can be multiply imaged. In general, multiple images occur when the convergence

$$\kappa(\vec{\theta}) = \frac{\Sigma(\vec{\theta})}{\Sigma_c} \text{ with } \Sigma_c = \frac{c^2}{4\pi G} \frac{D_s}{D_d D_{ds}} \tag{2.50}$$

is greater than 1. To discriminate the regions of strong (multiple images) and weak (single, distorted image) lensing, it is useful to define the Einstein radius, which reads for a point-mass lens of mass M as:

$$\theta_E = \sqrt{\frac{4GM}{c^2} \frac{D_{ds}}{D_s D_d}}. \tag{2.51}$$

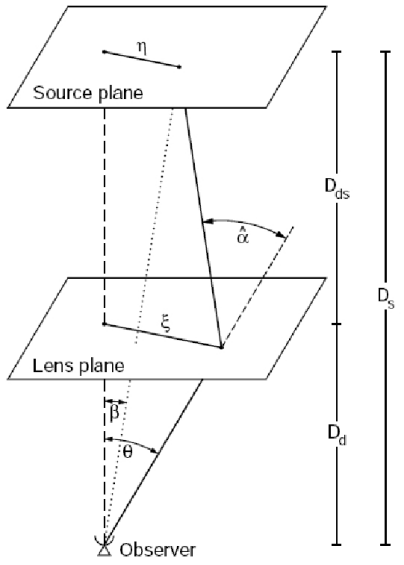

Figure 2.3: The geometry of a lensing system. The angular diameter distances between observer and lens, observer and source and between lens and source are denoted by D_d, D_s and D_{ds} respectively. The transverse distance from the source to the optical axis is η, the distance of the light ray to the lens in the lens plane is given by ξ. β denotes the angle between the observed image and the optical axis, θ is the the angle between the (unlensed) source and the optical axis and $\hat{\alpha}$ is the deflection angle, which is connected to the reduced deflection angle α via equation 2.48. Credit of the figure: Bartelmann and Schneider [2001]

This is the radius of the circular image caused by a source-lens system that is perfectly aligned along the line of sight; this is a very rare configuration, but broken rings can be observed more often, the ring segments in these cases are called arcs. The Einstein radius divides the regions of $\kappa > 1$ (inside), where multiple images are observed and $\kappa < 1$ (outside), where only distortions and (de-) magnifications are observed.

An additional problem that arises when one wants to measure the distortion of background galaxies in a weak lensing analysis, is the fact that galaxies are not circular but intrinsically elliptical, so the observed images are a superposition of their intrinsic ellipticity and the distortion imprinted by the

shear. Since the Universe is assumed to be homogeneous and isotropic, there is no preferred direction of the intrinsic ellipticity of galaxies, thus for a large enough sample, the mean ellipticity is zero. This means it is possible to measure the shear if a large number of background galaxies is available (thanks to deep observations) by averaging over all available sources, even though the intrinsic ellipticity is approximately one order of magnitude larger than the distortion imprinted by the shear. Weak lensing is thus very well suited to study less dens regions, like for example the outer regions of galaxy clusters and groups.

2.1.3 The Sunyaev Zel'dovich effect

The intra-cluster medium, consisting of highly ionized hot gas, contributes a substantial amount to the total mass of a galaxy cluster. Rashid Sunyaev and Yakov Zel'dovich predicted that photons from the CMB traveling through the ICM may be boosted to higher energies by inverse Compton scattering with the electrons in the hot gas. This results in a characteristic distortion of the CMB spectrum crossing a galaxy cluster. The spectrum of the SZ-effect can be approximated by the sum of two components, the (i) thermal SZ-effect that is caused by the random thermal motion of the scattering electrons (Sunyaev and Zeldovich [1972]), and the (ii) kinematic SZ-effect due to the peculiar motion of the ICM with respect to the CMB rest frame (Sunyaev and Zeldovich [1980]). In the following I will only consider the thermal SZ-effect, as the kinematic effect is assumed to be much smaller (Gramann et al. [1995], Sheth and Diaferio [2001], Suhhonenko and Gramann [2003]).

The thermal SZ-effect has a distinct spectral signature, coming into effect as a decrease of the net flux at frequencies below the crossover frequency $\nu \approx 217$ GHz (or $\lambda \approx 1.4$ mm) and an increase of the flux at higher frequencies. This implies that clusters are shining at frequencies above the threshold, while they are obscuring the CMB at lower frequencies. The exact value of the crossover frequency depends on the temperature of the ICM (Rephaeli [1995]).

Formulation of the thermal SZ effect

The rate of change of the photon occupation number has been quantified by Zeldovich and Sunyaev [1969] as:

$$\frac{\partial n}{\partial t} = \frac{k_B T}{m_e c} \frac{\sigma_T n_e}{x^2} \frac{\partial}{\partial x} \left(x^4 \frac{\partial n}{\partial x} \right), \tag{2.52}$$

where $x = \frac{h\nu}{k_B T}$ is the dimensionless frequency and σ_T is the Thomson cross section.
The dimensionless Compton parameter y is defined as the integral of the electron density multiplied by the temperature along the line of sight:

$$y = \frac{k_B \sigma_T}{m_e c^2} \int T n_e dl, \tag{2.53}$$

where $m_e c^2$ the rest energy of the electrons.
The integral over the physical extent of y yields the SZ observable Y:

$$D_A^2 Y = \frac{k_B \sigma_T}{m_e c^2} \int T n_e dV, \tag{2.54}$$

where D_A is the angular diameter distance.
The temperature decrement in the ICM is then given by [Sunyaev and Zeldovich, 1972]:

$$\frac{\Delta T}{T} = -2y. \tag{2.55}$$

As the SZ effect is a scattering process, the magnitude of the frequency shift is independent of redshift.

SZ cluster detection

While the SZ effect is an unwanted effect for measurements of the CMB temperature, it grants a new method of detecting galaxy clusters. The SZ surveys are particularly well-suited for cluster detection, as every cluster above a certain mass threshold will be detected, independent of redshift. To distinguish the SZ signal caused by a cluster from CMB fluctuations, both the spatial and spectral dependence of fluctuations of the CMB need to be taken into account. In each frequency band, the data are convolved with a spatial high-pass filter to remove the background and isolate the (high-spatial frequency) SZ signal. When extracting an SZ signal from a multitude

of frequency bands, the frequency dependence of the signal and the cross-correlation between the channels are considered to either generate a set of maps (one for each band), then combined for detection, or to form a single combined map.
Similar to X-ray observations, the SZ effect traces the gas density in the ICM. An important difference, however, is that the SZ observable depends linearly on the gas density $Y \propto \rho_{gas}$ (opposed by the quadratic dependence of the X-ray luminosity), which makes the SZ effect a very good tracer for the outskirts of clusters. The total cluster mass can be computed from the SZ brightness by assuming hydrostatic equilibrium. SZ selected clusters tend to be biased towards high mass systems, since only the most massive clusters have a significant SZ signal in current missions.
Staniszewski et al. [2009] conducted an SZ cluster survey with the South Pole Telescope, searching for clusters in single-band mode at 150 GHz, confirming their candidates at 95 and 225 GHz.
The *Planck* survey satellite, whose main task is to perform CMB anisotropy measurements, is also very successful at detecting galaxy clusters via the SZ effect. The *Planck* PSZ1 union catalog contains 1227 clusters over the whole sky, selected for their SZ effect (Planck Collaboration et al. [2013a]). Since the *Planck* PSZ1 union catalog plays a central role in this work, I will give more detailed information about the *Planck* signal extraction in chapter 4.

2.2 Introduction to the Wendelstein 2m Telescope and the WWFI

The Wendelstein Observatory (operated by Ludwig-Maximilians-Universität München), located in the Bavarian alps at 47°43′13.1″ north and 12°00′43.4″ east at an elevation of 1838 m above sea level, has been equipped with a modern 2m-class robotic telescope inside a 8.5 m dome, replacing the older 80 cm telescope. The *Fraunhofer* telescope was built by the German companies Kayser-Threde GmbH[10] and Astelco Systems GmbH in Munich, using a very compact three-mirror design in order to fit the telescope inside the dome[11]. The first two mirrors form a Ritchey-Cretien system with

[10]Now OHB Systems AG

[11]The diameter of the dome is limited to 8.5m due to the limited space on the steep summit of mount Wendelstein.

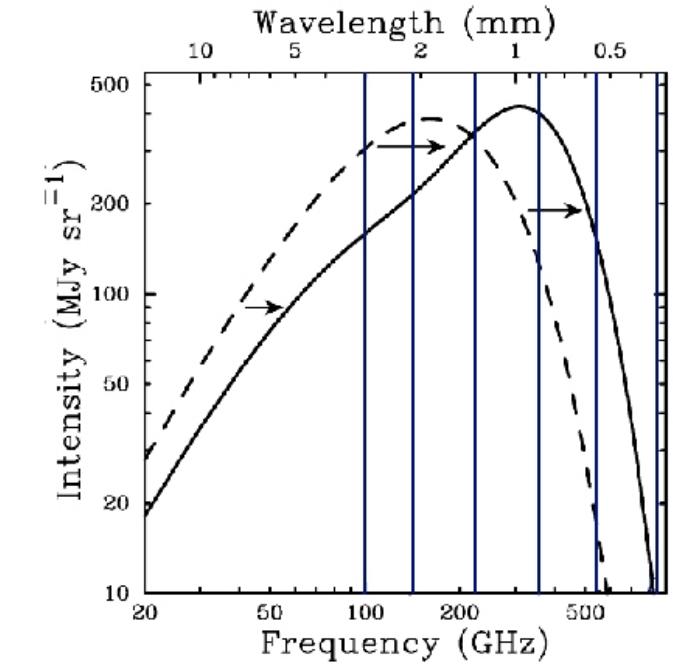

Figure 2.4: Distortion of the CMB by the SZ effect. The dashed line is the undistorted CMB spectrum while the solid line represents the observed spectrum after the radiation of the CMB passes through a galaxy cluster. The amplitude of the frequency shift depends only on the mass of the cluster but not on its redshift. The effect is greatly exaggerated here, for better visualization. The six blue vertical lines denote the frequencies used by the *Planck* satellite to detect clusters (100, 143, 217, 353, 545 and 857 GHz). Courtesy of the figure: http://astro.uchicago.edu

a focal ratio of f/7.8, while the third mirror is flat and reflects the light into the focal stations. One of the two Nasmyth ports of the Alt-Azimuth mounted telescope is equipped with a three lens field corrector (the wide field port will be referred to as "port 2", while the other one will be called "port 1"), designed to maintain the excellent seeing quality (median $<0.8''$) of the site [Hopp et al., 2008] over a field of view (FoV) of 0.22deg^2. The wide field port is equipped with the Wendelstein Wide Field Imager [see Gössl et al., 2010, 2012, Kosyra et al., 2014], a 64 Mpixel mosaic consisting of 2×2 4k $\times$ 4k CCDs with a field of view diameter of $0.7°$, manufactured by Spectral Instruments Inc. The *Fraunhofer* telescope entered its commissioning phase in autumn 2013. The pixel scale of 0.2 arcsec per pixel was chosen, following the *Nyquist theorem* [see Nyquist, 1928], in such a way that sources with a seeing of 0.4 arcsec, which is half the median seeing of the site, are sampled. This results in a pixel size of 15μm. The Wendelstein Wide Field Imager was chosen as the scientific first light instrument for the new *Fraunhofer Telescope* for two reasons. First, it should support the tedious alignment of the very compact optical system of the telescope, and second, it should provide early science verification during telescope commissioning with a number of projects we were already pursuing. These projects were: difference imaging of Local Group galaxies to search for variables and microlensing events [e.g. Lee et al., 2012, Kodric et al., 2013], planet transit analyses [e.g. Koppenhoefer et al., 2013], surface photometry of galaxies [e.g. Kormendy and Bender, 2012] and weak lensing mass estimates for galaxy clusters [e.g. Gruen et al., 2014].
Figure 2.5 shows the peak of mount Wendelstein, featuring the 0.5 MW radio antenna and to the left the Wendelstein observatory with its 8.5 m dome containing the *Fraunhofer Telescope*, and figure 2.6 shows the WWFI mounted at the wide field port of the telescope.

Figure 2.5: Image of the summit of mount Wendelstein, showing the radio antenna and 8.5 m dome of the observatory to the right.

Figure 2.6: WWFI (left) mounted at one Nasmyth port of the *Fraunhofer Telescope*.

Chapter 3

WWFI: A wide field camera for the Wendelstein 2m Telescope

In this chapter I describe the details of the design, calibration and commissioning of the Wendelstein Wide Field Imager (WWFI). In section 2.2 I start with a description of the Wendelstein 2m Fraunhofer Telescope and state the science drivers that led to the development of the WWFI. In section 3.1 I describe the mechanical and optical layout as well as the electrical and software design. All laboratory measurements that have been performed for the calibration of the WWFI are presented in section 3.2. These include measurements of the gains and linearities, the detectors' quantum efficiencies (QE), the readout noises, the charge transfer efficiencies as well as the characteristics of persistent charges. I will also make a proposal for dealing with the problem of charge persistence. In section 3.3 I compare our lab results with first on sky commissioning observations of globular cluster Messier 13 and three standard star fields from the Landolt catalog. I measure the zero points and compare them to theoretical predictions based on efficiency measurements from the laboratory. Furthermore I characterize the on sky performance using the stellar spectra from Kurucz [1979]. In section 3.4 I compare our system to ESO OmegaCAM [Iwert et al., 2006] and ESO WFI [Baade et al., 1999] and in section 5.1 I conclude with a summary.
Most of the contents of this chapter have been published in Kosyra et al. [2014] in Springer Experimental Astronomy. The authors contributed to this paper as follows: the mechanics of the instrument have been designed by Florian Lang-Bardl. The electronics have been developed by Claus Gössl, Wolfgang Mitsch and myself. The software has been programmed by Claus

Gössl. Most laboratory measurements for calibration have been performed by me, the exceptions are filter transmissivity and mirror reflectivity which have been performed by Ulrich Hopp. The first observations, used for on-sky commissioning, have been performed by Michael Schmidt and Christoph Riess. The analysis of the lab measurements and observations for calibration and commissioning was done exclusively by me (including the development of the software for analysis). Ulrich Hopp provided many ideas for data analysis, especially for the evaluation of the on-sky data. Arno Riffeser also contributed some ideas to the analysis of the on-sky data, and the software used for evaluating the data in the second part of zero point analysis (with standard stars, see 3.3.2).

3.1 Instrument design

3.1.1 Optics and detector systems

The WWFI is built around a Spectral Instruments 900 series detector system (SI900[1]) and the field corrector optics which is an integral part of the *Fraunhofer Telescope*. The optical design is based on a three elements transmissive field corrector optics and a mandatory 15 mm silica plate (or equivalent) for filters. The field corrector[2] consists of a lens doublet that is attached to the telescope flange and a field flattener lens that also serves as entrance window to the SI900 dewar. The system is designed to yield diffraction-limited images within all optical wavebands [Hopp et al., 2010, Gössl et al., 2010]. The good to excellent seeing of the site [< 0.8" median, up to 0.4" at best, Hopp et al., 2008] requires a pixel size of of $(0.2 \text{ arcsec})^2$, which is realized by a 2×2 mosaic of $(4\text{k})^2$ 15 μm pixel, back-illuminated e2v CCDs[3]. The basic parameters of the system are given in table 3.1 and a detailed discussion can be found in section 3.2. The CCDs are cooled actively by two Polycold PCC Compact Coolers[4]. The compressors for the cooling system are offloaded into a separate cabinet and supply the refrigerant by 23 m long lines which run through the telescope cable wrap.

[1] SI900 is a trademark by Spectral Instruments Inc., Tucson, USA

[2] The field corrector was produced by POG Präzisionsoptik Gera GmbH, Germany

[3] The CCDs are a trademark of e2v Inc, Chelmsford, Essex, England

[4] Polycold PCC Compact Cooler is a trademark of Brooks Automation Inc, Chelmsford, USA

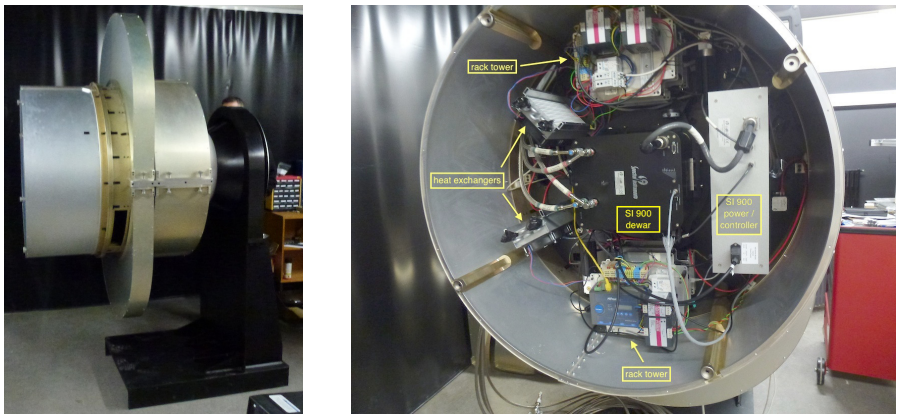

Figure 3.1: WWFI mounted on the derotator test flange in the laboratory. Left: Side view with fully assembled covers. Right: Rear view onto the partially assembled electronics section.

The system is equipped with two off-axis guiding units that pick up their light after the lens doublet in front of the main detector shutter. This results in non-flat image planes which are partially vignetted but still good enough for guiding, as it allows for guide star acquisition / guiding to be done independently from the main shutter/filter/detector system. The guider cameras were taken from a previous project[5], two Fingerlake Instruments Microline ML3041, which have $(2k)^2$, 15 μm pixel, back illuminated Fairchild CCDs 3041, use thermoelectric cooling for the detector and had their air cooled heat sinks replaced by water cooled ones.

3.1.2 Mechanics

The limited space at the observatory and the optical design yield several basic constraints to the mechanical design of the WWFI:

- It must fit inside a cylindrical volume with 1 m depth and radius and its mass must not exceed 350 kg.
- The camera has to operate at environmental temperatures in the range from $-15°$C to $25°$C without contributing to dome seeing.

[5]I.e. AMiGo, a two channel CCD-camera for the former 80 cm telescope of the Wendelstein Observatory [Gössl, 2007].

Table 3.1: Basic parameters of the Wendelstein Wide Field Imager

Global parameters	
Size (envelope)	< 1 m radius and depth cylinder
Mass	$\lesssim 350$ kg
Operating temperature	$-15°\text{C} \leq T \leq 25°\text{C}$
Power consumption	~ 1.6 kW
Optical parameters	
Telescope aperture	2.0 m
F-ratio	7.8
Field of view	(27.6x29.0) arcmin^2
Pixel scale	0.2 arcsec/pixel
Gaps	98" and 22"
Mosaic alignment	$\leq 0.13°$
Field distortion	$< 2.2 \cdot 10^{-5}$
Wavelength range	300 nm $\leq \lambda \leq$ 1050 nm
Guiding FOV	$2\times \sim$ (6.8 arcmin)^2
Main detector system parameters	
SI900 Mosaic	$4 \times$ (4k)^2 e2v 231-84 type deep depletion CCDs
Readout time (4 ports per CCD)	8.5 s at 500 kHz, 40 s at 100 kHz
Readout noise	7.8 e^- at 500 kHz, 2.2 e^- at 100 kHz
Gain	5.81 ± 0.04 e^-/ADU at 500 kHz, 0.688 ± 0.003 e^-/ADU at 100 kHz
Dark Current (at -115 °C)	0.27 e^-/h / pix
Dynamical range	16 bit
Full well capacity	> 250 ke^-/ pix
Peak QE	0.9

- The "truss" part of the WWFI covering the field corrector lens doublet has to be stiff enough to carry the whole instrument without significant flexure.
- The optical design implies that a tilt of the image plane cannot be accepted while some minor shift of the image plane during rotation will have no discernable impact on image quality. Specifications are given in Gössl et al. [2010], a description of flexion tests is given in Gössl et al. [2012].
- Since we aim at robotic operations the WWFI should provide more than 10 filter slots.
- An effective EMI protection is mandatory to ensure the system electronics to work in the strong electromagnetic fields emitted by the close by radio transmitter.
- Two off axis guiding cameras should ensure sufficient field and "lever" to correct for tracking errors of the telescope and its field derotator.

The corrector lens doublet, the double off-axis guiding units, a Bonn Shutter [Reif et al., 2005], two large filter wheels, and the SI900 detector system are aligned in a row (see Fig. 3.2). The envelope covering the instrument is designed to operate as an effective electromagnetic interference protection against the emissions of the nearby 0.5 MW radio transmitter. Figure 3.3 shows the complete mechanical design.
The WWFI is divided into three sections: The first volume is enclosed by an aluminum cast cone with eight struts directly casted to it and a mount plate with a diameter of $\sim$ 1 m. The stiff cone covers the corrector lens doublet frame and has two apertures: a small one that fits to the derotator flange and a large one which can sustain the remaining components of the camera. The "Semi- Serrurier" configuration formed by the struts avoids tilts against the optical axis of the subsequent components. The struts are massive enough to prevent all but minor shifts perpendicular to the optical axis (Fig. 3.4). The 200 mm Bonn shutter[6] and, on top of that, the two offset guiding stages are mounted at the telescope side of the mount plate.

[6]Bonn Shutters [Reif et al., 2005] are widely used for large format astronomical CCD cameras, e.g. ESO OmegaCAM [Iwert et al., 2006], Pan-STARRS-1 Gigapixel Camera [Tonry et al., 2007]. Their simple and compact twin blade design yields uniform, "photometric" exposures even for short exposures (1 ms).

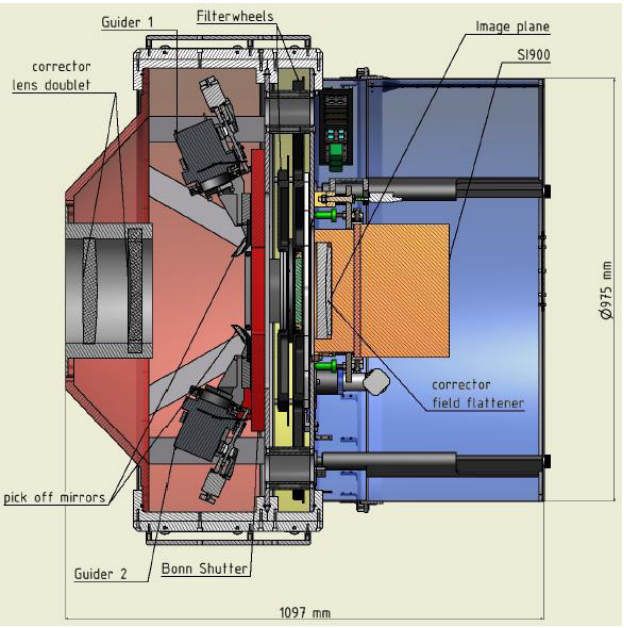

Figure 3.2: Sectional view of the WWFI. Red, yellow, and blue backgrounds show its three principal sections. See text for details. Courtesy of the figure: Florian Lang-Bardl

The guiding stages each support a pick-off mirror and an FLI Microline 3041 CCD camera[7] in a cardanic mount for manual tip/tilt adjustment on a motorized linear stage[8] for independent focusing. The stepper motors driving the linear stages are connected to ball screws and allow for a travel range of 40 mm. A precise MYCOM limit switch[9] serves as reference for initialization. The relative position is determined by counting motor steps.
The second volume holds two eight-position filter wheels in between the guider/shutter mount plate and a second mount plate for the SI900 detector system and the electronics. The two filterwheels provide the 14 slots for filters as one empty slot is needed in each wheel. The first wheel (next to the science camera) is already equipped with an SDSS filter set [*ugriz*, Fukugita et al., 1996]. The central wavelengths and spectral widths of the filters are given in table 3.2. As the distance from the filter position to the focal plane

[7]FLI Microline 3041 is a trademark of Finger Lakes Instrumentation, New York, USA
[8]The linear stages were produced by Franke GmbH, Aalen, Germany
[9]The precision switches were produced by MYCOM AG, Berlin, Germany

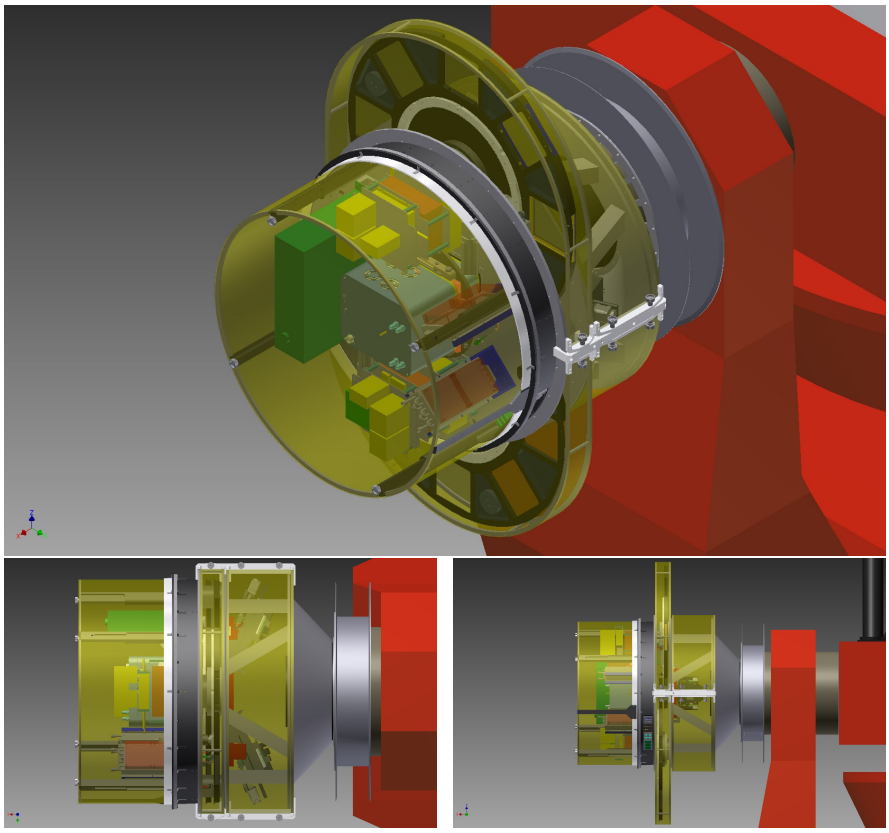

Figure 3.3: Isometric view of the WWFI (upper panel), side view (lower left panel) and another side view rotated by 90 degrees relative to middle panel (lower right panel). Courtesy of the figure: Florian Lang-Bardl

is slightly different for each wheel, the filter size is $(150\ \mathrm{mm})^2$ in the first and $(160\ \mathrm{mm})^2$ in the second filter wheel.

For now we have also installed a black metal sheet filter in each wheel to allow for additional stray light and EMI tests. The plates are attached to each other with four short thick "tubes". Two of these serve as shafts for the bearings that hold the wheels, all four can be used to feed support lines from the last section through to the first. We employ a notch mechanism for repeatable positioning of the filters. Two stepper motors attached to a gearbox with a gear ratio of 12:1 drive the wheels. The gearbox provides the torque needed to drive the system. We installed two "limit" switches to

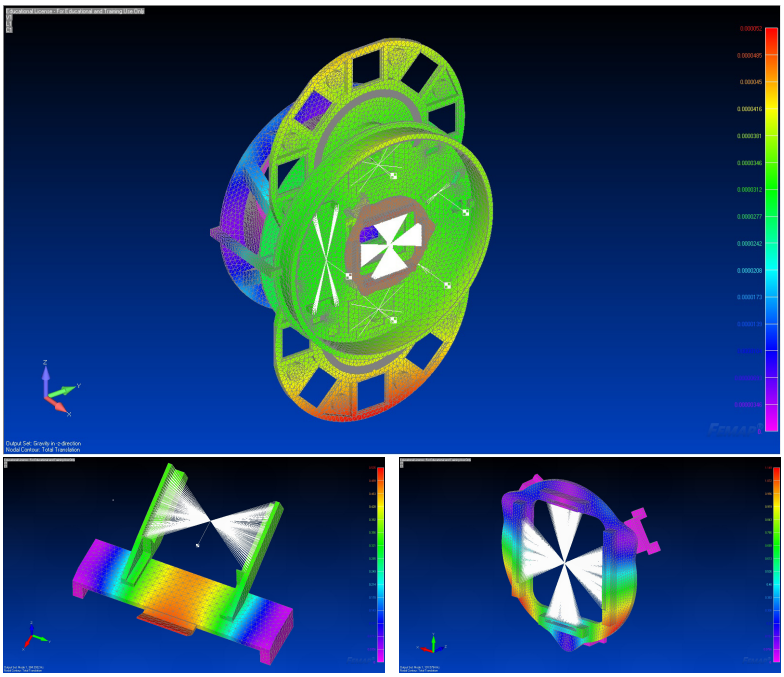

Figure 3.4: The upper panel shows an undeformated view of the total translation. Maximum displacement (red) is around 50 micron. The tilt angle of the parts in respect to the optical axis is small enough to have no influence on the optical performance. The lower panel shows the result of an eigenfrequency analysis of the guider-mount (left) and the tip-tilt stage (right). The first eigenfrequency of the tip-tilt stage is at 190Hz, the one of the guider-mount is at 380Hz. Courtesy of the figure: Florian Lang-Bardl

get information about the position of the notch itself (notch in the groove or not) and one extra switch to define a reference position[10].
The camera head and all electronics[11] needed to drive and control the WWFI components are installed at the backside of the second plate. The back focus tolerance of the telescope optical design was ±4mm. Therefore, and to allow for less tight tolerances when machining the mechanical parts, we mounted the camera head with a manual 5-axis (tip/tilt and x, y, z translation) stage

[10]See next Sect. for details on drive logics.
[11]I.e. power supplies, RS232 to Ethernet converters, thermostats, switches, motor controllers, compressor relays, and embedded control PCs.

Table 3.2: Central wavelength and spectral width of the WWFI filters.

Filter	u	g	r	i	z
$\lambda_{\text{central}}[\mathring{A}]$	3540	4770	6180	7590	8970
$\lambda_{\text{width}}[\mathring{A}]$	600	1300	1400	1400	1500

onto the plate. This electronics volume is insulated with Armaflex[12] and cooled by two liquid-to-air heat exchangers from Thermatron Engineering Inc. to minimize the contribution to dome seeing of the instrument.

The eigenfrequencies and the bending behavior of the instrument have been determined with a finite element method (FEM) analysis. Because all telescope axes (azimuth, elevation and both derotators) are driven by direct drives we had to make sure that the eigenfrequencies of the structural parts are high enough (> 50 Hz), to lower the risk of mechanical oscillations induced by the direct drive controllers. Because of the complexity of the model, the FEM analysis was split into several steps. First we had a look at subassemblies as the guider mechanism or the heat exchanger mounts. When the FEM model showed that the eigenfrequencies of the sub components are high enough, the part has been integrated as a mass point in the complete FEM model of the WWFI. By this method we ensure to have reasonable calculation times due to the reduced complexity. The only components that turned out to have eigenfrequencies low enough to possibly get excited, are the electronics mounts and the camera head. The sheet metal was damped by the Armaflex insulation we attached to it. We also put some Armaflex insulation beneath the electronics mounts to have a soft connection to the stiff structure. The lowest eigenfrequency of the supporting structure was found at 83 Hz (see Fig. 3.4).

The other value of interest is the bending behavior. It was straightforward to use the same FEM model as for the eigenfrequencies, because all the necessary parameters were already implemented (mass points for subassemblies, connections, mesh). In order to get the bending behavior, we only had to switch on gravity in different directions We were especially interested in the differential bending between the detector surface and the guider, since it may influence the guiding performance. The differential translation we found was negligibly small. The maximum total translation at the camera surface was

[12]Armaflex is a trademark of Armacell GmbH, Münster, Germany

around 50 μm (see Fig. 3.4).

3.1.3 EMI covers

The covers of the WWFI not only serve as a shield from light but also from EMI (electromagnetic interference) due to the proximity of the nearby radio transmitter station. The camera has to work within fields $\approx 20\,\mathrm{V/m}$. Without an effective shield the detector displays enhanced noise (Sect. 3.2.3) and the motor controllers for the filter wheels and offset guider focus movement just do not work at all. (They pick up too much interference from the lines to the limit/position switches to boot properly.) The 5-part cover is built from chromated aluminum sheets screwed and conductively glued onto a minimal truss. High conductivity glues have about 80% filling of silver (or a similar conductive metal) and therefore are not adhesive enough without the additional screws to hold the sheets in place. The "sharp" edges of the covers slide into light traps with conductive lip seals. The only electric lines into the camera are shielded and filtered power lines; network connection is established via optical fiber link. Hierarchized thermal switches protect the electronics from overheating in case of a cooling failure.

3.1.4 Software and control

The WWFI control software has to support and combine the different proprietary interfaces of its hardware components: The SI900 is controlled through a Windows graphical user interface (GUI, based on LabView[13]) which offers a TCP/IP socket for "backdoor" control. The FLI MicroLine 3041 guiding cameras come with a C Developer Kit for Linux. The filter wheels and offset guiding focus work through Pollux[14] high resolution positioning controllers via the Venus-2 command language on serial interfaces (which we map to TCP/IP via a Moxa NPort[15]). The Bonn shutter is directly controlled by an I/O signal from the camera but also offers additional controlling and surveillance options through a serial interface of its motor controller (again mapped to TCP/IP). For all four components we developed device programs which can be accessed by TCP/IP sockets and translate simple human readable

[13]LabView is a trademark of National Instruments Corporation, Austin, USA

[14]Pollux Controller and Venus-2 command language are trademarks of PI miCos GmbH, Eschbach, Germany

[15]Moxa NPort is a trademark of Moxa Inc., Brea, USA

commands to the explicit hardware control commands and vice versa for the messages received from the hardware. The device programs log state and optionally debug messages to a central syslog facility server which again parses a subset of those messages to provide status webpages (simple HTML) which are independent of the higher level controlling software. They also already allow for "scripted" observations which greatly enhance the efficiency of commissioning.

While the device programs were planned to map only basic functions of their respective hardware there had to be some exceptions to that rule: the motor controller of the filter wheels and its language was specifically designed for arbitrary linear movements between hard limits which is obviously almost the opposite of moving between mechanically fixed positions on a circle. Therefore, we use the position switch as a simultaneous upper/lower limit switch with the reference switch inverting the upper limit again[16]. Now, as the switches reset the position accounting within the motor controller, the device program has to count filter notches. It also has to turn off hard limits before starting moves and turn them back on while moving as active limit switches control the direction in which subsequent moves are allowed. The second exception is guiding image evaluation. As the device program already holds the images (before optionally saving them to disk) it is also the right place to evaluate them, i.e. to correct for bias / dark current, compute star positions and perform a rudimentary point spread function (PSF) analysis (second order moments). This saves bandwidth and improves performance (speeds up guiding turn around) as the higher level control instance runs on another platform.

The next layer of software represents the logically integrated WWFI control: It connects to the single device programs and again offers simple human-readable commands and messages on its TCP/IP interface to control the instrument. It allows to start / stop guiding, move filters, expose etc. while keeping track of the individual components and prohibits "stupid" mistakes (like changing filter while exposing). This layer now can not only be controlled from the command line but also via a web-browser based GUI or a robotic scheduler. Our prototype for this layer which already provides the guiding for the WWFI makes heavy use of multithreading and is implemented in Python[17] (work in progress by Claus Gössl).

[16]Because of this the initialization run has to move "backwards".

[17]Python Programming Language is a trademark of Python Software Foundation,

Table 3.3: Gain per port for the fast and slow readout mode (500 and 100 kHz), as measured in our lab.

	Gain [e^-/ADU]			
CCD	0	1	2	3
Port	500 / 100 [kHz]	500 / 100 [kHz]	500 / 100 [kHz]	500 / 100 [kHz]
1	5.87 / 0.71	5.94 / 0.71	5.87 / 0.71	5.85 / 0.71
2	5.88 / 0.69	5.85 / 0.68	5.84 / 0.70	5.87 / 0.69
3	5.76 / 0.68	5.75 / 0.67	5.73 / 0.67	5.72 / 0.67
4	5.75 / 0.68	5.78 / 0.68	5.75 / 0.68	5.79 / 0.69

3.2 Calibration and characterization

Before mounting the imager at the telescope, we need to calibrate it in the laboratory in order to enable the use of quantitative photometry. In this section, all lab measurements that I have performed with the WWFI are described and the results are presented. The tests include gain, linearity, quantum efficiency, charge transfer efficiency and charge persistence measurements.

The zero-point calibration and an on-sky calibration with stellar spectra will be presented in section 3.3.

3.2.1 Gain

The digital output signal of a CCD is typically given in *analog to digital units* (ADUs) must be converted back to electrons and then to photons in order to calibrate the system. The latter transformation (electrons to photons) is quantified by the quantum efficiency (QE), which will be described in detail in subsection 3.2.5. The conversion from ADUs to electrons is quantified by the *photon transfer gain factor* (hereafter: gain) of the amplifiers in the system, which is the topic of this subsection. A very detailed explanation of the gain can be found in McLean [2008].

Beaverton, USA

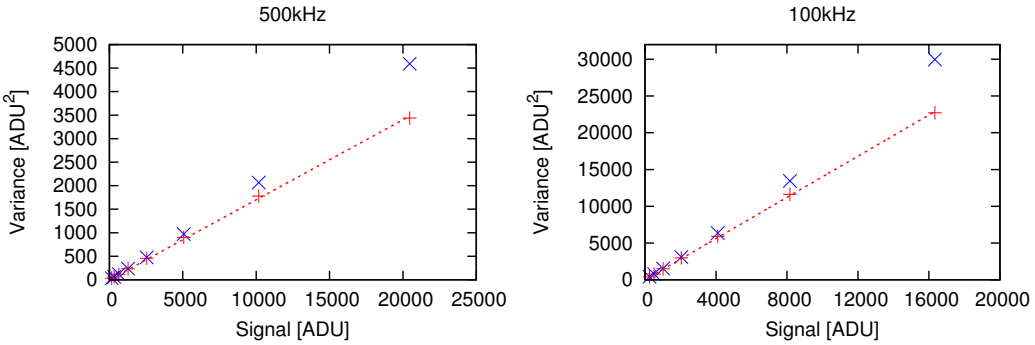

Figure 3.5: Exemplary photon transfer for the 500 kHz readout mode (left) and the 100 kHz mode (right) for CCD 0, Port 1, with the signal in ADU on the x-axis and the variance on the y-axis. The blue "×" show the uncorrected values, while the red "+" show the values that have been corrected for the noise of the masterflat. An early version of this figure is shown in Gössl et al. [2012].

The *gain* of a photon collecting device is given by the ratio

$$g = \frac{N_e}{\#\mathrm{ADU}} \tag{3.1}$$

The probably most widespread method for measuring the gain is the *photon transfer gain method*, as it is described in McLean [2008]. I adopt this method to determine the gain of the WWFI.
In principle it would be necessary to take multiple flat field images at multiple illumination levels and measure the average signal and noise for each and every pixel on the detector at each illumination level. Alternatively, I take only one image per illumination level and substitute the averaging over several images by averaging over several pixels and previously removing the pixel-to-pixel variations by dividing each image by a *masterflat* composed of 30 single flat-field images at a signal level significantly below half well capacity. Then I measure the average signal and variance of every image (one per illumination level). As the readout noise is well below the photon noise, I will neglect the readout noise for further considerations. The photon noise σ is then only source of variance σ^2 left in an image with a mean signal S, since $noise^2 = p^2 + R^2$ (with photon noise p and readout noise R).
By dividing this equation by the squared gain, the left hand side can be

expressed through the variance (in ADU) and since the photon noise p is equal to the square root of the signal $\sqrt{g \cdot S}$, we get:

$$\sigma^2 = \frac{S}{g} \tag{3.2}$$

Unfortunately, the introduction of the masterflat also causes additional photon noise. Gössl et al. [2012] introduced a method to correct for this additional noise. I adopted this method and will explain it here. The following description closely follows the derivation therein.
The relative noise in the final signal (F_i) reads:

$$\left(\frac{\sigma_{F_i}}{F_i}\right)^2 = \left(\frac{\sigma_M}{M}\right)^2 + \left(\frac{\sigma_{S_i}}{S_i}\right)^2 \tag{3.3}$$

where S_i is the mean signal in the original exposure (index i for number of the exposure), M is the mean signal of the masterflat, F_i is the mean signal in the final image (divided by the masterflat) and the σ are the corresponding photon noises. As the masterflat is normalized to 1 it can be assumed that $S_i = F_i$ and equation 3.2 can be used to obtain the following expression for the gain:

$$g = \frac{\frac{1}{F_i} - \frac{1}{F_j}}{\left(\frac{\sigma_{F_i}}{F_i}\right)^2 - \left(\frac{\sigma_{F_j}}{F_j}\right)^2} \tag{3.4}$$

for any indices $i \neq j$, for all pairs of data points. The gain is now estimated by equation 3.4, to determine the (relative) photon noise in the masterflat via equation 3.2, which is then subtracted in equation 3.3 to obtain the true photon noise, corrected for the contribution of the masterflat. Figure 3.5 shows the photon transfer functions for the 500 kHz (top) and 100 kHz (bottom) readout mode, with blue "×" for uncorrected values and red "+" for values corrected for the noise of the masterflat. The gain has finally been determined as the slope of the linear fit to the corrected values. Table 3.3 shows the gain for both readout modes for all ports and CCDs.

Relative gain calibration

While the absolute gain determination is not better than a few % flat-fields are used to adjust the gains within one detector to be consistent to each other

to better than 0.05%. Usually flatfielding would take care of those minor differences as a per port individual multiplicative gain factor is applied to both flat-field and science images and therefore cancels out. But adjusting gain levels helps us overcome differential bias level fluctuations at the $0.3e^-$ level. Clipped averages of almost adjacent rows/columns[18] are used for correction factors. The "almost" is because the CTE (see Sect. 3.2.9) is affecting the last read out rows/columns enough to give overall wrong correction factors if those were used.

3.2.2 Bias level calibration

As mentioned before the bias level and even its offset between serial overscan[19] and the image region is not stable to more than about $0.3e^-$. The resulting "small" steps between different ports within one detector can yield rather large distortions of the isophote shapes of extended objects (galaxies) which fill more than one quadrant of a detector. Since the gain ratios have been calibrated within one detector we can apply the same principle again for scientific images with big enough regions of low flux levels at the port boundaries (for medium to higher flux levels $\sqrt{\text{flux}[e^-]} \gg 0.3\,e^-$ the steps are irrelevant). Median clipped averages of the directly adjacent rows/columns are used here to derive and correct for the remaining bias offsets between the detector ports.

3.2.3 Readout noise

There are three types of noise present in CCD images:

- The intrinsic noise of the system amplifier is called *readout noise*, it is a constant value.
- The *photon noise* is governed by Poisson statistics and is therefore proportional to the square root of the illumination.
- The *pixel noise* is caused by pixel-to-pixel variations of the quantum efficiency. It is a linear function of the signal level.

[18] We used the third row/column next to the border.

[19] Three overscan regions are read from each port: Serial pre- and overscan, as well as parallel overscan. The serial overscan displays the smallest and most stable offset to the image region in bias and dark frames.

Table 3.4: Average gain and readout noise measured in the lab (USM), by the manufacturer (SI) and typical values measured at Mt. Wendelstein without EMI-shield (WST) and with EMI covers (WST-shield). The values of the readout noise show clearly that the presence of the radiation raises the noise drastically (by about 50%), but the EMI-shield mitigates this effect (for slow readout even completely). The readout noise varies less than 0.2 ADU for lab and EMI protected frames, but can change for several ADU between different not EMI protected frames on site.

Readout mode	Gain [e^-/ADU] USM	SI
500 kHz	5.81 ± 0.04	5.89
100 kHz	0.688 ± 0.003	0.72

Readout mode	Noise [e^-] WST	WST-shield	USM	SI
500 kHz	12.4	8.0	7.8	8.1
100 kHz	3.3	2.2	2.2	2.4

A detailed description of the noise types in a CCD can be found in Janesick [2001].

As the readout noise is the only type of noise that appears in bias frames (it is independent of signal level), it is straightforward to use these frames to determine the readout noise.

Firstly, I calculated the median value and standard deviation σ of all pixels in a bias frame. Then I rejected all outliers outside of 5σ around the median value, to get rid of defective pixels, and calculated the mean and new standard deviation with this "clean" image. The standard deviation is a measure for the readout noise of the CCD. I repeated this procedure for all 16 ports of the WWFI. Table 3.4 shows the average values of the readout noise for both readout modes measured in our lab compared to the results of the manufacturer.

The values measured in our lab are systematically lower than the ones achieved by SI. The reason for this are the slightly lower gain values we measured.

I also checked the noise difference in the laboratory and on-site with and without the electromagnetic shielding. The results show that the noise on-site is about 50% higher due to the strong radiation, but the shield mitigates

this effect (for slow readout even completely).

Quantization noise

Additionally, I checked the contribution of the charge quantization to the readout noise: I found no difference in the fast readout mode, while in the slow mode I measured a quantization noise of 0.02 electrons, which is negligible for all our applications.

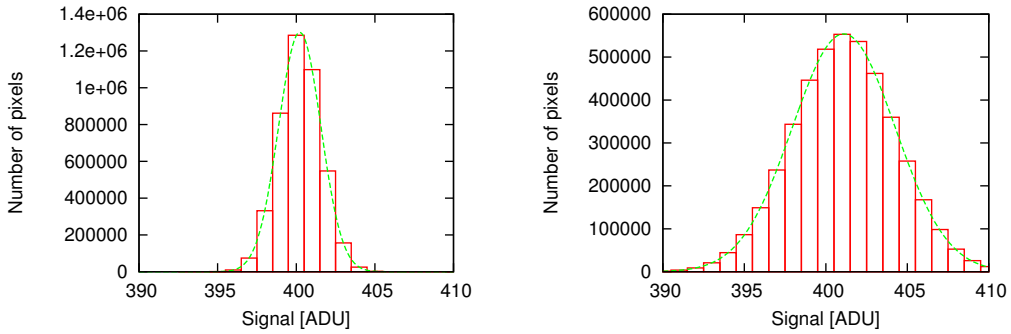

Figure 3.6: Histogram of the signal of a bias frame. Measured data in red, Gaussian fit is green. If the FWHM of the Gaussian is larger than the noise (as calculated in the previous section), this indicates the presence of quantization noise. Left: fast readout mode, right: slow readout mode.

3.2.4 Linearity

To first order, the response of a charge coupled device is linear, as each photon with the same wavelength has the same probability to be detected (quantum efficiency, see sect. 3.2.5). When looking more closely, the detection probability of a given pixel is a function of the amount of charge currently captured in the well of that pixel. Two distinct effects are responsible for this behavior:

1. As the charge in a pixel approaches the full-well capacity, the Coulomb-repulsion between the electrons becomes relevant. This causes newly generated free electrons to be eventually deflected by this repulsive force and not ending up in the well of the pixel, at whose surface they were generated. The magnitude of this effect depends on the exact position of the generated electron, as electrons near the pixel borders are easier deflected than charges near the center of a pixel.

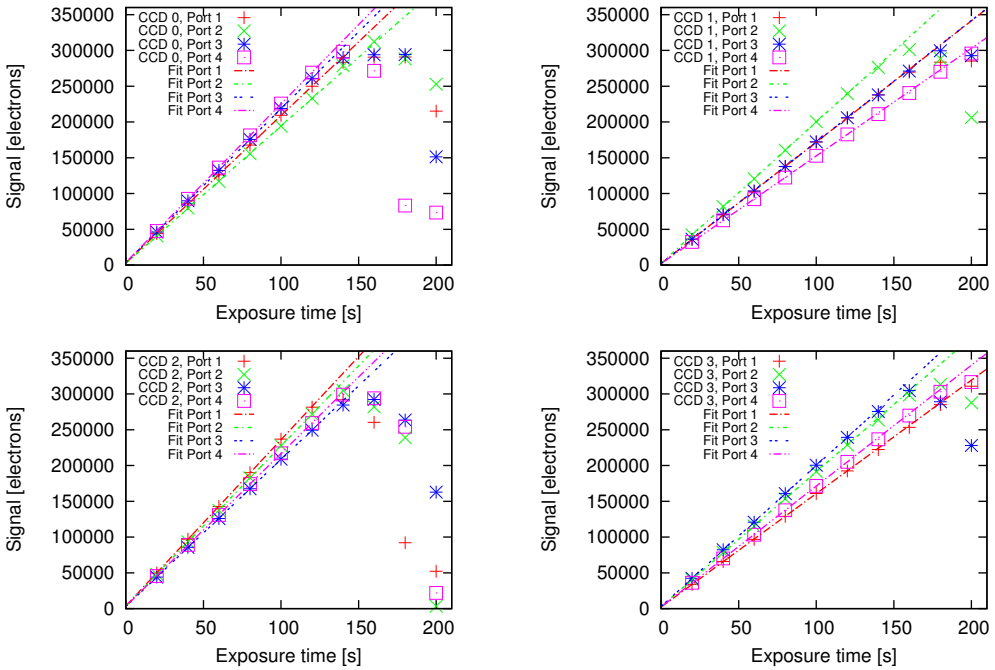

Figure 3.7: Signal versus exposure time at constant illumination. The four subfigures represent the four CCDs, while each color represents one port. The linear response regime of the CCDs can be quantified by determining the point where the signal first deviates from linear correlation.

2. The more free electrons are created, the more holes are left behind. This leads to finite recombination probability as the charge in a pixel increases. Electron-hole pairs that recombine before the readout process sets in do not contribute to the signal, so the linear characteristic of the response is suppressed by this effect.

A more detailed introduction to CCD-linearity can be found in Janesick [2001] and in McLean [2008].

However these effects become relevant only as the charge in a pixel approaches the full well capacity, resulting in a non-linear response at high illumination levels. I tested the linearity of response of the WWFI by taking a series of flat fields with varying exposure time in the lab with a constant, stable light source (same setup as described in section 3.2.5). The results of this

Table 3.5: Minimum guaranteed full well capacity of each port of the WWFI in units of ke^-.

CCD	0	1	2	3
Port	Full well capacity [ke^-]			
1	120	160	120	120
2	160	120	160	180
3	120	120	120	140
4	180	140	140	160

measurement in figure 3.7 show a minimum guaranteed[20] linearity in the "worst" ports of $\sim 120ke^-$ in some ports even up to $\sim 180ke^-$.

3.2.5 Quantum efficiency

In a CCD, charge carriers are generated by the photoelectric effect, i.e. a photon is being absorbed, transferring an electron from the valence band to the conduction band of the semiconductor, leaving behind an electron-hole pair. This process is referred to as *charge generation*. The free electrons that are produced in this process are then collected in a quantum well that is defined by the electric potentials on the chip. This process is called *charge collection*. Both of these processes have a finite efficiency, as on the one hand not every incident photon will be absorbed to generate a charge carrier, and on the other hand a newly generated free electron does not necessarily find its way into the quantum well of the pixel where it was created. The efficiencies of these two processes are called *charge generation efficiency* and *charge collection efficiency*, respectively.
For the calibration of a detector it is not necessary to know each of these two efficiencies, but it is enough to know the resulting efficiency of these two, called *quantum efficiency* (QE). The QE is the fraction of photons incident on the surface of the detector that produce charge carriers that are collected within the same pixel's quantum well. It is measured in terms of electrons per photon and is a function of wavelength.
Next, I describe our method to measure the QE in the laboratory and compare our results for all four chips with the results obtained by the CCD

[20] I define the last data point that is in agreement with the linear fit as the minimum guaranteed value for the end of the linear regime.

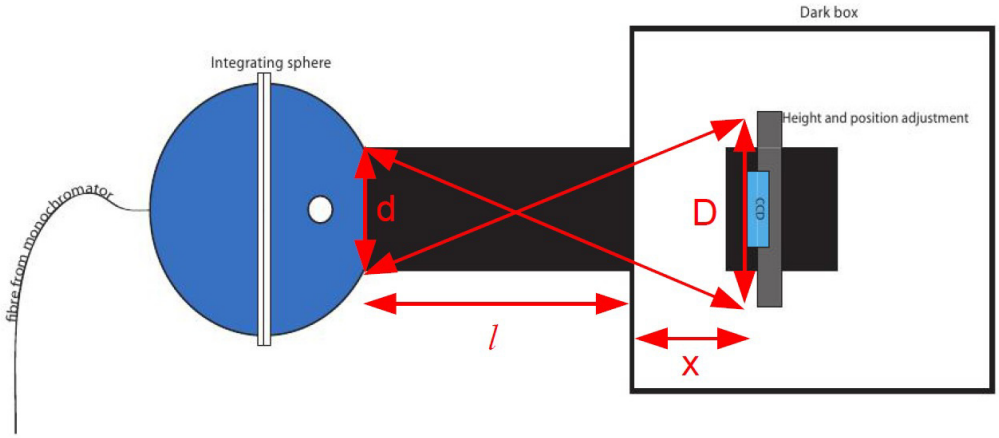

Figure 3.8: Sketch of test setup with integrating sphere and darkbox

manufacturer e2V.

The setup

For measuring the QE of a detector, a homogeneously illuminated area at least as large as the collecting area of the detector, which in our case is $\sim$ (15 cm)^2, is required to ensure a homogeneous illumination of the CCDs (as a flat field image). I used a 100 W white halogen lamp as source of illumination. The light is fed into a reversely operated double monochromator[21] for wavelength selection. The monochromatic light then enters an integrating sphere (via an optical fiber) which randomizes the direction of the light rays and creates a uniformly illuminated source. The flat light from the sphere passes through a tube with a diameter of 30 cm to a large darkbox where the detector is mounted at a distance that corresponds to a focal ratio of $f/7.8$, which is the same as at the Fraunhofer telescope in order to simulate the incident angles as they are at the telescope site. I use an absolutely calibrated photodiode to measure the absolute amount of photons per unit area arriving at the camera plane in the dark box. Figure 3.8 shows a sketch of the integrating sphere and the darkbox.

[21] The exit and entrance slits of the second monochromator in the row are reversed, resulting in a reduced straylight.

Measurement

I measured the quantum efficiency of the camera in the wavelength region 340 - 1000 nm, in 20 nm steps up to 900 nm and in 50 nm steps above 900 nm. Five images were taken at each wavelength, with an exposure time just high enough that the average amount of counts is something around 10000 ADU. Additionally, a single dark frame was taken for each exposure time.

Data analysis

The definition of the gain is given in equation 3.1 and the definition of the quantum efficiency of a detector reads:

$$\mathrm{QE} = \frac{N_e}{N_{\mathrm{phot}}}, \tag{3.5}$$

with $N_{\mathrm{phot}} = \dfrac{P \cdot t_{\mathrm{exp}} \cdot \lambda}{h \cdot c}$ (where P is the power of the incident light $P = \frac{dE_{phot}}{dt}$ and I is the photodiode current) and the spectral response of the photodiode $\mathrm{SR} := \dfrac{I}{P} \Rightarrow P = \dfrac{I}{\mathrm{SR}}$ and the transmissivity of the entrance window T_{win} we obtain:

$$\mathrm{QE} = \frac{g \cdot \#\mathrm{ADU} \cdot \mathrm{SR} \cdot h \cdot c}{I \cdot t_{\mathrm{exp}} \cdot \lambda \cdot T_{\mathrm{win}}}. \tag{3.6}$$

Since the detection area of the photodiode (A_{pd}) is not equal to the active area of a single pixel in the CCD (A_{pix}), we need to multiply the equation by the ratio of these two areas:

$$\mathrm{QE} = \frac{g \cdot \#\mathrm{ADU} \cdot SR \cdot h \cdot c}{I \cdot t_{exp} \cdot \lambda \cdot T_{win}} \cdot \frac{A_{pd}}{A_{pix}}. \tag{3.7}$$

All quantities and parameters that are used in this derivation are summarized in table 3.6. There are two problems arising in our setup concerning the reference measurement with the photodiode: firstly, the measurements with the CCD and the diode should in principle take place simultaneously, or to be more exact, the time interval between the measurements must be shorter than the time in which the illumination from the lamp changes significantly. The current of power supply of the halogen lamp is stabilized and therefore provides a constant illumination over a time period of a few hours, so the time interval between the measurements should be much less

than that, which we cannot realize in our setup. Secondly, incident light at the camera plane is very faint. At short wavelengths (where the spectral response of the photodiode is low) it is therefore not possible to measure a significant current with the diode, as the signal drowns in the noise. At the surface of the integrating sphere however, the illumination is higher by approximately a factor 100. I solved these problems by measuring the diode current at the surface of the integrating sphere simultaneously with the CCD measurement, and then, since we need to know the illumination level in the camera plane, introduced a second measurement determining the light level in the sphere and (nearly) simultaneously in the camera plane. With the two values from the latter measurement, I generated a calibration factor that is equal to the ratio of the illuminations in the sphere and at the camera plane:
$c_f = \frac{L_{\mathrm{sphere}}}{L_{\mathrm{camera}}}$
The illumination ratio can also be estimated by geometrical considerations: Let d be the diameter of the tube through which the light leaves the integration sphere, D denotes the diameter of the illuminated area in the camera plane, l is the length of the tube and x is the distance of the camera from the front wall of the dark box (see red lines and arrows in Fig. 3.8). All of these quantities can be measured directly except for D which can be calculated: $\frac{D}{l/2+x} = \frac{d}{l/2}$ or $\frac{D}{d} = 1 + \frac{x}{l/2}$. The illumination on the surface of the integrating sphere is proportional to $\frac{1}{d^2}$ while the illumination in the camera plane is proportional to $\frac{1}{D^2}$, so the ratio of illuminations is equal to $\frac{D^2}{d^2}$. With the numbers from our setup $x = 89\ cm$, $d = 30\ cm$ and $l = 80\ cm$ we get an illumination ratio of 10.4. The (wavelength-averaged) illumination ratio from our measurement is 33 which means that we lose more than a factor 3 more light than we expect from our (simple) estimation. Remembering that inside of the sphere all angles of light rays are present, while in the camera plane there are only light rays under steep angles given by the geometry (the flat angles hit the inside of the tube which is black and will absorb the most), it becomes instantly clear that our simple approximation underestimates the illumination ratio by an amount which is given by the geometry (i.e. the minimum acceptance angle of light rays incident at the camera plane).
This ratio enters the equation for the QE as a linear factor:

$$\mathrm{QE} = \frac{g \cdot \#\mathrm{ADU} \cdot \mathrm{SR} \cdot h \cdot c}{I \cdot t_{\mathrm{exp}} \cdot \lambda \cdot T_{\mathrm{win}}} \cdot \frac{A_{\mathrm{pd}}}{A_{\mathrm{pix}}} \cdot c_f \tag{3.8}$$

To zeroth order, the calibration factor c_f does not depend on wavelength.

Table 3.6: Quantities used in QE equation.

QE	quantum efficiency of CCD
g	gain (ratio of electrons per ADU)
#ADU	number of analog to digital counts
SR	spectral response of the photodiode in $\frac{A}{W}$
h	Planck's constant
c	speed of light
I	current of the photo diode
t_{exp}	exposure time of the image
λ	wavelength
A_{pix}	area of one pixel
A_{pd}	area of the photodiode
c_f	correction factor for the distance from the integrating sphere

When looking more closely we recognize the differences in the angle dependencies of the spectral response of the photodiode for different wavelengths, e.g. at long wavelengths the effective cross section of the diode becomes larger for flat angles[22], while at short wavelengths a larger fraction of the light is being reflected at the surface for flat angles. This means in our case that the calibration factor c_f depends on the wavelength, since inside the sphere the diode sees light coming from all angles, while in the dark box only steep angles are arriving at the diode. I tried to overcome this problem by measuring c_f for wavelengths in between 400 nm and 1000 nm, extrapolating for wavelengths below 400 nm (since it is not possible to measure any signal with the diode in the box below 400 nm, as the faint signal is in the same order of magnitude as the fluctuations of the dark current).
Figure 3.9 shows the QE curves measured in the USM laboratory (red, green, blue, purple, for the four CCDs) and by e2v (cyan). It can clearly be seen that our lab measurement yields a slightly higher QE than the one from the manufacturer, nearly over the complete spectral range. I consider our results as reasonable, as the curve from e2v is not an individual detector measurement, but rather a minimum guaranteed curve. The only exception is

[22]At large wavelength the penetration depth in silicon is larger, so photons are not absorbed at the surface but in the bulk

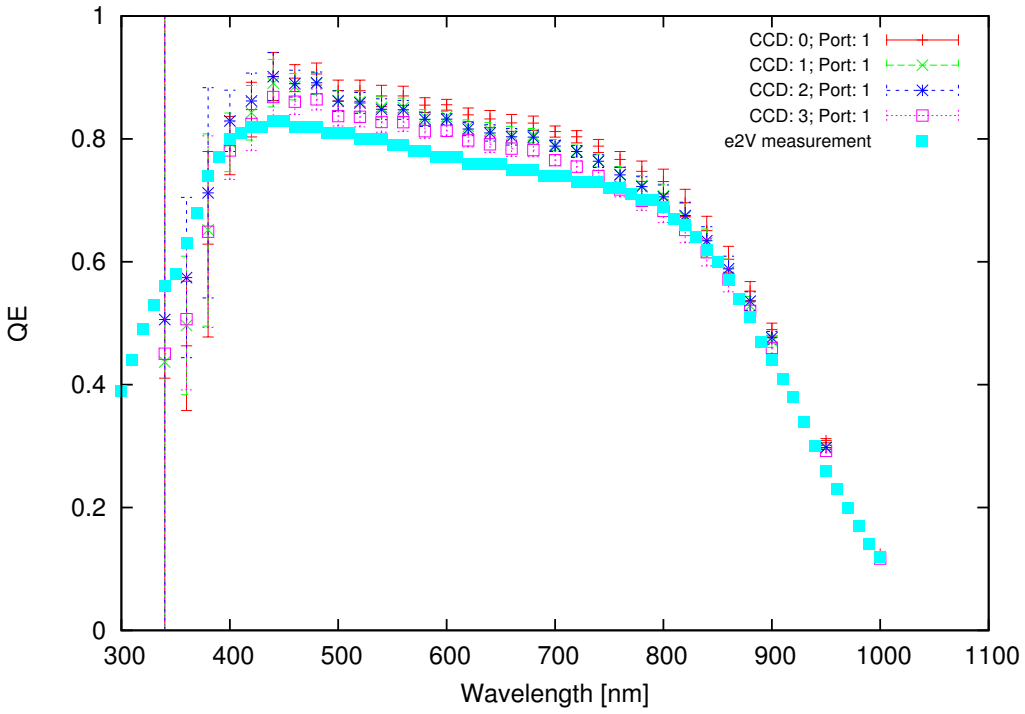

Figure 3.9: Quantum efficiency of the four chips of the wide field imager measured in the lab of the USM (red, green, blue, purple), as well as the minimum guaranteed curve by e2v (cyan).

at wavelengths <400 nm, where the results from our measurement are lower. However, the results agree within the error margins that are significantly larger in this region due to the very low photodiode currents.

3.2.6 Filter transmission

The transmissivity of the optical filters[23] [following the SDSS-system: *ugriz*, Fukugita et al., 1996] has also been measured in our laboratory. The measurement setup used the same light source and double monochromator described in Sect. 3.2.5, but this time without the integrating sphere since large flat fields are not needed. Instead, the light from the monochromator is illuminating the photodiode directly through the filter inside a dark box. The diode current is measured for the light transmitting the filter and once without filter as a reference to obtain the transmissivity. This procedure was repeated for nine different equally distributed positions on the filter, giving the average as the value for the filter transmission. There is no significant variation between the nine positions. The measured transmission curves are shown in Fig. 3.10 (green lines).

3.2.7 Total efficiency

Following the aim to predict the on-sky performance of our camera, that means to predict the number of ADUs detected when observing an object of a known magnitude in a given filter, we need to characterize the total efficiency of the system. Now I put the together following pieces of the puzzle:

- Quantum efficiency of the detector (see Sect. 3.2.5).
- Transmission curve of each filter (see Sect. 3.2.6).
- Transmission of the field corrector, which consists of three lenses.
- Reflectivity of the primary, secondary and tertiary mirror.
- Extinction in the atmosphere, including the contributions from Rayleigh scattering, ozone absorption and aerosol scattering, as in Bindel [2011].

[23] The filters were manufactured by Omega Optical Inc, Brattleboro, USA

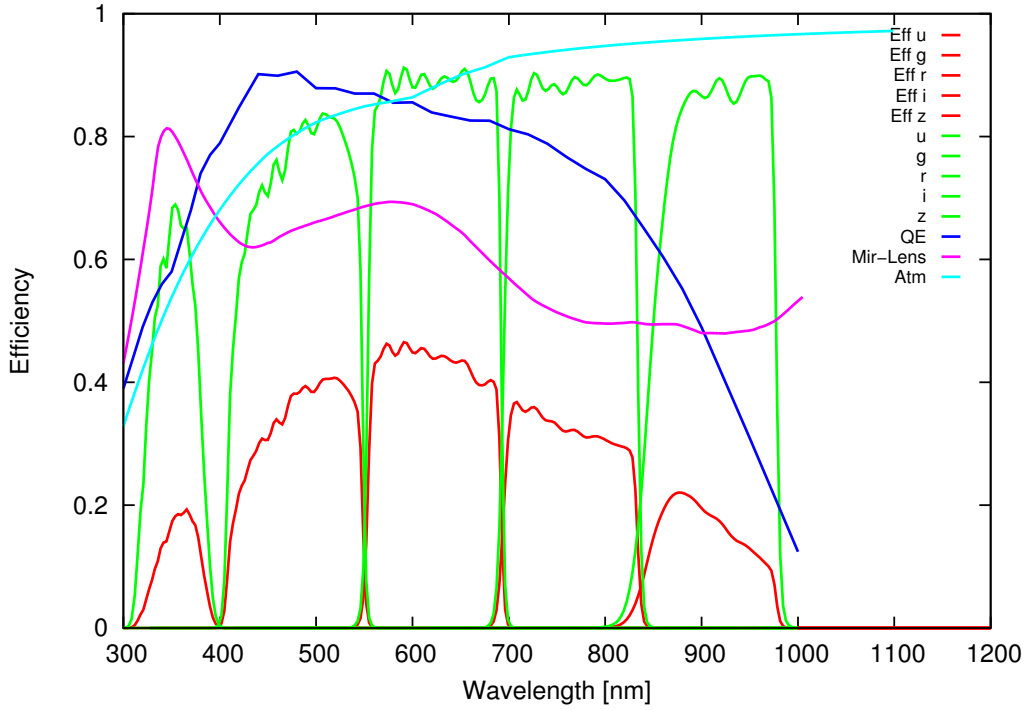

Figure 3.10: Total Efficiency of the WWFI (CCD 0, Port 1) in *ugriz* filters (red), filter transmission (green), QE of the detector (blue), combined corrector transmission and mirror reflectivity (all three, purple), combined atmospheric transmission at airmass unity (Rayleigh, ozone and aerosol, cyan).

With the total efficiency known one can calculate the number of photons incident to the Earth's atmosphere from the number of counts in a CCD image.

Due to the large statistical error of our QE measurement at wavelengths smaller than 400 nm (see Fig. 3.9) we decided to use the manufacturer's QE below 400 nm and our own measurement above this value as the "true" QE, as displayed in Fig. 3.10 (blue curve). Fig. 3.10 shows that the QE (blue curve) of the detector is only of minor importance regarding the total efficiency, while major contributions come from the mirrors and lenses (purple curve) at long wavelengths and from the atmospheric extinction (cyan curve) at shorter wavelengths. For the z-band, however, the total efficiency is dominated by

the QE curve of the detector, which falls steeply for wavelengths $\gtrsim 850$ nm. The contribution from ozone absorption is negligibly small (but has been considered here), while Rayleigh and aerosol scattering both contribute a significant fraction to the total efficiency, especially at short wavelengths. Since the aerosol abundance on Mt. Wendelstein is not known, I followed Bindel [2011] who assumed that the abundance is comparable to that at Fred Lawrence Whipple Observatory on Mt. Hopkins at an altitude of 2617 m [Hayes and Latham, 1975].
Table 3.7 shows the limiting AB magnitudes[24](with apertures of 1.1") of objects with which a signal-to-noise ratio of 5.0 can be achieved with five exposures with an exposure time of 360 s each (cumulative exposure time of 1800 s), taking into account all system parameters and assuming unity airmass and a PSF with FWHM of 0.8", according to the median seeing of the site at mount Wendelstein.

Table 3.7: Predicted system throughput Q and signal to noise ratio for a given AB magnitude in each filter for the WWFI for 5×360 s exposures, combined $\hat{=}$1800 s, PSF with FWHM 0.8", aperture 1.1" at airmass 1.0.

waveband	u	g	r	i	z
Q	0.201	0.363	0.415	0.325	0.155
night sky AB	22.80	21.90	20.85	20.15	19.26
S/N	5.0	5.0	5.0	5.0	5.0
AB mag	24.88	25.46	25.00	24.43	23.60
zero point	24.25	25.41	25.36	24.87	23.54

3.2.8 Charge persistence

The detector of the WWFI is operated at a temperature of -115°C. At these low temperatures the thermal energy of the electrons is so low that electrons that are trapped in lattice defects have escape times of $\sim$ several hours. When a pixel is oversaturated, the traps will be filled with charges and the long escape times cause a "bleeding" effect as the charges are released during subsequent exposures or readouts. These *persistent charges*, also called *residual images* can be divided in two different forms: Residual

[24]Following the definition by Oke and Gunn [1983].

surface images (RSI) and residual bulk images (RBI). RBI are only caused by photons with a high penetration depth, thus they generally occur only when the chip is illuminated by radiation with wavelengths greater than 700nm. RSI can be caused by illumination of any wavelengths. RSI and RBI can be distinguished by their appearance: RBI cause persistent charges only in the pixels that were illuminated, while RSI cause the complete column (parallel to the readout direction) to bleed. If one observes bleeding columns with a spot somewhere which is bleeding stronger than the rest of the columns, both RSI and RBI are present. A very detailed explanation of this effect can be read in Janesick [2001].
Janesick and Elliott [1992] state the decay time to be exponentially dependent on the temperature of the CCD. Therefore, I have investigated whether the presence of residual images may hamper the performance of our detector.
Janesick [2001], Janesick and Elliott [1992] and Barrick et al. [2012] state that one can get rid of residual (surface) images in backside illuminated CCDs by inverting the clock voltage during readout, but unfortunately since we bought the detector system as a "black box" we have no access to the detector electronics and are not able to adjust these parameters. So we have to live with that problem and provide a useful workaround to the observer, which is what I try to do in this section.

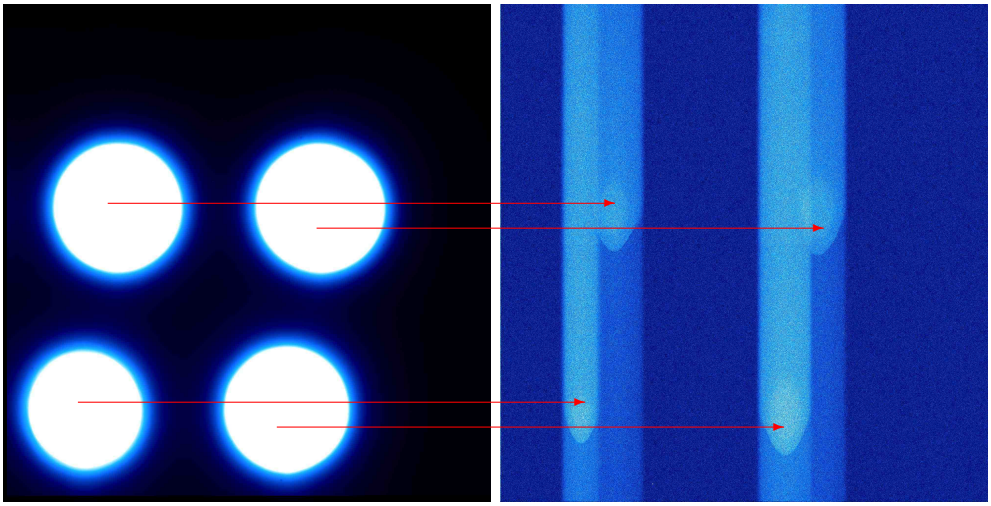

Figure 3.11: Left: Image of four oversaturated spots. Right: the same region of the detector in a dark frame directly after the oversaturation. The overscan is on the top, the serial register at the bottom of the picture.

Figure 3.11 shows four oversaturated spots on one port of one CCD (left), and a dark frame taken immediately after saturating (right). In the dark frame the trails caused by the residual surface images can be seen very clearly. The trails away from the serial register (above the oversaturated region) are brighter than the trails towards the serial register (below). The reason for this is that pixels farther away from the shift register are shifted across the saturated region during readout where they "catch" charges from the bleeding pixels.
Additionally, the figure confirms the presence of RSI (presence of bleeding trails) as well as the absence of RBI (the saturated regions do not bleed stronger than the trails).

Method

A mask with 64 small holes (hole diameter 1mm) has been mounted in front of the detector and a stabilized white LED has been used to generate defined oversaturated regions on the detector (16 per chip, 4 per port). We oversaturated the spots on the detector defined by the mask, then took a dark frame immediately afterwards and repeated this procedure 10 times (of oversaturating and taking a dark frame), where the only quantity that changes is the exposure time of the dark frame. In other words I was measuring the integrated value of decaying charges. I also took as series of *real* dark frames (beforehand, without residual images) for dark-subtraction. The signal in each spot has been analyzed in a centered square of 20×20 pixels, while the diameters of the spots are approximately 100 pixels. In order to characterize the effects of persistent charges, I performed several measurements with the following varying parameters:

- the chip temperature,
- the amount of oversaturation that we defined as the charge in units of the full-well capacity, and
- the wavelength of the incident light.

Data analysis

I quantify our results by plotting the exposure time of the dark frame on the horizontal axis and the total charge on the vertical axis, such that the

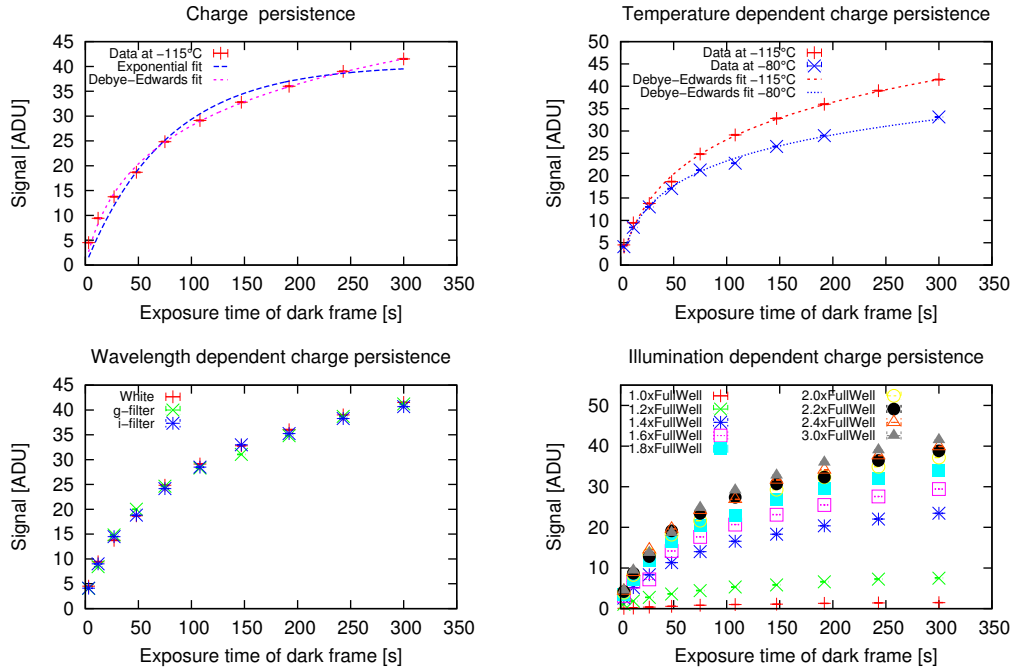

Figure 3.12: Top left: Integral plot of persistent charges with exponential fit (blue) and Debye-Edwards fit (magenta). Top right: the same at −115°C (red) and −80°C (blue) with Debye-Edwards fits. Bottom left: the same for different wavelength regions: white light (red data points), SDSS g filter (green) and i filter (blue). Bottom right: the same for differing degrees of saturation, from 1× full well capacity up to 3× full well. All plots with exception of the top right one are at −115°C.

derivative of these functions represents the charge decay. I fitted an integrated exponential function as well as an integrated Debye-Edwards type decay function [as proposed in Barrick et al., 2012] with a power-law exponent of 1,

$$F = \frac{A_0}{t + A_1} + A_2, \tag{3.9}$$

to our data, where F is the decaying charge, A_0 is the amplitude, A_1 gives the variability with time and A_2 represents the contribution of the dark current to the signal. The latter is equal to 0 in our case, since a dark frame of identical exposure time has been subtracted from each image.
In the top left panel of Fig. 3.12 the total charge in the dark frame taken

directly after saturation as a function of (dark) exposure time is shown. The temperature of the CCD was set at −115°C and the oversaturation is three times the full well capacity. The green curve shows an exponential fit and the blue curve shows a Debye-Edwards fit. It can be clearly seen that the fitting by the Debye-Edwards function works better, which tells us that the charge decay does not take place independently for each electron, but is a function of the amount of trapped charges. I assume at this point that the electrostatic repulsion between the trapped charges is responsible for the decay of charges, but this requires further investigation. The top right plot in Fig. 3.12 shows the persistent charges for a CCD temperature −115°C (red) and −80°C (green). As expected, we see a faster rate of charge decay at the higher temperature. The bottom left graph of Fig. 3.12 shows the residual images for different wavelength regions of incident light, i.e. white light, an SDSS *g* filter and an SDSS *i* filter[25]. I cannot confirm a dependence of the charge decay time on the wavelength of the incident light, i.e. it does not matter how deep the radiation penetrates into the pixel. This proves that there are no residual bulk images, which should show up only in the *i*-Filter, since only radiation with wavelengths greater than 7000 $\mathring{A}$ penetrates deep enough into the bulk to create them. This result is in agreement with Janesick [2001], who states that residual bulk images do not show up in backside illuminated devices. It also confirms our conclusion from figure 3.11 that there are no RBI as they would manifest in bleeding spots, but we only observe bleeding trails. In the bottom right panel of Fig. 3.12, the persistent charges are plotted for several levels of oversaturation in units of the full well capacity. We identify an obvious dependence on illumination, that is especially distinct at values slightly above full well capacity.
In order to characterize this dependence I plotted the residual signal vs. the *oversaturation level* (in units of full well capacity, Fig. 3.13) for three different (dark) exposure times (1 min: red, 5 min: blue, 60 min: magenta). The data are well fitted by an exponential function, as shown in Fig. 3.13.

$$S(I) = a \cdot \left(1 - e^{-bI}\right) + c \tag{3.10}$$

I is the oversaturation level in units of full well capacity, $S(I)$ is the persistent signal in ADU in the subsequent darkframe, b is the time constant and $a + c$ is the maximum (asymptotic) value for infinite saturation.

[25] g filter: $\lambda = 4770\ \mathring{A}, \Delta\lambda = 1300\ \mathring{A}$, i filter: $\lambda = 7590\ \mathring{A}, \Delta\lambda = 1400\ \mathring{A}$

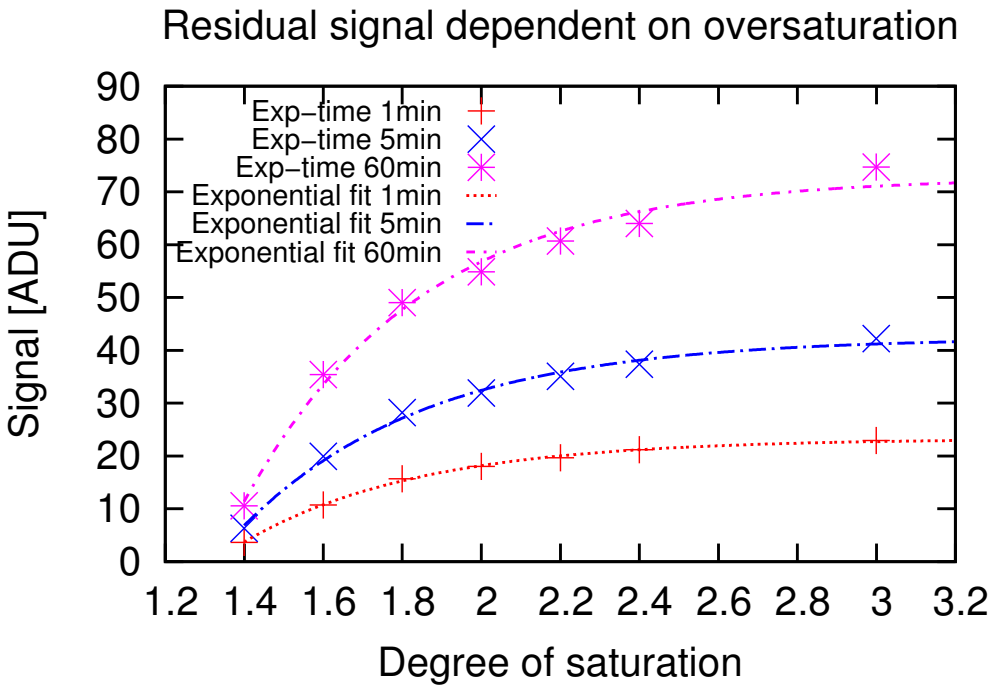

Figure 3.13: Residual signal vs. *oversaturation level* (defined as the charge per pixel in units of the full-well capacity) for three different exposure times of the dark frame (red: 1 min, blue: 5 min, magenta: 60 min), where the dark frame was taken immediately after saturation.

The best fit parameters for the three exemplar exposure times are given in table 3.8.

Table 3.8: Fit parameters of the exponential fit to the persistent charge data in dependence of oversaturation level. The lines correspond to the exposure times of the subsequent dark frame. The rightmost column ($a + c$) is the maximum asymptotic value for infinite oversaturation.

Parameter Exposure time [s]	a [ADU]	b	c [ADU]	$a + c$ [ADU]
1 min	2260	2.2	-430	1830
5 min	3090	2.12	-650	2440
60 min	4550	2.04	-1020	3530

For further treatments of the persistent charges I use the asymptotic maximum of the exponential fit (i.e. the worst case, given as $a + c$ in the table).

Dealing with persistent charges

There are several possible ways of dealing with residual images:

1. Run the detector at a higher temperature.
2. Pre-flash (saturate) the detector before each sky exposure.
3. Mask oversaturated regions for a defined amount of time.
4. Prevent saturation, which is impossible for a wide field imager.

The red, green, blue and magenta lines in the left plot of Fig. 3.14 show the charge persistence for different *waiting* times between oversaturation and beginning of the following exposure (with no wiping between the exposures). Comparing these to the signal from the night sky background in the current filter gives us the time we should mask out the oversaturated region.
The right panel of Fig.3.14 shows the persistent charges and the dark current of the detector at two different temperatures. It can clearly be seen that raising the temperature of the detector to accelerate the decay of persistent charges is not an option since the dark current rises by a factor greater than 1000 when changing the temperature from $-115°$C to $-80°$C.

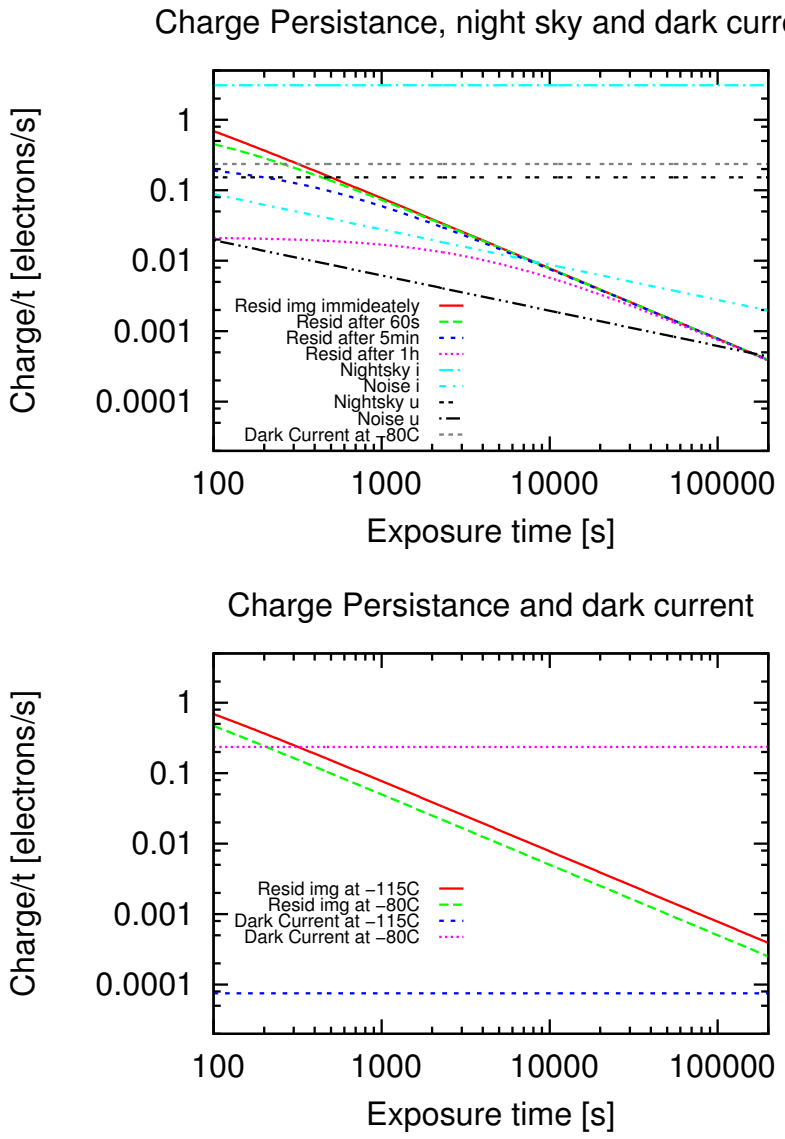

Figure 3.14: Top: Plot of the persistent charge vs. exposure time of the subsequent image (not the integrated form as in fig 3.12, but in units of $\frac{e^-}{s}$), for an image taken immediately (red), 60 seconds (green), 5 minutes (blue) and 1 hour (magenta) after saturation compared with the night sky background and its noise in the i filter (cyan) and u filter (black) and the dark current at a chip temperature of $-80°$C (the dark current at the operating temperature of $-115°$C is not shown since it is extremely low at about $0.27\frac{e^-}{h}$ and therefore not relevant). Both axes are logarithmic. Bottom: This plot has the same axes as the left plot, but shows persistent charges for two different temperatures (for the *immediate* case only) compared with the dark current at the same temperatures.

Pre-flashing the detector would require a light source that illuminates the detector area homogeneously. Furthermore, it is in principle the same as raising the dark current and noise (by the needed amount to let residual images *disappear* in the dark), so it is slightly preferable over a warmer detector, but still not an ideal solution.
Masking of the oversaturated regions sounds like a method that is easily realized, but there are two problems that have to be solved: Firstly, one has to decide for how long one wants to mask the bleeding regions. By looking again at the left plot of Fig. 3.14, it becomes clear that the amount of time has to depend on the filter of the next exposure (since the level of the night sky background depends on the filter). Secondly, it is not an easy task to decide which regions of the detector are saturated, since the detector saturates in terms of electrons, but not in terms of ADUs. This implies an overflow resulting in low ADU values again at illumination above saturation. We decided to go for the masking solution, since it leaves most of the detector area usable without adding an artificial signal (and noise). A still open task is now to develop an algorithm that finds saturated regions reliably: Before the overflow effect sets in, the signal will be constantly rising with illumination level, so if one finds a closed ring of pixel maxima, one can tell for sure that everything inside this ring is saturated. This method will be used to find saturated regions, and flag these regions in subsequent images (depending on the time interval between the exposures and the filter used in the subsequent image). The observer can then decide whether to discard the flagged regions.

3.2.9 Charge transfer efficiency

The process of shifting the charges from one potential well to the next by clocking during readout is not perfect: charge carriers can be left behind in the originating pixel by either:

1. The fact that the gate is opened a finite time, and the processes that drive the charges from one well to the next have finite time constant (happens even in an ideal lattice), or

2. the trapped charges in lattice defects that are released later during readout. This effect is mainly an issue in space-based detectors, as they are exposed to large amounts of cosmic rays that create more and more lattice defects over time.

In this section I present the results of our measurement of the *charge transfer efficiency* (CTE) and characterize the dependence of the CTE on the illumination level. CTE is defined as the number of charges arriving at the target pixel during a single shift, divided by the number of charges departing from the original pixel. Analogously, one defines the *charge transfer inefficiency* (CTI) as :

$$\mathrm{CTI} = 1 - \mathrm{CTE} \tag{3.11}$$

The effects that are responsible for the CTI are described in detail for example in Janesick [2001], and will be summarized here.

Origin of charge transfer inefficiency

There are three effects that are responsible for the shift of charges from one pixel to the next [from Janesick, 2001]: thermal diffusion, self-induced drift and a fringing field effect. A specific time constant can be assigned to each of these mechanisms, and based on this, the contribution to CTI can be calculated for each transfer mechanism.
Thermal diffusion is always present, its time constant τ_{th} depends on the temperature of the lattice:

$$\tau_{\mathrm{th}} = \frac{L^2}{2.5 D_n}, \tag{3.12}$$

with gate length L and the (temperature dependent) diffusion coefficient D_n. The contribution to CTI from diffusion transfer is given by:

$$\mathrm{CTI}_D = e^{-\frac{t}{\tau_{\mathrm{th}}}}. \tag{3.13}$$

Thermal diffusion dominates when the charge packets are small.
Self-induced drift is caused by the electrostatic repulsion of the charges inside a potential well, and it becomes important when the charge packets are large. Its specific time constant reads:

$$\tau_{\mathrm{SID}} = \frac{2L^2 C_{\mathrm{eff}}}{\pi \mu_{\mathrm{SI}} q Q}, \tag{3.14}$$

where C_{eff} is the effective capacitance, μ_{SI} is the electron mobility, Q is the number of electrons per unit area for the charge packet and q is the elementary charge. The resulting contribution to CTI is:

$$\mathrm{CTI}_{\mathrm{SID}} = \left(1 + \frac{t}{\tau_{\mathrm{SID}}}\right)^{-1}, \tag{3.15}$$

which does not depend exponentially on time, but has a 1/time dependence because the field strength that causes the repulsion decreases as the charges are shifted. This means that the self-induced field decreases until thermal diffusion takes over.
Fringing field drift mainly affects charges near the border of the potential well and is therefore dominant in pixels with small gates and becomes less dominant when the size of the charge packet approaches full well, since it depends on the potential difference between the phases. The fringing field time constant is given by:

$$\tau_{\mathrm{FF}} = \frac{L}{2\mu_{\mathrm{SI}} E_{\mathrm{min}}}, \tag{3.16}$$

where E_{min} is the minimum electric field strength under the gate. The contribution to CTI from fringing field drift is:

$$\mathrm{CTI}_{\mathrm{FF}} = e^{-\frac{t}{\tau_{\mathrm{FF}}}}. \tag{3.17}$$

These effects will be found even in ideal CCDs. In real CCDs however, bulk traps will capture charges and release them after a time that is governed by an exponential decay with a time constant of the individual trap. This trapping effect produces deferred charges and can also contribute to CTI. It is especially critical in space missions, since the detectors on satellites are exposed to a much higher dose of radiation which increases the trap density over time.
A very common method to describe the contribution of traps to CTI is described in Rhodes et al. [2010]: It is assumed that there are several populations of charge traps in the chip, each population is characterized by its own density and characteristic decay time. The decay times are characteristic of the detector material [Rhodes et al., 2010, assumes three different populations]. This results in a distribution of traps at different energy levels (trap heights) in each pixel. If the *filling height* of a pixel is equal to or greater than the trap height, this individual trap will be occupied by a single electron. If (after one or several pixel shifts) the *filling height* of the pixel is again lower than the trap height, the charge will be released after the specific decay time of the trap. The specific decay time of the traps governs how many pixels *behind* the trapped charge will be relocated (this is of course a stochastic process).

The CTI causes a distortion of image shapes along parallel and serial readout direction (there is CTI in the serial register as well), since the amplifier assigns the deferred charges to another pixel. In fact, the deformation of images in both directions depends on the parallel and serial CTE and on the amount of parallel and serial shifts the charge undergoes until it reaches the readout amplifier. An otherwise perfect PSF is no longer circular. This may become important for applications where one wants to measure image shapes, as in the analysis of weak gravitational lensing. The effect of CTE on image shapes is further in investigated in Rhodes et al. [2010].
Generally, CTE becomes better at higher illumination levels, since the time constant of self-induced drift τ_{SID} [Janesick, 2001] becomes smaller for larger charge packets [26] . At very high signal levels (around half-well and higher), CTE can again become worse because the time constant of fringing fields τ_{FF} becomes larger [26] [Janesick, 2001]. Below that point, CTI can generally be described by a power law dependent on signal level:

$$\mathrm{CTI} = a \cdot \mathrm{signal}^b, \tag{3.18}$$

with b generally $\sim -1.0 \cdots - 0.5$.

Method

There are several different methods for measuring the CTE. A relatively straightforward method, which is both qualitatively and quantitatively useful, is to take a series of flat field images at different light levels and *overscan* the serial and parallel registers to produce an image that is several pixels larger on both axes than the actual detector. If the CTE would be 1.0, one would measure just bias level in the overscan region. In real CCDs with CTEs slightly lower than 1.0 the light level in the first row (or column, in case of serial register) of the overscan region is slightly above the bias level depending on the value of the CTE. The CTE can be obtained as follows:

$$\mathrm{CTE} = 1 - \frac{I_{n+1}}{I_n \cdot n}, \tag{3.19}$$

where I_{n+1} is the mean intensity in the first row (column) of the overscan, I_n is the intensity in the last row (column) of the active region and n is

[26] These arguments are true for ground based detectors only, where traps are usually not an issue.

the number of transfers necessary to read the complete image (equal to the number of pixels per column (row)). This method is called *Extended Pixel Edge Response*, and is described in more detail in McLean [2008] and Janesick [2001] among several other methods.

Results

The top graph in Fig. 3.15 shows the parallel CTI (red) compared to the serial CTI (blue) vs. the light level in the last light sensitive line (column). The data can be described by a power-law. At illumination levels below $10000e^-$ the serial CTI is higher than the parallel one by a constant factor of approximately 1.5, at higher illumination the serial CTI deviates from the power-law. A possible explanation for this is that the signal level might approach the full-well capacity here, which would cause the CTI to become larger again. The middle graph in Fig. 3.15 shows the parallel CTI for the fast (red) and slow (blue) readout mode, indicating that there is no difference. The bottom graph in Fig. 3.15 shows the serial CTI for the fast (red) and slow (blue) readout mode. In this section I present only the results of one of the camera's CCDs (number 0). For the complete results and a comparison to the manufacturer's results I refer the reader to App. A.

We do not expect any problems with photometry as the CTI values of the WWFI are very low.

3.3 Commissioning

The commissioning phase of the WWFI started in August 2013. First observations included M31, several globular clusters and Landolt standard star fields [Landolt, 1973, 1983, 1992, 2009] for photometric calibration. In this section I will give an overview of the reduction of the WWFI data and present first photometric zero points from observations of globular cluster M13 and from Landolt standard star fields. Furthermore I present an analysis of the system throughput based on stellar spectra by Kurucz [1979] and Castelli et al. [1997], presenting predicted instrumental magnitudes for objects based on their spectral energy distributions.

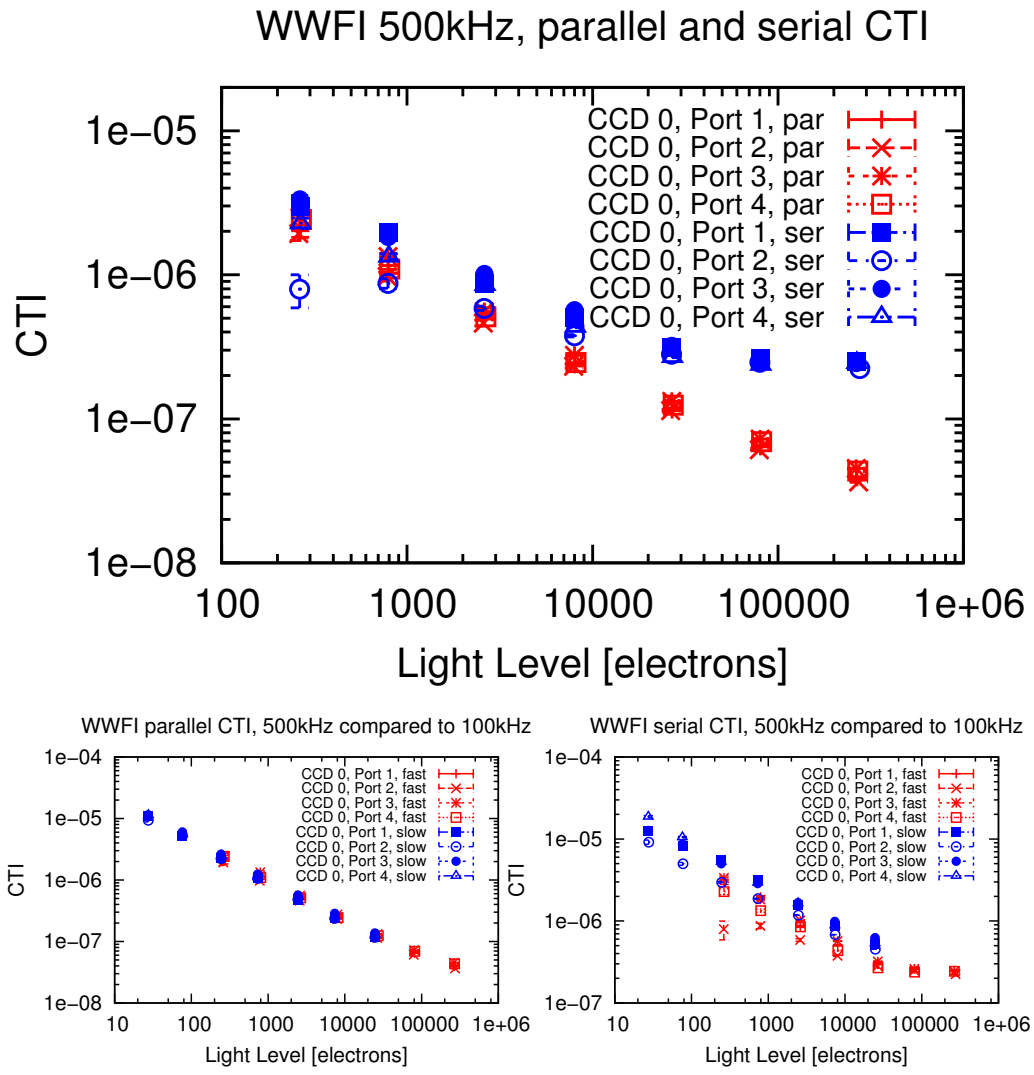

Figure 3.15: Top: Parallel CTI (red) compared to serial CTI (blue) in the 500kHz readout mode in dependence of illumination, for one CCD of the WWFI. Bottom left: Parallel CTI in the 500kHz mode (red) compared to parallel CTI in the 100kHz mode. Bottom right: Serial CTI in the 500kHz mode (red) compared to serial CTI in the 100kHz mode.

3.3.1 Data reduction

The standard data reduction of WWFI images uses the *fitstools* package [Gössl and Riffeser, 2002]. The first step in the data reduction process is to split the image according to the four CCDs. I then follow the standard recipes of bias and dark subtraction and flatfield correction, as well as cosmic ray removal with *cosmicfits* from *fitstools*. The *fitstools* package is also able to create error frames based on shot noise, read noise and gain and propagate these error frames properly through each step of data reduction. The final reduced images, including their corresponding error frames can then be fed into any photometry software for source detection.

3.3.2 Photometric zero point

The photometric zero point (ZP) is defined as the magnitude of an object that produces a charge of exactly one electron in an exposure of one second in an instrument. It quantifies the transmissivity of the system. Due to atmospheric variations the zero point may be different in each image taken. I used the first on-sky data taken with the Wendelstein *Fraunhofer Telescope* of the globular cluster M13[27], and with data from one night of the Landolt standard star fields SA95[28], SA97[29] and PG0918[30] to measure the zero point of the WWFI. In this subsection I describe our method of calculating the photometric zero point from the data of the two observations, present the results, compare them to each other and examine how good they agree with theoretical predictions from an exposure time calculator.

Zero points from M13 data

The first step is to reduce the data according to the method described earlier in this section. After data reduction we obtained aperture magnitudes with $1.5''$ diameter[31]by running SeXtractor [Bertin and Arnouts, 1996] on the images (in u, g, r, i and z band) with a detection threshold of 3σ for 4 contiguous pixels.

[27]Exposure times M13: u: 60 s, g: 20 s, r: 10 s, i: 20 s, z: 40 s

[28]Exposure times SA95: u: 60 s, g: 10 s, r: 10 s, i: 10 s, z: 20 s

[29]Exposure times SA97: u: 30 s, g: 10 s, r: 10 s, i: 10 s, z: 10 s

[30]Exposure times PG0918: u: 60 s, g: 30 s, r: 30 s, i: 30 s, z: 30 s

[31]I chose this small aperture to avoid errors induced by crowding effects, and extrapolated the magnitudes later on to an aperture of $10.0''$ with 23 isolated bright stars in the

I matched our detected stars to the lists published by An et al. [2008] and also used their catalogs for reference magnitudes to calculate the zero point using the equation:

$$ZP = m_{\mathrm{lit}} - m_{\mathrm{inst}} + AM \cdot \kappa - 2.5\log(t_{\mathrm{exp}}) + 2.5\log(g), \tag{3.20}$$

where m_{lit} is the magnitude from the catalog of An et al. [2008] in the AB photometric system, m_{inst} is the (uncalibrated-calibrated) instrumental magnitude, AM is the airmass which was 1.08 in our observation, κ is the atmospheric extinction coefficient, for which I used the average approximated values from Bindel [2011][32], t_{exp} is the exposure time and g is the gain of the detector (the estimated values for the extinction are given in table 3.9).
To minimize systematic errors we only accepted stars with:

- Literature magnitude <19.
- Distance from center of M13 >350″, in order to reject stars with bad photometry due to crowding effects in the center of the globular cluster.
- Magnitude error <0.1 (from SeXtractor run).

In general, when measuring an instrument's zero point with stars of known magnitudes, the published catalogs have not used exactly the, same filters as the own instrument. This results in a color-dependent correction term to the zero point, which takes the general form:

$$ZP(\mathrm{color}) = ZP_0 + a \cdot \mathrm{color} + b \cdot \mathrm{color}^2 + ..., \tag{3.21}$$

where ZP_0 is the zero point at color 0, a is the linear color term, b is the quadratic color term and so on. When the filters of the two instruments are truly identical[33], all color terms are zero. For similar filters, the color terms are expected to be small, resulting in negligibly small higher order terms. When we plot the zero point in each filter for each individual star versus a color (Fig. 3.16), we find a linear dependence as expected, as the catalog published by An et al. [2008] uses AB-magnitudes in an SDSS filter set as well. The linear color terms found are very small.

outer region of the field.

[32]Since we have only a single observation in each filter per airmass, I was not able to calculate the extinction.

[33]Exactly spoken, not only the filters but all wavelength dependent components in the system, like detector QE, mirrors and so on, have to be identical in terms of wavelength dependence.

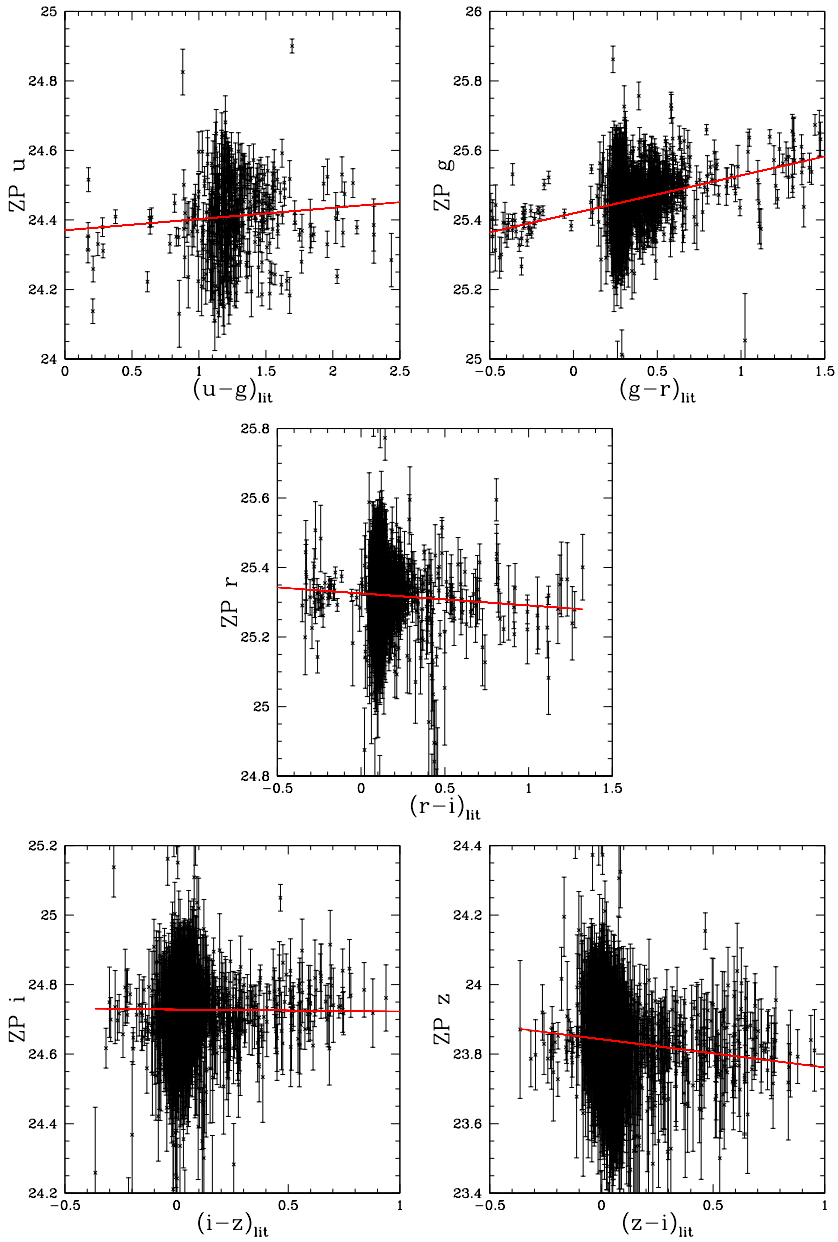

Figure 3.16: Zero point (average over all 4 CCDs) from M13 data (in the AB-system) plotted vs. (literature) color with linear fit to obtain the average zero point at color 0 and the corresponding color term. Top left: u band ZP vs. $u-g$, top right: g band ZP vs. $g-r$, middle: r band ZP vs. $r-i$, bottom left: i band ZP vs. $i-z$, bottom right: z band ZP vs. $z-i$; the scatter comes from the shallow depth of the observations and possibly also from variable sources in the catalog from An et al. [2008].

Table 3.9 shows the results of our zero point calculation. I will discuss these at the end of the following subsection.

Zero points from Landolt standard star fields data

I used the Landolt standard star fields SA95, SA97 and PG0918 [Landolt, 1973, 1983, 1992, 2009] to measure the zero point again independently from the method explained above, with two exposures per filter in SA95 and SA97 each and one exposure per filter in PG0918 for a total of five airmasses for the calculation of the extinction coefficient. The procedure of data reduction and application of photometry by SeXtractor is the same as described in the previous subsection, with the one exception that I used aperture diameters for photometry of $10.0''$ from start, since I did not have to deal with a crowded field here. The main advantage over the previous method is the availability of observations at multiple airmasses and thus the possibility to fit the extinction coefficient for the particular night, rather than relying on average empirical estimates for the atmospheric extinction.
The first step is to determine the extinction coefficient (in each filter) by applying a linear fit to all stars that are detected at at least two airmasses. Fig. 3.17 shows the magnitude difference between the literature magnitude and the instrumental magnitude vs airmass in the i filter. Each blue dot represents the magnitude difference for a single star at given airmass. Each red line is a separate linear fit to each single star at all available airmasses. The slope of each fit is the extinction coefficient measured from that particular star. The average extinction coefficient results from a global fit to all the star multiplets simultaneously.
I investigated the possibility of a variable extinction coefficient throughout the night by comparing the magnitudes of stars dependent on time. I found a constant extinction coefficient for each filter except the u-filter, where I estimated the systematic error from varying extinction to be 0.05 mag. I added this error to the flux error in our analysis in order to obtain a better fit for the zero point in the u-filter.
After correcting for the extinction, our photometric catalogs are matched with the standard star catalogs from Landolt [1973, 1983, 1992, 2009]. Since the WWFI is using a filter set that is similar to SDSS [*ugriz* Fukugita et al., 1996] and the Landolt catalog uses Johnson-Morgan (U, B, V) [Johnson and Morgan, 1953] and Cousins (R_C, I_C) [Cousins, 1976] filters, we have to compare our magnitudes to the literature magnitudes taken from the nearest

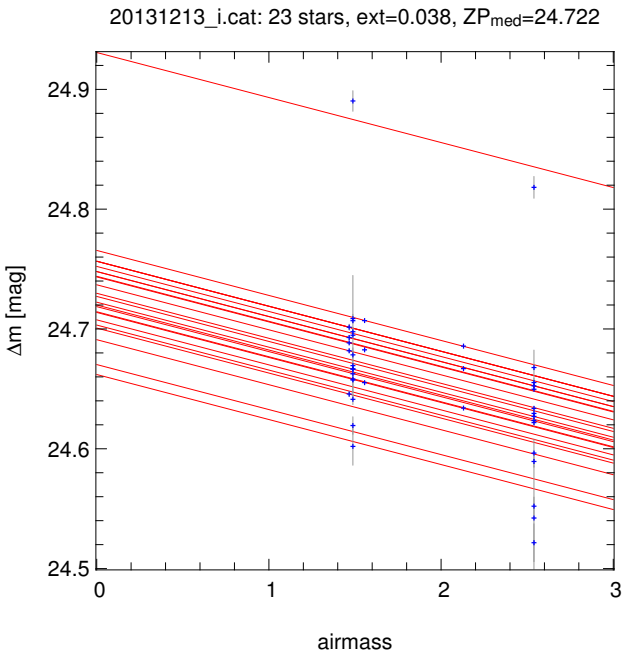

Figure 3.17: Difference between literature magnitude and WWFI instrumental magnitude vs airmass (i filter). The red lines are linear fits to each star separately at different airmasses. The slope of the fit is the extinction coefficient.

(in terms of central wavelength) filter from the Landolt catalog, which results in larger color terms. Therefore, I compared our u with U, our g with V, our r with R and our i with I. I found that the filters are "similar enough" that a linear color term is sufficient to correct for the differences (Fig. 3.18). Unfortunately there is no adequate filter in the Johnson-Morgan and Cousins system to compare our z filter with, so I limited this analysis to u, g, r and i. All magnitudes in the Landolt catalog, which are given in the Vega-system, have been transformed to AB-magnitudes for our analysis.
In the near future, the photometry from the PanStarrs survey will be available for most of the northern sky in the SDSS filter system, which will be a great opportunity to redo this kind of analysis without having the problem of converting between two photometric systems.
After the matching has been completed, I calculated a zero point for each matched star via eq. 3.20 and applied a linear fit to the results in dependence of color (according to eq. 3.21), in order to determine the color term and zero

point at color 0.

Figure 3.18 shows the results of the linearly fitted zero points over color, and Table 3.9 summarizes the results of this measurement and the one from the previous subsection and compares them to our theoretically predicted values based on our laboratory results. The underlying exposure time calculator that was used to compute the theoretical zero points based on the lab calibration, will be explained in appendix B. Table 3.9 shows that there is an overall good agreement between our two measurements, the deviations are always within the margins of error. The measured and observed values are in very good in agreement in the g and r filter while in the u filter the agreement is a little worse, most probably due to the large uncertainties in the laboratory calibration at short wavelengths arising from low illumination. In the i and z filters the discrepancy is still a little larger (0.14 and 0.15 respectively), and since the statistical error in this wavelength region is small, I conclude that this arises most probably from systematic errors in the lab calibration.

Table 3.9: Theoretical zero points as obtained by the exposure time calculator compared to the ZPs measured on M13 data. All ZPs are in the AB photometric system.

waveband	u	g	r	i	z
ZP calculated	24.25	25.41	25.36	24.87	23.96
ZP measured M13	24.37	25.42	25.33	24.73	23.84
ΔZP M13	0.12	0.072	0.091	0.091	0.11
color term M13	0.032	0.109	-0.035	-0.0055	-0.081
color	u-g	g-r	r-i	i-z	z-i
extinct. estimated M13	0.56	0.18	0.10	0.08	0.07
number of stars M13	382	1376	1482	1726	1807
ZP measured Landolt	24.34	25.36	25.33	24.73	
ΔZP Landolt	0.037	0.018	0.069	0.031	
color term Landolt	0.019	-0.916	-0.228	-0.241	
color	U-B	V-R	V-R	R-I	
extinction Landolt	0.495	0.160	0.092	0.038	

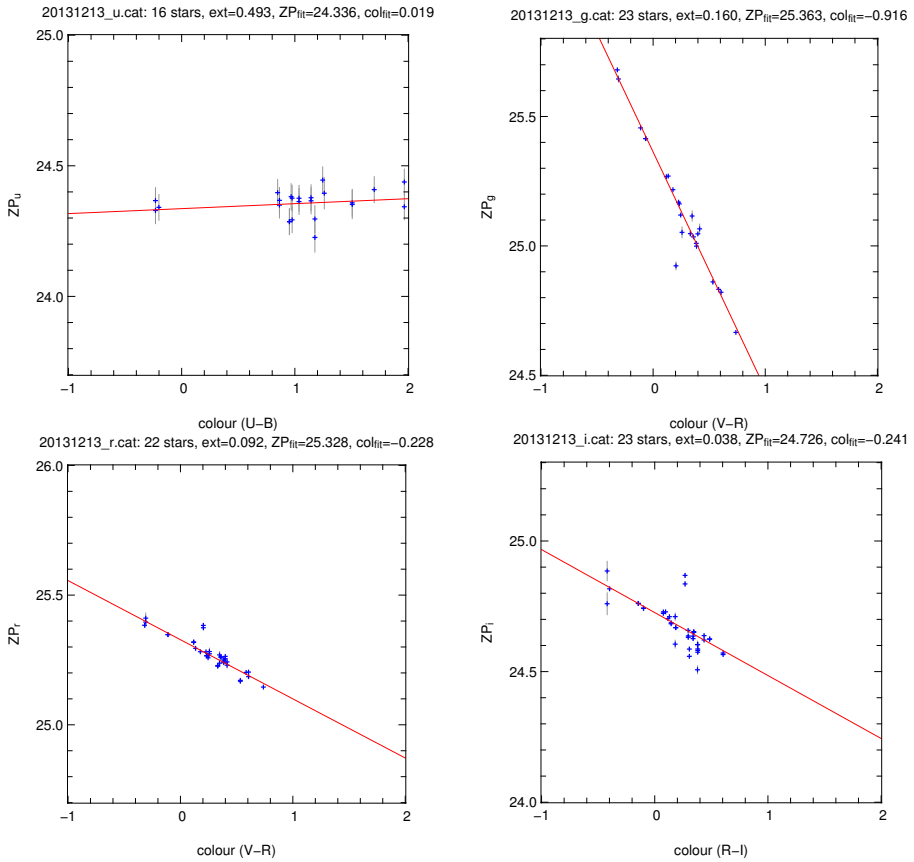

Figure 3.18: Zero points (in the AB-system) vs. colors from our standard star analysis. Top left: u band ZP vs. U-B, top right: g band ZP vs. V-R, bottom left: r band ZP vs. V-R bottom right: i band ZP vs. R-I.

3.3.3 Throughput

The throughput of a system is defined as the amount of photons detected by the instrument divided by the amount of photons incident at the telescope aperture in a given filter. The left plot of fig. 3.19 shows the SEDs of a number of types of stars and galaxies. The galactic SEDs can be described by a superposition of stellar SEDs. The right plot shows a color-color diagram that would result if these objects are observed with the WWFI.
In this section I predict the instrumental magnitudes of objects in our system depending on their SEDs. I use the same set of observations of M13 as described in Sect. 3.3.2, since a globular cluster is very well suited for this

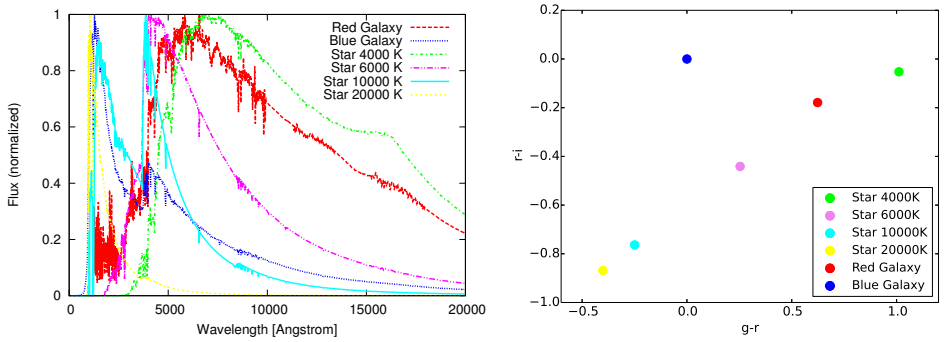

Figure 3.19: Left: Normalized spectra of four stars and two galaxies. The stellar spectra are taken from the Kurucz ATLAS 9 and have effective temperatures of 4000K (green), 6000K (purple), 10000K (cyan) and 20000K (yellow), solar surface gravity and low metallicity. The galactic spectra resemble a typical red and a typical blue galaxy. Right: The same objects as in the left plot (also in the same colors) in a color-color diagram when imaged with the WWFI. No interstellar or intergalactic absorption is considered here.

kind of analysis because it consists of stars of approximately the same age and metallicity, thus on the same isochrone. To obtain theoretical magnitudes for comparison I used the synthetic stellar SEDs from Kurucz ATLAS 9 [as described in Castelli et al. [1997], available on the CD-ROM No. 13 of Kurucz [1993] based on the initial grid from Kurucz [1979]] and the isochrones from Girardi et al. [2004]. Since the Kurucz spectra are on a grid spaced by 0.5 in $\log(g)$ and by 250 K at low temperatures (and more coarsely at higher temperatures) it is not possible to assign a separate SED to each entry of the isochrone. Thus, I interpolated linearly in $\log(g)$ and $\log(T_{\rm eff})$ to estimate the SED for each isochrone entry. The so found SEDs were then convolved with the instrumental efficiency curve measured in our lab (as presented in Fig. 3.10 red curve) for each filter, to find the instrumental magnitudes we expect these stars to have with our camera. Then I corrected these magnitudes for the distance modulus of M13 [14.44 ± 0.06 from Buckley and Longmore, 1992] and for the interstellar extinction[34]. These theoretical magnitudes are then plotted into a color-magnitude diagram and compared to the observational data, as shown in Fig. 3.20. The black empty squares in the

[34]From the Schlafly and Finkbeiner [2011] recalibration of the Schlegel et al. [1998] dustmap.

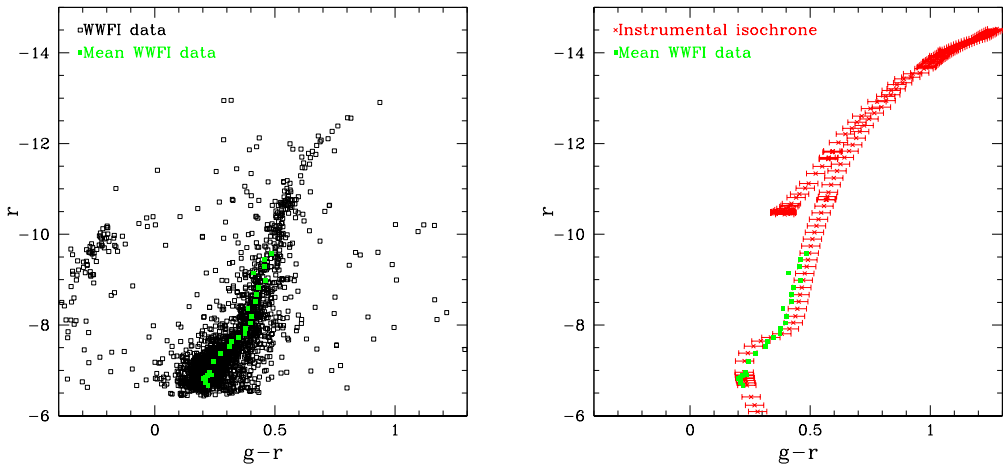

Figure 3.20: Instrumental color-magnitude diagrams, with $g - r$ color on the x-axis and r band magnitude on the y-axis. Left: Black empty squares are data points from the observation and green filled squares represent the ridgeline (color-averaged) of these values. Right: Red crosses are expected magnitudes based on our lab-results (explanation see text) and green filled squares are again the ridgeline of the observational values.

left panel represent the observational data, the red crosses in the right panel are the expected magnitudes (based on our lab data, the Kurucz-spectra and the isochrone) and the green filled squares in both panels represent the ridgeline of the observational values. I computed the ridgeline as the color-averaged values in magnitude bins, each centered at the magnitude position of an (instrumental) isochrone data point and a bin width equal to half the difference to the neighboring isochrone data points. At the bright end of the color-magnitude diagram of the globular cluster the sequence is very sparsely populated. In this region the objects scattered around the sequence (which are in fact field stars not belonging to the globular cluster) would have a large systematic impact on the averaging process and thus making it very difficult to define a ridgeline. Due to this reason I decided to apply a magnitude cut at the bright end of the sequence (cut level depends on filter) and restricted this analysis to the region where the sequence is densely populated.
Table 3.10 shows the root mean square of the color difference between the ridgeline and the expected instrumental colors, for different combinations of colors and magnitudes. For all combinations I tested the differences are

Table 3.10: Color differences (RMS) for different color-magnitude combinations between the ridgeline of the measured values and the expected instrumental values.

color and waveband	$u-g$ u	$g-r$ g	$g-r$ r	$g-i$ i	$z-i$ z
difference [mag]	0.083	0.037	0.030	0.063	0.057

between 0.030 and 0.083.

In this section I showed how well we can predict the performance of our system using the calibration measurements in the laboratory. The numbers are compatible with the relative errors of our laboratory calibration at the corresponding wavelengths, which shows that there is no dominant systematic error. The performance of this kind of prediction can be improved by using a more sensitive lab calibration system (especially more sensitive at short wavelengths). Furthermore it would help to have observations with a larger amount of different airmasses at hand, in order to be able to correct for atmospheric extinction more accurately.

3.3.4 Photometric redshifts with WWFI data

In section 2.1.1, the cosmological redshift is introduced as a measure for distances on cosmic scales. To estimate an object's redshift based on photometric observations (photometric redshift, i.e. by the template fitting method explained in sect. 2.1.1), galactic model SEDs have to be convolved with the instrument's throughput curve to obtain model fluxes that can be compared to the observed fluxes. Hence it is important to characterize a system's throughput, as it has been done during this chapter, to be able to estimate photometric redshifts based on the instrument's data.

The total efficiency curve of the WWFI presented in figure 3.10 can now be used to predict instrumental magnitudes for stellar SEDs (as we did in this section), as well as galactic SEDs (as they are superimposed of stellar SEDs), with color uncertainties as given in table 3.10. The instrument is thus ready for photometric redshift estimates.

3.4 Comparison to similar systems

I want to characterize the ability to compete of our instrument in terms of pixel scale, field of view, readout speed, noise and efficiency among others. In this section I compare the parameters of the Wendelstein Wide Field Imager with the ESO OmegaCAM [Iwert et al., 2006] at the VST survey telescope and with the ESO-WFI [Baade et al., 1999] at the 2.2 m Telescope at LaSilla. Table 3.11 shows a comparison of the most important parameters of the three wide field imagers. In terms of pixel scale, all three imagers are compatible, the OmegaCAM has a larger field of view since it has four times the amount of pixels compared to ESO-WFI and to our camera. One should point out that our imager has a significantly lower readout noise when choosing the slow readout mode (and a compatible readout time), while we could choose to have a much faster readout if we live with a higher readout noise. The dark current of our camera at operating temperature is by a factor 2 lower than the dark current of the OmegaCAM.
Figure 3.21 compares of the quantum efficiency as a function of wavelength of the detector of OmegaCAM with the QE of the WWFI. In the wavelength region above 450 nm the QE of the WWFI is higher by approximately 5-10%, while at short wavelengths the QE of the WWFI seems to be lower but the QEs of the two detectors are in agreement with each other in the margins of the errors of the WWFI measurement in this region.

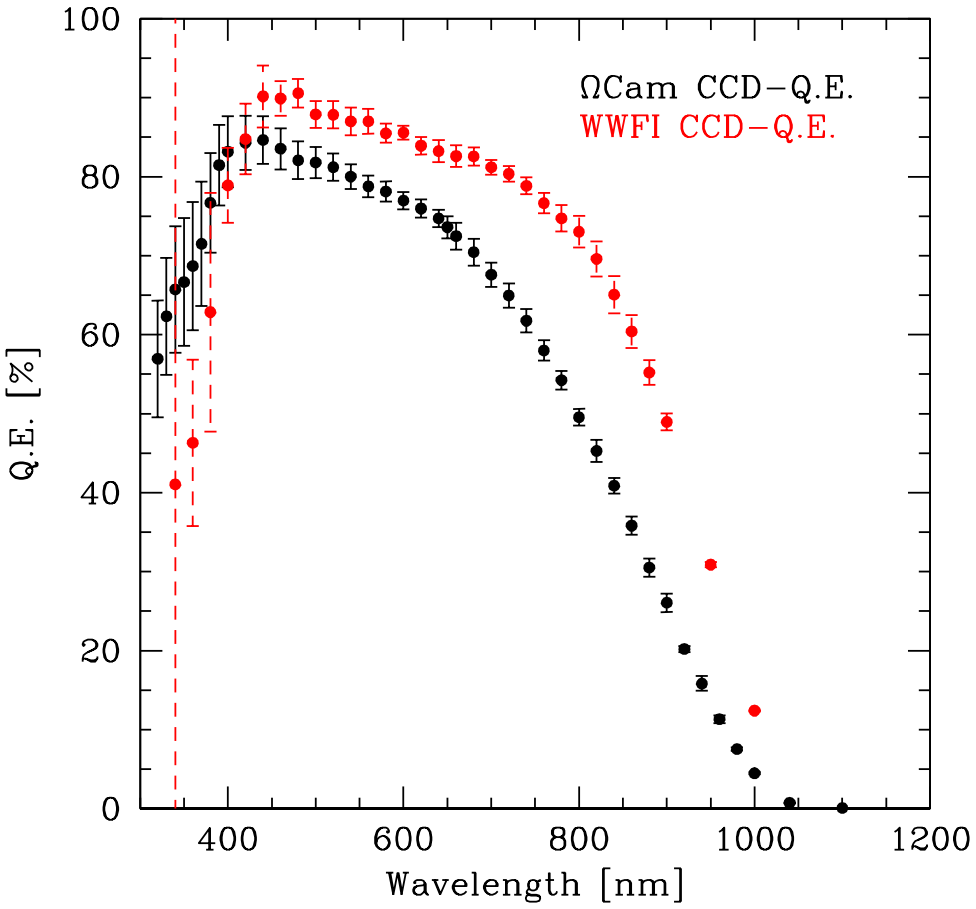

Figure 3.21: Quantum Efficiency of the OmegaCAM detector (black) compared to the WWFI (red).

Table 3.11: Comparison of WWFI with OmegaCAM and ESO-WFI. WWFI readout is via 4 ports per CCD, OmegaCam and ESO-WFI readout via 1 port per CCD.

instrument	**WWFI**	**OmegaCAM**	**ESO-WFI**
CCD type	e2v 231-84	e2v CCD44-80	e2v CCD44
pixels	8k × 8k	16k × 16k	8k × 8k
field of view	$30' \times 30'$	$56' \times 56'$	$34' \times 33'$
pixel scale	0.2"/pixel	0.21"/pixel	0.24"/pixel
telescope aperture	2.0 m	2.6 m	2.2 m
gain	5.81 or 0.69	0.54	
readout noise	$7.8e^-$ or $2.2e^-$	$5e^-$	$4.5e^-$
readout time	8.5 s or 40 s	29.5 s	
dark current	$0.27e^-$/h	$0.54e^-$/h	

Chapter 4

Environmental selection effects of Sunyaev Zel'dovich selected clusters of galaxies

In this chapter I analyze potential selection effects imprinted on Sunyaev-Zel'dovich (SZ) selected clusters of galaxies by their large scale structure environment. An environmental selection effect affects the detection probability of a cluster depending on whether it resides in an over- or underdense (3D or projected) environment. These selection effects might bias mass measurements of the affected clusters by gravitational lensing, X-ray measurements or the SZ-effect itself.

The contents of this chapter have been published in Kosyra et al. [2015]. The work in this publication has been divided among the authors as follows: Eduardo Rozo provided the *RedMaPPer* catalog. Eli Rykoff helped with the usage of the *RedMaPPer* catalog and provided the random points. The generation of the comparison sample and of the *Planck* random points has been done exclusively by myself. The method of data analysis was also implemented by myself. The theoretical prediction has been done by Annalisa Mana. The method of error estimation was implemented by myself. Ariel Sanchez provided the CMASS LRG catalog. All authors contributed with ideas, discussions and proof-reading.

4.1 Motivation

As pointed out in 2, clusters of galaxies are major astrophysical and cosmological tools that can put constraints on the dark matter content of the Universe. Sensitive to the interplay of dark matter and dark energy, they can be used as cosmological probes that could potentially enable us to distinguish between dark energy and modified gravity explanations for the accelerating expansion of the universe [for a review, see Allen et al., 2011, Borgani and Kravtsov, 2011, Weinberg et al., 2013].
There are various methods for clusters detection and mass measurement. The most important of these have been introduced in section 2.1.3. Gravitational lensing probes the dark and luminous matter distribution of a cluster by measuring the distortion of background galaxies [weak lensing, for example in Hoekstra et al., 2001, Gruen et al., 2013, 2014], or by detecting multiple images of single background galaxies close to the LoS of the cluster core [strong lensing, for example in Zitrin et al., 2012, Eichner et al., 2013, Monna et al., 2014]. The *red sequence method* [Gladders and Yee, 2005, Koester et al., 2007, Rykoff et al., 2014] detects clusters optically, based on the spatial overdensity of red galaxies. Further methods include the observation of the X-ray Bremsstrahlung emission by the hot gas in the ICM [e.g. Piffaretti et al., 2011, Vikhlinin et al., 2009, Mantz et al., 2010] and the observation of inverse Compton scattering of CMB photons by the ICM, which is known as the SZ effect [Sunyaev and Zeldovich, 1972]. The latter is observable as the distortion of the CMB spectrum along the LoS through clusters and groups.
All of these methods may suffer from selection effects induced by structures along the LoS. Mass estimates from gravitational lensing can be biased by groups along the LoS contributing to their shear signal [e.g. Spinelli et al., 2012]. The X-ray emission from structures along the LoS can add to the X-ray signal of an observed cluster, causing the mass measurement to be biased. The same is true for the SZ effect, however more severely as the SZ signal is proportional to the gas density ρ, while the X-ray flux is proportional to ρ^2, making the effect of LoS structure on SZ signals much larger at larger angular separation. Due to this reason, it is reasonable to test for a potential environment-based selection bias in SZ selected clusters, either by physically uncorrelated foreground or background structures, or by correlated structures at the same redshift as the cluster itself, which I investigate in the ongoing chapter.
One could think of several effects that potentially contribute to a selection

bias. The SZ signal of the detected cluster may be blended with groups along the LoS, resulting in a high-biased SZ signal causing clusters along overdense lines of sight to be detected more likely. On the contrary, unresolved groups in the cluster's vicinity could lead to an increased background level, resulting in a lower detection probability as the signal from the cluster is partly suppressed by the wrong background estimate. Furthermore, if the background of a cluster is contaminated with radio-loud galaxies, this could raise the noise such that clusters with a weak SZ signal are not detected.
In this chapter of the thesis I address this question by analyzing the projected group environment of SZ-selected clusters from the *Planck* PSZ1 union catalog [Planck Collaboration et al., 2013a] and test for group overdensities or underdensities along the LoS in the foreground, background and at the redshift of the clusters. I compute the cluster-group angular two-point correlation function (2pcf) of galaxy clusters and groups for different subsamples of our catalogs (correlated, foreground and background structures) to quantify correlated and physically uncorrelated group overdensities and underdensities. The group sample is taken from the *RedMaPPer* red-sequence catalog based on SDSS DR8 photometry [Rykoff et al., 2014, Rozo and Rykoff, 2014, Rozo et al., 2014]. The results are then compared to the 2pcf obtained for an independent, optically selected cluster sample, drawn as a subsample of the *RedMaPPer* SDSS DR8 catalog, and to theoretically predicted values.
This part of the thesis is structured as follows. In section 4.2, I describe the *Planck* PSZ1 union catalog and the *RedMaPPer* SDSS DR8 group catalog as well as our matching algorithm. In section 4.3, I briefly discuss two-point correlation functions. Furthermore I describe our method of generating random points for the *Planck* catalog and the procedure of defining the cluster comparison sample out of the *RedMaPPer* catalog. I also include the description of our theoretical prediction of the 2pcf. In section 4.4, I present our results, give a detailed description of our error estimation and generalized χ^2 analysis and I estimate the implications of the measured effect on SZ and lensing analyses of *Planck* clusters. I conclude in section 5.2.

4.2 Data

4.2.1 The *Planck* PSZ1 survey catalog

The *Planck* PSZ1 union catalog is a cluster catalog covering nearly the whole sky (except a small region around the galactic disk) based on SZ detections using the first 15.5 months of *Planck* survey observations. It contains a total of 1227 clusters, 861 of which are confirmed while the remaining 366 are cluster candidates [Planck Collaboration et al., 2013a]. The *Planck* satellite features a low frequency and a high frequency instrument, the former covers the bands at 30, 44 and 70 GHz [Planck Collaboration et al., 2013e] while the latter operates at frequencies of 100, 143, 217, 353, 545 and 857 GHz [Planck Collaboration et al., 2013b] with angular resolutions between 9.53' and 4.42' FWHM, for a total of nine detection bands. The channel maps of the six highest frequency bands (100 to 857 GHz) were used to build the SZ-detection catalog, in order to avoid problems caused by strong radio point sources in cluster centers, which typically have steep spectra and thus do not appear in the high frequency bands [Planck Collaboration et al., 2013a].
The generalized NFW [Navarro et al., 1997] profile from Arnaud et al. [2010] was adopted for the cluster detection.
Three detection algorithms were used to create the cluster catalog, two realizations of the *Matched Multi-filter (MMF)* method [Herranz et al., 2002, Melin et al., 2006] and [*Powell Snakes (PwS),* Carvalho et al., 2009, 2012].
The *MMF* method detects clusters by using a linear combination of maps and a spatial filtering to suppress foregrounds and noise. The two implementations (*MMF1* and *MMF3*) split the whole sky in 640 patches of size 14.66 $\times$ 14.66 square degrees covering 3.33 times the area of the sky (*MMF1*), and in 504 patches of size 10 $\times$ 10 square degrees covering 1.22 times the area of the sky (*MMF3*). The *MMF3* algorithm is run in two iterations: the second is centered on the positions of the candidates from the first one, rejecting all candidates that fall below the signal-to-noise (S/N) threshold. The matched multi-frequency filter optimally combines the six frequencies of each patch and the resulting sub-catalogs for all patches are finally merged together to a single SZ-catalog per method, selecting the candidate with the highest S/N ratio. For estimating the candidate size, the patches are filtered over the range of potential scales, selecting the scale with the highest S/N of the current candidate. Finally, the SZ-signal is estimated by running *MMF* with fixed cluster size and position.

Powell Snakes is a Bayesian multi-frequency detection algorithm, optimized to find compact objects in a diffuse background. After cluster detection, *PwS* merges all intermediate sub-catalogs. The cross-channel covariance matrix is calculated directly from the pixel data, which is done in an iterative way to minimize the contamination of the background by the SZ signal itself. In each iteration step, all detections in the same patch with higher S/N than the current target are subtracted from the data before re-estimating the covariance matrix. This so-called "native" mode of background subtraction produces S/N values 20% higher than those obtained by the *MMF* method. In order to emulate the estimation of the background noise cross-power spectrum of the *MMF* method, *PwS* is run in "compatibility" mode, skipping the re-estimation step.

Each of the three detection algorithms creates a catalog of SZ sources with an S/N ratio ≥ 4.5. Obvious false detections are removed from each of the three individual catalogs [Planck Collaboration et al., 2013a].

The union catalog contains all sources that have been detected by at least two algorithms with S/N ≥ 4.5 within a distance of $5'$, fixing the position of the *MMF3* detection or, in case of no *MMF3* detection, keeping the position of the *PwS* detection.

4.2.2 The *RedMaPPer* SDSS DR8 catalog

The Red Sequence Matched-filter Probabilistic Percolation (*RedMaPPer*) algorithm [Rykoff et al., 2014] detects clusters for their red-sequence and is based on the optimized richness estimator λ [Rykoff et al., 2012]. λ has been designed to be a low-scatter mass proxy and to estimate photo-z [Rozo and Rykoff, 2014, Rozo et al., 2014]. The algorithm is divided into two stages. The first is a calibration stage deriving the red-sequence model directly from the data by relying on spectroscopic galaxies in galaxy cluster: given an initial model of the red-sequence, cluster member galaxies are selected and used to derive a new red-sequence model, iterating this process until convergence is reached, at which point the red-sequence model is adequately calibrated. The second is the cluster-finding stage, where the red-sequence model is utilized to search for clusters around every galaxy in the SDSS. In this work, the updated version (v5.10) of the original *RedMaPPer* catalog of Rykoff et al. [2014] presented in Rozo et al. [2014] is used.

4.2.3 Matching of the *Planck* and *RedMaPPer* catalogs

In order to calculate 2pcfs correctly, identical objects in both catalogs (SZ cluster catalog and optical group catalog) should have exactly the same coordinates[1]. This requires matching of the two catalogs, which I realized by an algorithm similar to the one described in Rozo et al. [2014]. All matches in the *RedMaPPer* in a radius of $10'$ around each *Planck* cluster are found, and in the case of multiple matches the best match is defined as the *RedMaPPer* system with the highest richness. All matches with a redshift difference between the *Planck* and *RedMaPPer* redshift of more than 3σ (where σ corresponds to the redshift error given in the *RedMaPPer* catalog), are then flagged. This leaves us with a total of 290 matched clusters.

Outlier rejection

All matches that are identified as obvious SZ-projections (5 cases) by Rozo et al. [2014] are removed from the matched catalog. All clusters that have been flagged as 3σ redshift outliers are cross-matched with the Rozo et al. [2014] table of redshift outliers, and in the case of an incorrect *Planck* redshift and a correct *RedMaPPer* redshift, we accept the cluster using the *RedMaPPer* redshift and vice versa. Furthermore, all clusters with a bad z-matching have been inspected visually and rejected if identified as a clear mismatch (one case only), and all outliers in the mass-Y_{SZ}-plane (according to Rozo et al. 2014) due to a low *RedMaPPer* richness have also been removed (one case only). After rejecting all outliers, the final matched catalog includes 265 clusters.

4.3 Methods

4.3.1 Two point correlation function

The two point correlation function has already been described from a theoretical point of view in section 2.1.2. Now I would like to introduce the 2pcf as an observational tool that traces the amplitude of cluster/group clustering

[1]This is also important when defining a reference sample for comparison, see section 4.3.4

as a function of their separation. The angular correlation function $w(\theta)$ is defined as the excess probability over a random, uncorrelated distribution of finding two objects separated by an angle θ. The probability of finding two objects in two infinitesimal solid angle elements $\delta\Omega_1$ and $\delta\Omega_2$ separated by angle θ then reads:

$$\delta P = n_1 n_2 \left(1 + w(\theta)\right) \delta\Omega_1 \delta\Omega_2, \tag{4.1}$$

with n_1 and n_2 being the mean cluster/group densities in both samples. A null value of $w(\theta) = 0$ means that the two samples are uncorrelated at angular distance θ, a value of 1 means an overdensity of factor 2 with respect to the uncorrelated random distribution, while a value of -1 states there are no objects separated by angular distance θ.

A multitude of different estimators exist for calculating $w(\theta)$ from data catalogs. They can be divided in two categories: pairwise estimators, based on counting pairs, and geometric estimators. The latter are preferred in mathematical research, while astrophysical research uses the former ones more commonly.

Pairwise estimators count the number of pairs in dependence of separation in the data set D and a sample of randomly distributed data points R. The task of the random points is to account for geometrical effects like survey boundaries and masks, that would otherwise cause incorrect results. The pair count rates for the data-data P_{DD}, random-random P_{RR} and data-random P_{DR} samples are computed. The random catalog shares the geometry, but not necessarily the number of objects with the data catalog. For this reason we introduce the normalized number of pair counts $DD = \frac{P_{DD}}{N_D(N_D-1)}$, $RR = \frac{P_{RR}}{N_R(N_R-1)}$ and $DR = \frac{P_{DR}}{N_D N_R}$ with N_D and N_R being the total number of objects in the data and random catalog, respectively. Kerscher et al. [2000] compared nine of the most important estimators (pairwise and geometric) in terms of the cumulative probability of returning a value within a certain tolerance of the real correlation.

From all the estimators tested, Kerscher et al. [2000] stated that the Landy & Szalay (Landy and Szalay [1993]) estimator performs best according to their criteria. I adopt this estimator for the later analysis. It is expressed by the following equation:

$$\hat{w}_{LS}(\theta) = \frac{DD - 2DR + RR}{RR}, \tag{4.2}$$

or, in case of a cross-correlation between two different samples:

$$\hat{w}_{LS}(\theta) = \frac{D_1D_2 - D_1R_2 - D_2R_1 + R_1R_2}{R_1R_2}, \tag{4.3}$$

where DD, DR and RR stand for the data-data, data-random and random-random pair counts, respectively. The indices denote the different samples. All pair counts in eq. 4.3 are normalized to the total number of data pairs in the respective samples. However, we do not want the random points to correct for environment-based detection effects, since this is the effect we want to measure. Therefore, we are using random points where the true detections have been erased. The pair counts have been computed using the 2d-tree code *Athena* [Kilbinger et al., 2014].

4.3.2 Generation of random points for the *Planck* catalog

The LS estimator (eq. 4.3) needs a random catalog for each data catalog, in order to correct for geometrical effects that could mimic a signal.
As mentioned above, we do not want the random points to account for environmental effects, so I make no attempt to simulate and detect clusters in real ways, but I test for a potential depth dependence of the density.
Since the RedMaPPer group catalog is sufficiently deep to contain all *Planck* clusters in the SDSS footprint, we only have to generate *Planck* random points and restrict them to the same area.
There are two effects that might imprint a spatial dependence on the *Planck* detection function: the variation in the noise level and the distance from the galactic disk. In this section I describe two different approaches I tried to generate random points for the *Planck* catalog taking into account the altering noise level. The variation of the detection probability as a function of distance from the galactic disk is investigated in appendix C.
Since the noise level of the *Planck* observations varies over the SDSS region, we need to test whether the density of SZ detections has a significant correlation with the noise level that has to be accounted for when generating a random catalog. I use the *Planck SMICA* map (in HEALPIX [Górski et al., 2005] coordinates with N_{side} =2048, 50331648 pixels, resolution $\sim 1.7'$), which uses an optimal combination of the nine frequency bands [Planck Collaboration et al., 2013c] to generate a noise map averaged to 3072 pixels, to find the noise at the position of each cluster.

Fitting *Planck* luminosity function by a power law

We assume the number of *Planck* detections in a given sky cell to be a function of the noise in that sky cell that reads:

$$N(Y) = \int_{Y_{min}}^{\infty} \frac{dn}{dY} dY \tag{4.4}$$

where Y is the SZ-signal and $Y_{min} = S/N_{thresh} \times N$ is the minimum detectable signal at given noise N for a detection threshold of $S/N_{thresh} = 4.5$. $\frac{dn}{dY}$ is the *Planck* luminosity function in units of detections per signal. I modeled the luminosity function by a power law of the form:

$$\frac{dn}{dY} = AY^{\alpha} \tag{4.5}$$

with amplitude A and power α.
In order to find the best true values for A and α I used the *Planck SMICA* map to generate a noise map averaged to 3072 pixels, to find the noise at the position of each cluster, and thus the signal for each cluster. By cutting the catalog at an arbitrary maximum noise level N_{max} and at a signal level $Y_{min} > S/N_{thresh} \times N_{max}$, I generate a signal-limited subsample of the catalog. This sub-catalog is then binned in signal and redshift bins, and the power law parameters A and α are determined for each redshift bin by a maximum likelihood analysis (results shown in fig 4.1). The so found power law parameters are then used to generate weights for the *Planck* random points via eq. 4.4.
Unfortunately, I find that the *Planck* noise is not a good proxy for the detection of clusters as expected. Looking at fig 4.2, one can clearly see that the distribution of Planck clusters across the sky does not correlate with the noise. This leads us to the second approach of modeling Planck random points.

Planck detections as a power law of noise

I test for correlation of the density of *Planck* detections with the noise quantitatively. In this case I assume the number of *Planck* detections per unit area f_i to be a power law of the noise N per redshift bin i with redshift dependent exponent α_i:

$$f_i(N) = f_i(1)N^{\alpha_i}. \tag{4.6}$$

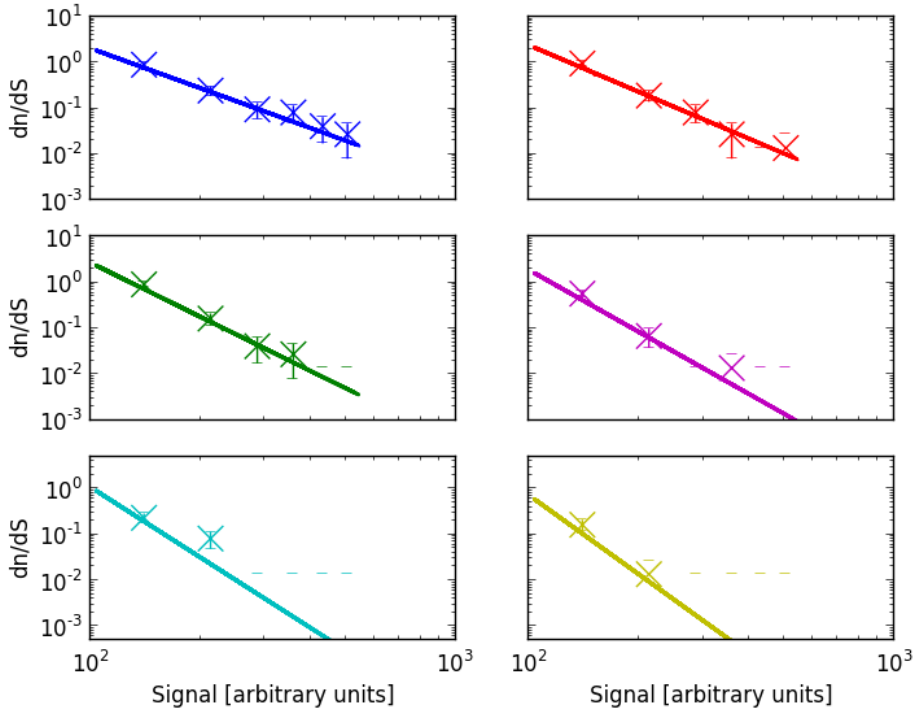

Figure 4.1: Planck power law for six redshift bins. Blue: z=0.0157...0.113, red: z=0.113...0.210, green: z=0.210...0.308, magenta: z=0.308...0.405, cyan: z=0.405...0.503, yellow: z=0.503...0.6. The crosses indicate the data points and the lines represent our global log-likelihood fit. The only exception where the data and the global fit do not agree within 1σ is in the "cyan" bin. This single outlier still agrees within 2σ, so I conclude that the global fit is a good solution. The small horizontal dashes in the empty bins represent "upper limits" and are equal to the $\frac{dn}{dS}$ of a single cluster in that bin.

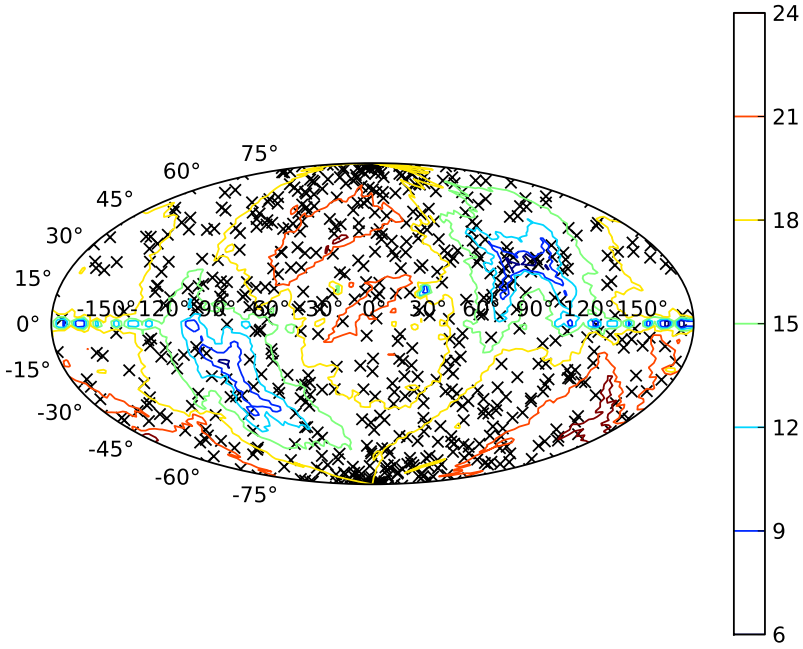

Figure 4.2: Planck noise map in galactic coordinates in Aitoff-projection. The black crosses denote the positions of *Planck* clusters. The two low-noise regions (blue contours) show the *Planck* deep survey zone. This figure shows the non-existence of a correlation between noise and detection density qualitatively.

I perform a likelihood analysis over the parameters $f_i(1)$ and α_i, by calculating the expected number of clusters in each sky cell via eq. 4.6 and computing the Poisson probability with the actual number of detections per sky cell. The power α_i scatters around and is consistent with zero for redshifts $z \leq 0.5$. Above this redshift, I find $\alpha_i \approx 0.8$. In conclusion, the noise level has no impact on detections for $z < 0.5$. We decide to remove all clusters with $z > 0.5$ from our catalog, bringing our sample size down to 250 clusters.

I further decide to use uniformly distributed random points for the *Planck* catalog. I therefore take the *Planck* survey mask to define the region where to generate the points and cut them afterwards to the SDSS footprint. The random points are generated in HEALPIX (N_{side} =2048) coordinates to ensure a uniform distribution over the sky.

4.3.3 Generation of random points for the *RedMaPPer* catalog

The random point catalog for *RedMaPPer* is generated by first drawing an arbitrary position in the sky, and then choosing a random *RedMaPPer* cluster. Given the assigned cluster redshift and richness, the *RedMaPPer* cluster model is used to randomly draw cluster galaxies to create a synthetic cluster. Then the *RedMaPPer* detection algorithm is executed at this location to determine whether the synthetic cluster is found or not. The procedure is repeated 100 times, and the fraction of times the cluster is detected at this location w is calculated. The quantity w is the weight assigned to this random point.

There is one subtlety associated with the above procedure: by random luck, some fraction of our synthetic clusters will overlap with real *RedMaPPer* clusters in both location in the sky and redshift. If one did not remove the galaxies associated with the original *RedMaPPer* cluster before placing the synthetic cluster at that location, upon running RedMaPPer one will always find a cluster there (i.e. the original cluster), and one would erroneously conclude $w = 1$ irrespective of the details of the synthetic cluster. Thus, it is critically important to remove the original *RedMaPPer* galaxy clusters from the galaxy catalog prior to drawing our random points. The clusters are removed probabilistically: for a cluster of given richness at redshift z, all of its member galaxies are collected, and each galaxy is erased according to

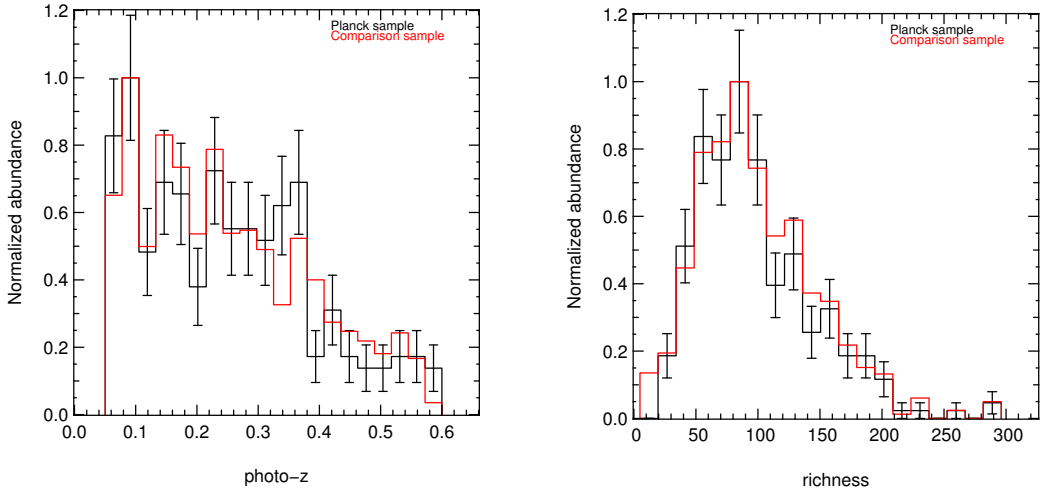

Figure 4.3: Redshift (left) and richness distribution (right) of the *Planck* sample (black) and the comparison sample (red). Planck error bars are Poissonian. Comparison sample error bars are not shown but are of comparable size.

the assigned membership probability. A galaxy that is 90% likely to be a cluster member is removed from the galaxy catalog with 90% probability.

4.3.4 Definition of a comparison sample

The goal is to test whether SZ selected clusters are generally found in a different environment than similar (in terms of redshift and richness) clusters that are selected for their optical properties. We need to compare the cluster-group two-point correlation functions obtained for groups in the vicinity of *Planck* selected clusters to an independent sample of optically selected clusters that resembles the selection function of the main sample in terms of their redshift and richness distribution. To this end, the *Planck* detection probability needs to be modeled. I assume that the probability that a *RedMaPPer* cluster is detected takes the form:

$$P_{\rm det} = \frac{1}{2}\left[1 + {\rm erf}\left(\frac{\Lambda - \Lambda_{\rm det}}{\sqrt{2}\sigma}\right)\right], \tag{4.7}$$

where erf is the error function, $\Lambda_{\rm det}$ is the richness at which the detection probability is 50% and σ the scatter in richness at fixed SZ signal. $P_{\rm det}$ states

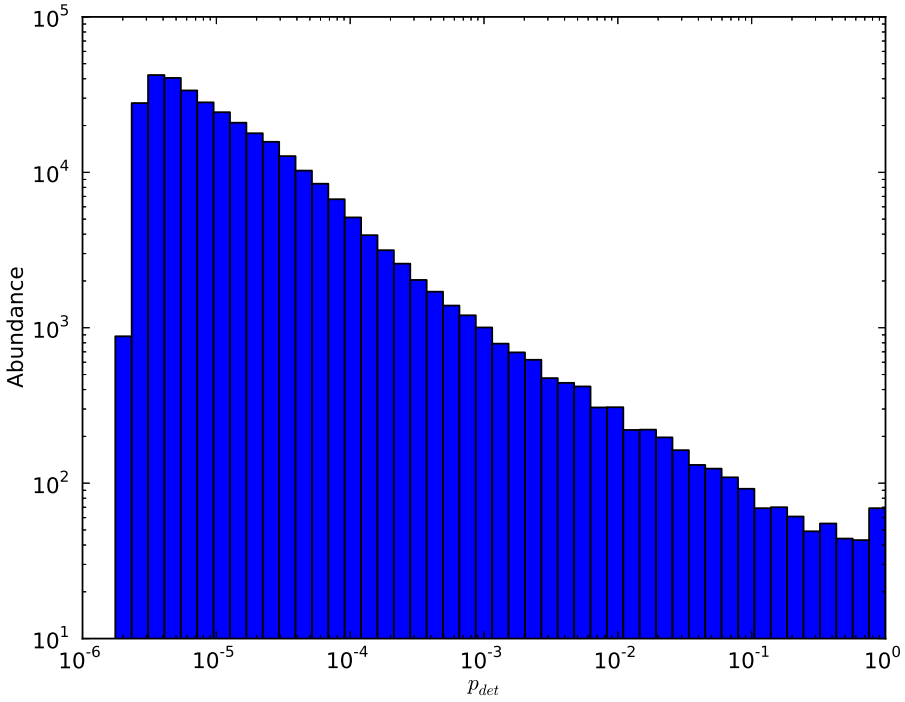

Figure 4.4: Log-log histogram of the detection probability.

the probability that a cluster of given richness Λ is detected by the *Planck* survey, if it was inside the survey area. In this work, I use the *RedMaPPer* SDSS DR8 catalog, calculate $P_{\rm det}$ for each cluster and assign it as weight. The redshift evolution of $\Lambda_{\rm det}$ and σ is parameterized as:

$$\Lambda_{\rm det} = \alpha_\Lambda (1+z)^{\beta_\Lambda} \tag{4.8}$$

and

$$\sigma = \alpha_\sigma (1+z)^{\beta_\sigma}. \tag{4.9}$$

To find the optimum values for α_Λ, β_Λ, α_σ and β_σ, I perform a likelihood analysis in these four parameters:

$$\ln(\mathrm{L}) = \sum_{i\,\mathrm{Pl}} \ln\left[\mathrm{P}_{\rm det}(i)\right] + \sum_{i\,\mathrm{non\,Pl}} \ln\left[1-\mathrm{P}_{\rm det}(i)\right]. \tag{4.10}$$

Here the sums are over all *RedMaPPer* clusters that have been detected by *Planck* or not, respectively. Figure 4.3 shows the photo-z distribution of the Planck sample (black) compared to the subsample (red) defined by the selection algorithm based on detection probability. The data agree in most bins within 1σ (of the Poissonian errors) and in all bins within 2σ. Figure 4.4 shows the distribution of the detection probability in a log-log histogram. To validate the quality of the comparison sample I drew 1000 random subsamples of 250 clusters according to their $P_{\rm det}$ and determined the likelihood of each subsample. Comparing to the likelihood of the original *Planck* sample, a p-value of 0.27 is obtained, so the comparison sample can be considered as reasonable (i.e., 27% of subsamples have lower likelihood than the actual *Planck* sample).
I generate a random catalog for the comparison sample by using the derived values for the four parameters α_Λ, β_Λ, α_σ, β_σ and calculate the detection probability for each entry in the *RedMaPPer* random catalog.

4.3.5 Theoretical two point correlation function

We calculate the cross correlation between a reference cluster at given redshift and correlated structures within a defined redshift slice around that cluster. The computation of the cluster-group two point correlation function is performed in redshift bins around the redshift of the reference cluster. As a result, the redshift distribution of the correlated groups depends on the reference cluster redshift. The total correlation function is then calculated

as the sum over all the redshift-binned contributions, weighted according to the cluster redshift distribution.
The numerical tool we use for calculating the theoretical correlation function is CAMB SOURCES [2][Lewis and Challinor, 2007], which computes the angular power spectrum C_ls of the matter density perturbations, for given input redshift distributions and for different cosmological models. We restrict our calculation to standard flat ΛCDM cosmology ($\Omega_m = 0.25$, $h = 0.7$) and the linear regime only. The relation between the cross-spectra and the projected two-point correlation function is given by

$$w(\theta) = \sum_{l \geq 0} \left(\frac{2l+1}{4\pi} \right) P_l(\cos\theta)\, C_l \ , \tag{4.11}$$

where P_l are the Legendre polynomials of degree l. We use a maximum $l = 3000$ and $\theta \in [0.01, 300]$ arcmin. The expected two-point correlation (eq. 4.11) is computed for 20 reference cluster redshifts $z_{\rm cl} \in [0.05; 0.5]$. For the redshift distribution of the reference clusters, we assume a Gaussian distribution centered at the cluster redshift $z_{\rm cl}$, with standard deviation equal to the mean photometric redshift error associated with the cluster redshift in the Planck catalog, i.e. $\mathcal{N}(z_{\rm cl}, 0.02)$. For the redshift distribution of the correlated groups, we use the observed redshift distribution of the *RedMaPPer* groups with richness $\lambda > 5$, limited to a range of ± 0.06, centered around $z_{\rm cl}$. This interval is greater than the bin width in the analysis of the observational data of ± 0.05 (see section 4.4), as the errors of the photometric redshifts (~ 0.02) have also been accounted for. The observed correlation is calculated as the average of the $w_i(\theta)$ in each redshift bin i, weighted by the average biases of the cluster and group distributions and normalized by the total number of objects.
An analogous estimate for the foreground/background structures at $|z_{\rm cl} - z_{\rm gr}| > 0.05$ yields a 2pcf consistent with zero within the statistical errors of our analysis.

4.4 Analysis and results

The relevant quantities of interest are the 2pcfs of clusters and groups for correlated structure (groups with similar redshifts as the cluster), foreground

[2] http://camb.info/sources/

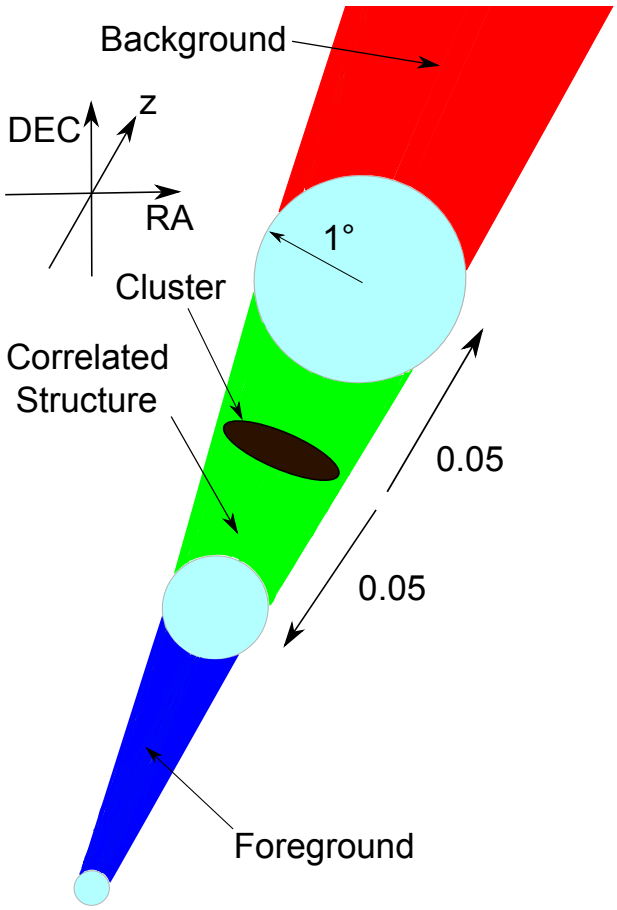

Figure 4.5: Sketch of the selection method for the group catalogs. The green, blue and red volumes show the selection for the correlated, foreground and background samples respectively. The total z-depth of the green volume is 0.1, with the cluster in the center. The angular radius for all volumes is 1° (see cyan circles).

structure (groups with lower redshift than the cluster) and background structure (groups with higher redshift than the cluster). This translates to the following set of constraints, for which I calculate the angular correlation function:

1. the RedMaPPer-*Planck* cluster pair is separated by less than $|\Delta z|$ <0.05,
2. the RedMaPPer-*Planck* cluster pair is such that $z_{\mathrm{rm}} < z_{\mathrm{pl}} - 0.05$,
3. the RedMaPPer-*Planck* cluster pair is such that $z_{\mathrm{rm}} > z_{\mathrm{pl}} + 0.05$.

The first set of pairs allows us to test for the environmental impact of physically correlated structures, the second for the impact of foreground structures and the third for the impact of background structures. This selection method is displayed graphically in figure 4.5: in green the correlated structure is shown, in blue the foreground and in red the background.
I draw 100 sets of 250 *Planck* random points, assigning them the same redshift distribution as the clusters themselves. The procedure described above is then performed on each set, averaging the results. The comparison sample is handled analogously: 100 sets of unweighted clusters are drawn by selecting randomly among all comparison sample clusters according to their detection probability. The size of these sets is on average 247, the same as the sum over all detection probabilities. This procedure is performed on the random catalog of the comparison sample (see subsection 4.3.4) too.

4.4.1 Error estimation

For estimating errors and covariance matrices, three different methods are used:

1. a "replace-one" implementation of the Jackknife resampling method for the errors of the *Planck* sample with respect to theory (zero);
2. Bootstrap resampling for the errors of the comparison sample with respect to theory (zero);
3. a "delete-one" Jackknife resampling by drawing 100 different (unweighted) representations out of the complete comparison sample randomly according to the detection probabilities for the errors of the *Planck* sample with respect to the comparison sample.

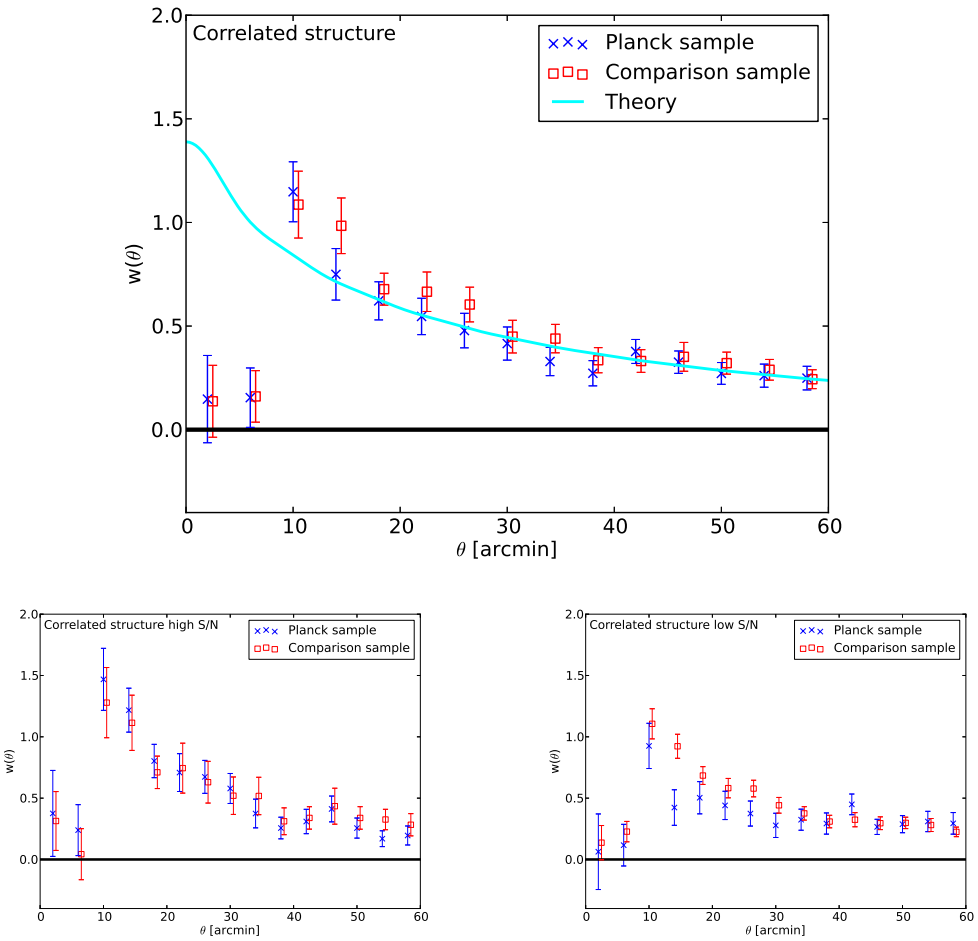

Figure 4.6: Two point correlation function for groups in the vicinity of *Planck* clusters (blue) and groups in the vicinity of clusters in the comparison sample (red). In this plot we show the 2pcf for groups with redshift equal to the cluster redshift ± 0.05 (correlated structure). The cyan line represents the theoretical prediction. Top: complete sample. Bottom left: only clusters with S/N >median. Bottom right: only clusters with S/N <median. In the low S/N case there is a slight underdensity in the *Planck* sample in the region between $10'$ and $20'$. For interpretations see sections 4.4, and 5.2.

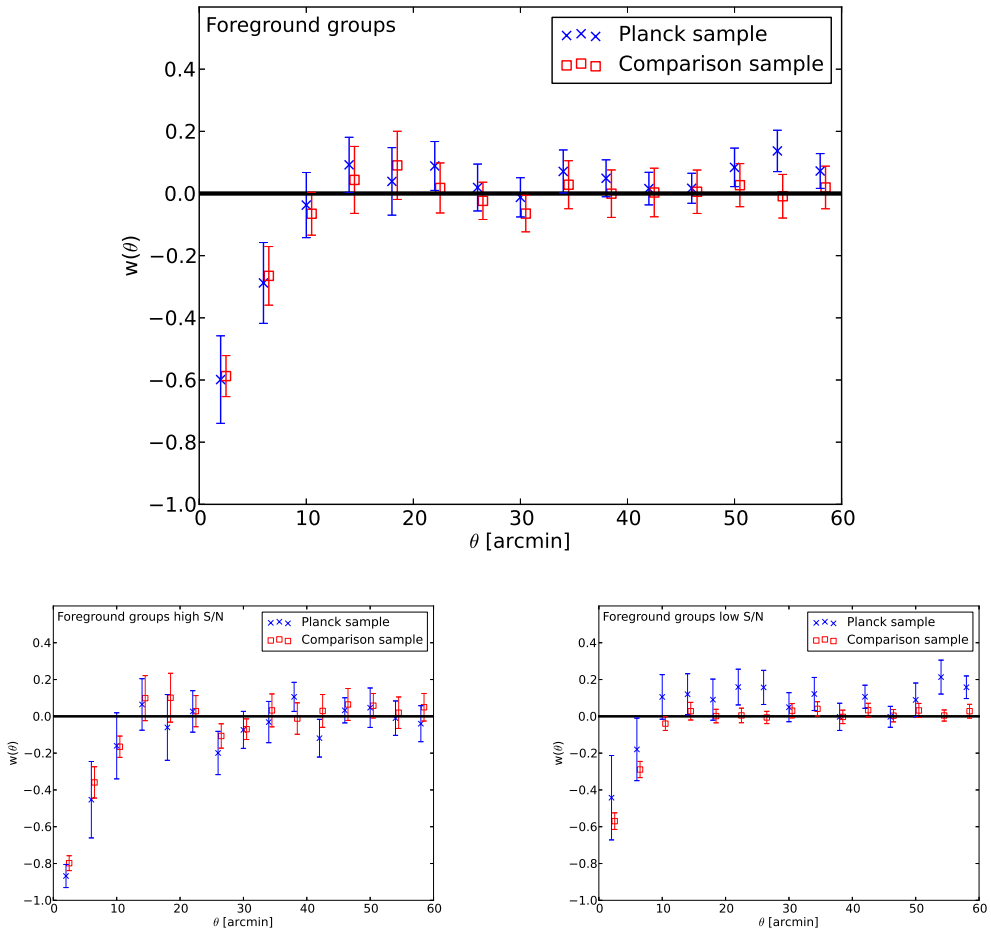

Figure 4.7: Same as figure 4.6, but for groups with redshift $z_{\mathrm{gr}} < z_{\mathrm{cl}} - 0.05$ (foreground structure). The two data sets agree well in the complete sample and the high S/N case, while for low S/N a slight overdensity can be observed in the *Planck* sample nearly over the complete angular region tested, albeit most data points still agree within the error margins.

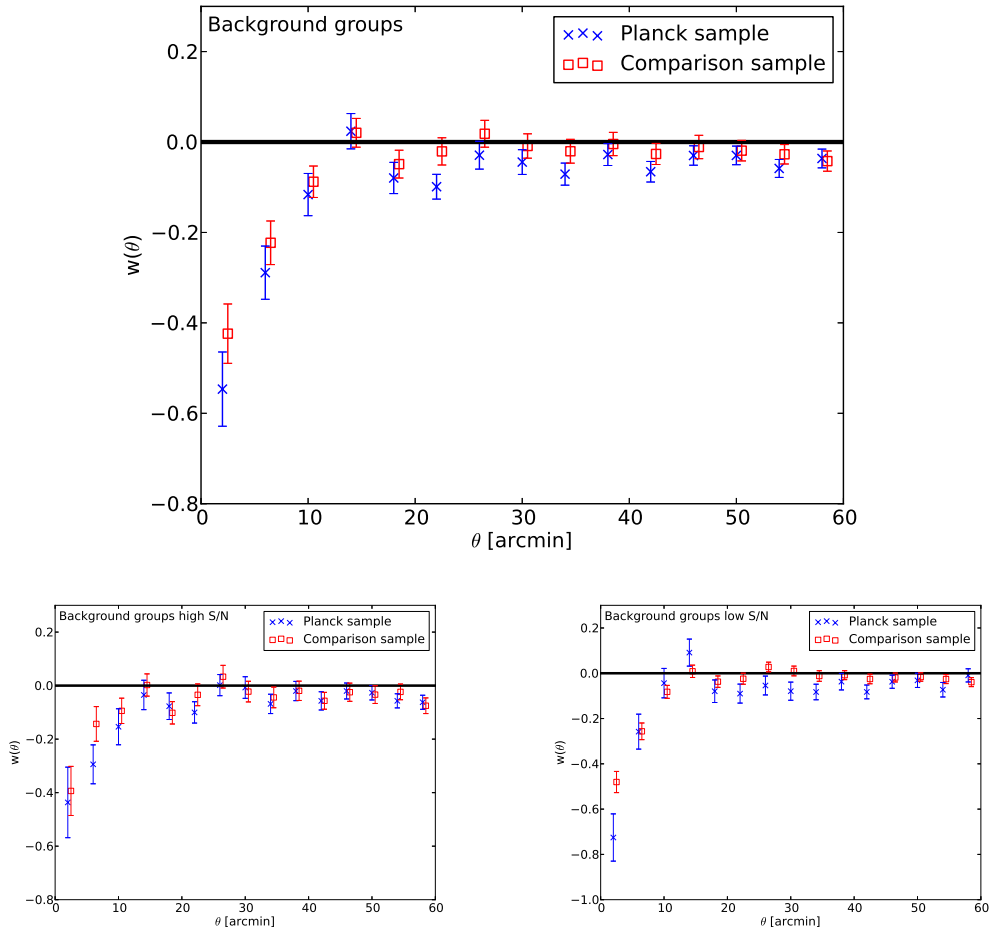

Figure 4.8: Same as figure 4.6, but for groups with redshift $z_{\rm gr} > z_{\rm cl} + 0.05$ (background structure). We observe a slight underdensity in the *Planck* sample with respect to the comparison sample, which is more severe in the low S/N subsample.

The former two will be explained in more detail in the following subsection.

Errors of the *Planck* sample with respect to theory

I use a slightly modified version of the Jackknife resampling method. In the standard "delete-one" Jackknife technique, the survey area is subdivided into a number of subsamples and the analysis is done a number of times equal to the number of subsamples, leaving out a single different subsample each time. The Jackknife covariance reads:

$$C_{ij} = \frac{m-1}{m} \sum_{k=1}^{m} \left(x_{i,k} - \bar{x_i}\right) \left(x_{j,k} - \bar{x_j}\right), \tag{4.12}$$

where m is the number of Jackknife samples, $x_{i,k}$ is the data value in bin i of sample k and $\bar{x_i}$ is the mean value in bin i. Due to the intrinsic clustering of galaxy groups, the errors in neighboring bins are assumed to be correlated: the full covariance matrix needs to be taken into account in our analysis.
The Jackknife samples are defined to be equal to the data-cylinders in the sub-catalogs. There are 250 samples, each containing exactly one cluster and all groups in its vicinity.
Since the theoretical prediction is made for the exact redshift distribution of the *Planck* catalog, it is required to find the errors with respect to this distribution. A delete-one Jackknife would introduce a systematic error here, as the redshift distribution of the sample changes when deleting one cluster. To overcome this problem, a slightly modified Jackknife variant is introduced: in each Jackknife sample, one subsample (cluster) is left out and a weight of two is assigned to another cluster. This cluster is chosen to be the closest in redshift to the left-out cluster, in order to minimize the effect of altering the redshift distribution of the sample. Equation 4.12 is thus modified to account for the changed sample size:

$$C_{ij} = \frac{1}{2} \sum_{k=1}^{m} \left(x_{i,k} - \bar{x_i}\right) \left(x_{j,k} - \bar{x_j}\right). \tag{4.13}$$

The validity of the formula has been verified in a Monte-Carlo-simulation.

Errors of the comparison sample with respect to theory

To estimate the errors of the comparison sample, I perform a Bootstrap resampling on the *RedMaPPer* catalog by drawing 1000 random catalogs

with the same number of clusters as in the original catalog. I then count the number of pairs in angular bins around each cluster, weighted with the detection probability and compute the covariance in each angular bin from these 1000 samples. It turns out that the errors estimated by this method tend to be higher than the errors of the *Planck* sample, since the modified redshift distribution due to the bootstrapping has not been accounted for. This problem can be overcome by bootstrapping sets of 5 groups instead of single groups. The sets are created by dividing the catalog into 5 subsamples split by redshift and selecting one group from each of these subsamples. The latter are sorted by weight to ensure that each package contains 5 groups with similar weights and different (equally distributed) redshifts. In this way the systematic error due to the modified redshift distribution is minimized.

4.4.2 Results

In this section I present the results of the angular two-point correlation function of galaxy clusters and groups, obtained as described earlier in this chapter. I analyze $w(\theta)$ in 15 equidistant angular bins, with a width of $4'$. The results obtained for the *Planck* sample (blue points in figures 4.6, 4.7 and 4.8) are compared with those for the comparison sample (red points) and with the theoretical predictions (cyan line). A likelihood analysis is presented in subsection 4.4.3.

High S/N detections should be influenced only minimally by a selection effect, so I expect that a potential effect will affect clusters that are just above the detection threshold S/N of 4.5 more strongly. To investigate this I split the clusters into a high and low S/N sample. The most useful approach here would be to divide the sample at S/N 7, which is the threshold above which the clusters are included in the *Planck cosmological sample*, according to Planck Collaboration et al. [2013d]. Unfortunately, in this case the size of the high S/N sample would be too small, resulting in too large the error limits, so I generate two equally large subsamples (with 125 clusters each) by splitting the sample at the median S/N of 5.4.

The top of figure 4.6 shows $w(\theta)$ for groups in a redshift slice of ± 0.05 around the cluster redshift (correlated structure). In the two innermost angular bins both samples are affected by blending effects and halo exclusion. The latter is the effect of two nearby structures merging into one halo, which has not been included in the theoretical prediction. Up to approximately $40'$, the *Planck* sample shows a slight underdensity with respect to the comparison

sample in most bins, albeit the individual data points are still in agreement within the error margins (the likelihood analysis shows that the underdensity is not significant, see table 4.1). The excess in the third bin with respect to the predicted curve is potentially explained by non-linear structure growth. In the high S/N subsample (bottom left plot) the agreement between the *Planck* and comparison sample is better, while it is worse in the low S/N case (bottom right) where *Planck* clusters are found in even more underdense background environments.
Figure 4.7 shows the 2pcf for groups with redshift $z_{\rm gr} < z_{\rm cl} - 0.05$ (foreground structure). We also observe blending here (in the innermost bins), which shows us that the detection probability of *RedMaPPer* groups also suffers from blending effects, i.e. *RedMaPPer* is less likely to detect groups in the vicinity of a rich foreground or background cluster. Besides this effect, a slight overdensity in the *Planck* sample at angular scales $>10'$ can be observed, but the errorbars suggest that this difference is not significant. The effect is again weaker in the high S/N and stronger in the low S/N subsample.
Figure 4.8 shows the 2pcf for groups with redshift $z_{\rm gr} > z_{\rm cl} + 0.05$ (background structure). Here the 2pcf suffers from blending on small angular scales, as well. The *Planck* sample shows a slight underdensity with respect to the comparison sample in nearly all angular bins. The individual data points are, however, in agreement within the error margins. The observed underdensity also appears less severe in the high S/N and more severe in the low S/N case.

4.4.3 Likelihood analysis

In order to characterize the significance by which the 2pcfs in the *Planck* sample differ from the comparison sample and from the theoretical prediction, I perform a generalized χ^2 analysis, considering the full covariance matrix to account for positively correlated errors in neighboring bins due to the clustering of groups. The generalized χ^2 reads:

$$\chi^2_{\rm gen} = \boldsymbol{\delta}^T \cdot C_{ij}^{-1} \cdot \boldsymbol{\delta}, \tag{4.14}$$

where C_{ij}^{-1} is the inverse covariance matrix and δ is the residual vector, containing the difference between measured and expected values (where measured values correspond to the *Planck* 2pcf and expected values correspond to either the comparison sample or predicted values) in angular bins. For the foreground and background sample we compare the results with zero, since

Table 4.1: P-values for the different samples for *Planck* with respect to the comparison sample and to the theoretical prediction and for the comparison sample with respect to the theoretical prediction.

Sample		All	High S/N	Low S/N	High λ	Low λ
Correlated	Plck-Comp	0.805	0.555	0.433		
	Plck-Theo	0.901				
Foreground	Plck-Comp	0.28	0.98	0.39		
	Plck-Zero	0.72	0.64	0.34		
	Comp-Zero	0.34	0.18	1.0		
Background	Plck-Comp	0.48	0.70	0.37	0.89	0.73
	Plck-Zero	0.0060	0.051	0.097	0.18	0.010
	Comp-Zero	0.16	0.023	0.64		

the theoretical predictions in these cases are several orders of magnitude lower than our measurement uncertainty.

In table 4.1 the p-values are given for all our three different data samples for *Planck* with respect to the comparison sample, *Planck* compared to theory and the comparison sample with respect to the theoretical prediction. The four innermost angular bins have not been considered in the χ^2 calculation, since the data in these bins apparently suffer from halo exclusion and blending effects, which have not been accounted for in our theoretical prediction. Thus, the number of degrees of freedom is 11.

The p-values with respect to the comparison sample are typically quite high (the lowest one being 0.28 for the foreground sample), so the null-hypothesis, which states that the two samples are similar, cannot be rejected. The generally slightly lower p-values in the low S/N case support the assumption that selection effects are predominantly observed in the low S/N regime. Nevertheless, a selection bias based on our data sample cannot be confirmed, since the values of *Planck* and comparison samples are in agreement everywhere.

When comparing the *Planck* data with the theoretical prediction, the p-values are high in the correlated and foreground samples, while we find very low values in the background, which suggests a selection effect related to lower background density. To investigate this further, we look at the p-value of the comparison sample vs zero (for the background sample) which suggests much better agreement than the value of the *Planck* sample. Analyzing the split sample with respect to S/N, it can be concluded that the p-values for the

Table 4.2: Best fit values and 1-σ intervals for the foreground and background samples, for *Planck* and comparison sample. For the background sample, *Planck* is not consistent with zero within 4σ while the comparison sample is consistent with zero within 1.3σ.

Sample		All	High S/N	Low S/N
Foregr	Plck-0	0.040 ± 0.027	-0.014 ± 0.041	0.071 ± 0.036
	Comp-0	-0.00039 ± 0.021	0.0052 ± 0.033	0.016 ± 0.027
Backgr	Plck-0	-0.049 ± 0.012	-0.047 ± 0.015	-0.046 ± 0.016
	Comp-0	-0.02 ± 0.016	-0.037 ± 0.023	-0.017 ± 0.022
		High λ	Low λ	
Backgr	Plck-0	-0.044 ± 0.016	-0.058 ± 0.016	

Planck sample are higher than for the complete sample in both cases (low and high S/N), even though for low S/N the disagreement seems to be larger when looking at the plot. The reason for this are the larger uncertainties in the split sample due to the smaller sample size. The p-values for *Planck* relative to the comparison sample in the high S/N case are in good agreement, yet both only marginally agree with zero, which most probably originates from cosmic variance. In the low S/N sample however, the agreement of *Planck* with zero is significantly worse than for the comparison sample. I conclude that the background underdensity for *Planck* clusters is a function of S/N and the effect becomes stronger for low S/N detections.

I also split the group sample in two parts at richness 12 (high λ and low λ in table 4.1), but no significant differences were found in these two subsamples.

The measured 2pcfs appear to be nearly independent of angular distance in the observed range, thus it seems convenient to fit a constant value. The best fitting constants and corresponding 1σ errors for the 2pcf are given in table 4.2. The first four angular bins which suffer from blending have been ignored in this fit. We see that the background correlation is not consistent with zero for *Planck* with a significance greater than 4σ, while the comparison sample is consistent with zero within 1.25σ, which can still be due to statistical fluctuations. Since the detected background underdensity is -0.049 with a significance of $\sim 4\sigma$ with respect to zero but the comparison sample also differs from zero with a value of -0.02 at $\sim 1.25\sigma$, I conclude that statistical fluctuations in the particular regions used (cosmic variance), likely also contribute to the observed defect of *Planck* background groups, but are

no sufficient explanation of the full observed effect. On the other hand, one could imagine that *RedMaPPer* detections are biased in the vicinity of massive clusters due to the correlated structure that surrounds them out to large radii, which might affect the detection of groups due to the blending effect, as discussed in section 4.4.2.
When looking at the foreground sample, the slight overdensity one might expect from figure 4.7 is not significant, with a p-value of 0.72.

4.4.4 2pcf for *Planck* and LRGs

I want to verify the results by comparing them to an independent sample of background sources. The *RedMaPPer* group catalog is replaced by the *CMASS* catalog of luminous red galaxies (LRG) with spectroscopic redshifts [Eisenstein et al., 2011, Dawson et al., 2013, Anderson et al., 2014]. As clusters and groups tend to feature mostly red galaxies, the LRGs are expected to show a similar clustering behavior. Furthermore, if the origin of the observed underdensity is truly the presence of radio sources, which tend to cluster at high redshifts, the same effect is expected to be present in *CMASS* galaxies. When looking at figure 4.9, the underdensity found for background *RedMaPPer* groups cannot be confirmed with CMASS LRGs. If the physical effect has a z-dependence, the fact that the redshift distributions of the *RedMaPPer* groups and the *CMASS LRGs* differ largely might be responsible for the observed effect. As uniformly distributed random points are being used for the *Planck* clusters, a potential position dependence of the selection function is not accounted for. In particular, a spatial variation of the redshift dependence of the *Planck* detection probability could possibly mimic such a selection effect. I investigated the most likely version of this possibility in Appendix A, although more complex dependencies might exist.

4.4.5 Discussion of possible selection effects

I briefly discuss several possible causes for a selection bias. Groups in the vicinity of the observed cluster that are not close enough to the cluster to contribute to the signal, might still be inside the filter window for background estimation and artificially rise the measured background level and lead to a decreased detection probability in crowded fields, as the subtracted background estimate is too large. On the other hand, clusters are detected by combining six frequency bands with different filter sizes, so it is rather

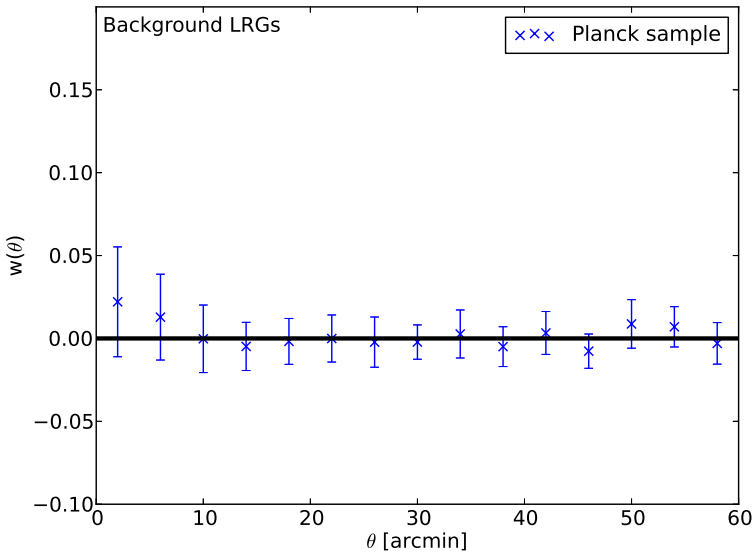

Figure 4.9: Same as figure 4.8, but for CMASS LRGs with redshift $z_{\rm LRG} > z_{\rm cl}+0.05$ (background structure). We do not observe the underdensity that we observed for the RedMaPPer group background in figure 4.6. The small errorbars come from the much larger number of objects due to the non-overlapping redshift distributions of *Planck* and CMASS (all LRGs are background to all clusters with respect to redshift alone).

unlikely that this still causes problems when detecting clusters based on the differential signal.
Another possibility would be a selection effect that originates from radio-loud galaxies in the background. According to Donoso et al. [2010], in the redshift range $0.4 < z < 0.8$ radio-loud active galactic nuclei (RLAGNs) are predominantly found in denser environments than radio quiet galaxies and regular red luminous galaxies (LRGs). They conclude that this clustering effect is stronger for more massive RLAGNs. Yates et al. [1989] compare the clustering effect of RLAGNs at $z \approx 0.2$ to the one at $z \approx 0.5$ and find that the RLAGNs at the latter redshift reside in environments denser by a factor of three, on average. They also state that more luminous RLAGNs are found in denser environments than fainter ones. Based on their findings I hypothesize that clusters in regions with high background group densities are less likely to be found in SZ surveys, as the increased probability of finding radio sources in the background may lead to an increased noise along the LoS that raises the detection threshold.

4.4.6 Implications for SZ and lensing masses

I found a potential selection effect that causes *Planck* clusters to be found preferentially in regions with low background density in a projected environment of angular range from $\sim 15'$ up to $\sim 60'$. It is possible to model the effect as a constant underdensity in this range, which I found to be -0.049 ± 0.012.
Now I will investigate whether this effect influences mass estimates by various methods. At first, I estimate the defect SZ signal caused by this effect in the average beam size of the *Planck* channels that are involved in the cluster detection. I use the median redshift of the 250 *Planck* clusters in our sample (0.23) and calculate the mean SZ signal of all *RedMaPPer* groups with redshift higher than that value +0.05 (as our background selection), using the scaling relation from Planck Collaboration et al. [2013d]. Analogously, the mean SZ signal of the *Planck* clusters themselves is computed. With the number of background groups with respect to the previously mentioned *Planck* median redshift inside the average beam size of the involved channels and the average background underdensity we can calculate the Y_{SZ}-defect caused by a background underdensity of -0.049. The result is a signal of only 1.7×10^{-4} relative to the mean signal of the cluster. This subdominance of background groups in SZ is due to the self-similar slope of the Y_{SZ}-MOR. I

conclude that there will be no implications on cluster masses derived from their SZ-signal. For the same reason I conclude the effect of the background underdensity on X-ray measurements to be negligible as well.
Furthermore, I estimate the impact that our potential selection effect has on weak lensing mass estimates of the affected clusters. To this end I calculate the effect of the measured background underdensity on the convergence κ, which is the quantity that determines the magnification in gravitational lensing. As an example, I use a cluster with a mass of $M = 3 \times 10^{14} M_{\odot}$, at the *Planck* median redshift 0.23 and sources at redshift of 1.0, assuming that 5%[3] of the matter between the cluster redshift and the source redshift is missing. In a radius of 15' around such a cluster, the relative κ deficit would then be $\sim 80\%$ of the mean κ of the cluster (see section 5.2 for a discussion on the implications on mass-observable relations.). Due to the mass-sheet degeneracy [Schneider and Seitz, 1995, Seitz and Schneider, 1995, 1997], this large κ defect might have a much smaller effect on shear measurements. It will, however, have a non-negligible effect on magnification measurements. Magnification increases the surface area of observed objects with constant surface brightness, leading to higher total brightness (lower magnitude). On the one hand, the consequence is a higher (observed) galaxy density, as faint background galaxies (just below the detection limit) might be detected as their brightness increases. On the other hand, the increased surface area also increases the separation between the magnified objects, leading to a lower (observed) galaxy density, counteracting the first effect. For steep luminosity functions the first effect is stronger (which is generally the case for blue galaxies), while for flat luminosity functions the second effect dominates (red galaxies). As a consequence, I expect a negative 2pcf of red background galaxies around clusters caused by this effect. A potential background underdensity would counteract this effect, causing a slightly less negative 2pcf at small angular scales and a slightly positive 2pcf at intermediate angular scales. I estimate the amplitude of this effect for a typical *Planck* cluster using equation 10 from Umetsu et al. [2011]. I get a result in the order of $w(\theta) \lesssim 10^{-2}$ for $\theta = 10'$ for the effect caused by the magnification of the cluster itself, while the counteracting effect caused by the underdensity is 80% of this number, both of which is too small to be detected in our measurement.

[3] I assume here that *RedMaPPer* groups have no selection bias on average.

Chapter 5

Summary & Conclusions

In this chapter I will summarize the results of the two projects presented in this thesis and give some suggestions about research that might be performed in the future to complement the work presented here.

5.1 WWFI

I have presented the details about the mechanical construction of the Wendelstein Wide Field Imager as well as about the electromagnetic shielding and the software. Furthermore I have shown the details and results of calibration measurements in our laboratory as well as with first on-sky data.
In Sect. 3.2.1 I used the analytical method introduced in Gössl et al. [2012] that successfully allows us to consider data points at high count rates in our photon-transfer analysis even when the photon noise of the masterflat begins to dominate. I found reasonable results for the gain compared to the manufacturer's estimation (Table 3.3). The quantum efficiency measurement in the laboratory shows only small variations between the four CCDs and absolute values that are slightly higher than the manufacturer's minimum guaranteed values (at least at long wavelengths, while at short wavelengths our measurement errors are large). I consider these values to be in good agreement with specifications.
Charge persistence in our detector is found to be well described by a Debye-Edwards law. It varies with temperature and with illumination level, but is independent of the wavelength of the incident light. I am able to predict the amount of residual charge that remains on the detector in dependence

of time for the "worst case" of oversaturation, which may be important for future observations.
I have shown that the charge transfer efficiency (CTE) behaves as one would expect from low values at low light levels to higher values at intermediate illumination (it can be described by a power-law in this region quite well), becoming slightly lower above half of full-well capacity. I show that these results compare well to the values determined by the manufacturer, with few exceptions for very few ports only (see also App. A).

I have determined the photometric zero point of our system by two different methods (an observation of a globular cluster with published photometry and a standard star field) and found the results to be in good agreement with each other (with exception of the z filter where only one result is available). The dominant error source in this analysis is the atmospheric extinction which has been measured for the standard star analysis but has been estimated for the globular cluster analysis. The results are also generally in good agreement with theoretically calculated values, with the exception of the i and z filters where the dominant error source is assumed to be systematic errors in our lab measurements.
In App. B I describe the method I used to predict theoretical zero points with an exposure time calculator[1].

The on-sky performance of our system has been predicted by interpolating stellar spectra to isochrone entries and convolving the spectra with our measured efficiency curves. Comparing these theoretical magnitudes with observations of a globular cluster, I find the accuracy of the prediction to be in the range between 0.030 and 0.083 mag in all colors. To improve these numbers, a better lab equipment would be necessary, especially a brighter calibration lamp.

Finally in Sect. 3.4 I found that our system is very well comparable to similar systems, ESO OmegaCAM [Iwert et al., 2006] and ESO-WFI [Baade et al., 1999] in most respects. The field of view of the WWFI is smaller than the FoV of OmegaCAM, but in terms of QE and dark current our system is even better.

[1]The exposure time calculator uses theoretical values only

5.2 Selection effects of SZ clusters

The main scientific goal was to investigate possible selection effects on SZ selected clusters based on their group environment and estimate implications of such an effect on SZ, X-ray and lensing mass estimates.
I summarize the results as follows:

1. I do not find an overall selection effect due to correlated or foreground structure.

2. I find a potential underdensity of galaxy groups in the background of *Planck* clusters which manifests itself in an average 2pcf in an angular range $<40'$ of -0.049 with a significance of $\sim 4\sigma$. However, the effect is not detected when replacing *RedMaPPer* groups with CMASS LRGs in the analysis.

3. This effect grows stronger for low S/N detections and vanishes for high S/N detections. I find no dependence of the effect on the richness of the groups.

4. I consider three possible explanations for this effect:

   - An erroneous background estimation in overdense environments might lead to a lower detection probability of low signal clusters in these regions. The details and relative importance of these effects is likely dependent on the instrumental and survey design and the object detection algorithm. On the other hand, the fact that *Planck* detections combine six bands makes this explanation rather unlikely.
   - RLAGNs, which tend to cluster at high redshifts [Donoso et al., 2010, Yates et al., 1989], contribute to the radio signal in regions where the background density is high and could suppress low S/N detections.

     The above two points could be verified by using a mock catalog of galaxy groups and associated radio sources to determine the effect on cluster detection in a simulated survey
   - The *Planck* selection function is responsible for this effect.

     A spatial variation of the *Planck* selection function that correlates with the spatial variation of the *RedMaPPer* selection function

could mimic the observed background group underdensity. Due to lack of access to the *Planck* selection function I am not able to test this at the moment. On the other hand, I do get the same results if I split the sample by distance to the galactic disk, as shown in Appendix C, which makes this explanation less probable.

5. This potential selection effect has a vanishing impact on SZ and X-ray mass estimates. The implications on lensing mass estimates are, however, much larger with an estimated κ deficit of order unity relative to the cluster signal.

   Regarding the effect of our findings on other SZ-surveys, I expect the effect of environmental selection to be more severe for fewer frequency bands and lower angular resolution. As the SPT and ACT surveys both have fewer frequency bands but higher angular resolution compared to *Planck*, it is unclear whether similar effects could be present in these surveys as well.

In the latter context, it is interesting to note that Gruen et al. [2014] found a discrepancy from the self-similar slope ($\beta = 5/3$) in the Y_{SZ}-mass scaling relation for low S/N *Planck* clusters, with a slope of 0.76 ± 0.20. Sereno et al. [2014] found a slope of the Y_{SZ}-mass scaling relation of 1.22 ± 0.24 using all *Planck* clusters detected by the *MMF3* algorithm, and a slope of 1.40 ± 0.31 when using only the cosmological subsample (S/N >7). They made an additional analysis forcing the intrinsic scatter to zero, obtaining even lower results for the slopes, 0.95 ± 0.10 for the full and 1.09 ± 0.17 for the cosmological samples. The background underdensity in *Planck* clusters that I find in this work potentially explains their findings, since that could cause a low-biased lensing mass, depending on the S/N ratio of the SZ signal, resulting in a shallower slope of the scaling relation. The fact that Sereno et al. [2014] find a slightly steeper slope in the cosmological sample, supports the assumption of the S/N dependence of this effect. Von der Linden et al. [2014], who compared cluster masses from the *Planck* catalog with weak lensing masses from the *Weighing the Giants* project, found evidence for a mass dependence in the calibration ratio between the *Planck* mass M_{Planck} and the weak lensing mass $M_{\rm wl}$ which takes the form $M_{Planck} \propto M_{\rm wl}^{0.68^{+0.15}_{-0.11}}$. A possible explanation for their findings might be low-biased weak-lensing masses for low-mass clusters, caused by a background underdensity that dominates at low S/N, as I hypothesize it in this work.

5.3 Outlook

During the first year of observations after commissioning, the WWFI gathered a large amount of data with good seeing ($< 1''$) on several northern galaxy clusters, including *Planck* clusters. The aim is a combined weak lensing analysis of all available SZ selected clusters, as it has been done for 12 clusters from the *Planck* and SPT surveys in Gruen et al. [2014]. In this way one would be able to compare lensing masses of SZ selected clusters to masses of clusters measured by other methods. A larger sample will allow to determine the Y_{SZ}-mass scaling relation for SZ selected clusters at different S/N-levels detected by different SZ-surveys, and figure out whether the slopes of the mass-observable relations are in agreement with the self-similar case.
Further observations that are planned with the WWFI include:

- Observations of the nearby galaxies M31 and M33 with the goal to find and confirm variable sources, especially microlensing events by compact halo objects [Riffeser et al., 2011] and Delta-Cepheii stars [Kodric et al., 2013], with the goal to determine the distance to these galaxies more precisely as a groundwork for cosmological distance measurements.

- Photometric observations of cD-galaxies in clusters at low redshifts, which can give further insight into the nature of the dynamics of central galaxies of clusters, when analyzed in conjunction with velocity profiles obtained from spectroscopic observations, as it has been done in Bender et al. [2014]. Improving the quality of the photometry of the low-surface-brightness haloes might allow to clarify details about the evolutionary history of these dominant cluster galaxies.

- Follow-up of Pan-Planets transit candidates. Pan-Planets is a survey searching for transiting extra-solar planets in the galactic disk, conducted by the Pan-STARRS1 camera [Koppenhofer and Henning, 2011]. The main goal here to constrain the transit periods and transit depths more precisely to get further insight into the parameters of the host star and the exoplanet.

In the near future, cluster observations with the Wendelstein Wide Field Imager will contribute to the calibration of cluster probes and, in this way, to our undersanding of the cosmos.

Appendix A

Detailed charge transfer efficiency

In Sect. 3.2.9 I presented the results of the CTI measurement in our laboratory, but I only showed results for one CCD (number 0). In this appendix I show the complete set of measurements for all CCDs and compare them to the manufacturer's results. Figure A.1 shows the parallel CTI for all four CCDs compared to the values measured by Spectral Instruments. (USM: red crosses, green, blue and magenta; SI: cyan, yellow, black and red triangles). The plots show overall good agreement between the two measurements with few outliers in CCD1 and CCD2 (top right and bottom left) at low signal levels, where the measurement performed by SI yields higher values than our own results. Figure A.2 shows the same for serial CTI. Here, a few more outliers can be identified, also at low signal levels, but this time SI measures lower values than ourselves. The accuracy of the data obtained at USM is supported by successful fitting of a power law. Moreover, port-to-port variations of the data are very small.
It should be pointed out that port 2 of CCDs 0 and 2 (green data points in top left and top right of A.2) show a lower CTI by approximately factor 3 at low signal levels compared to the value estimated by SI. To explain these outliers, a more detailed analysis is required.

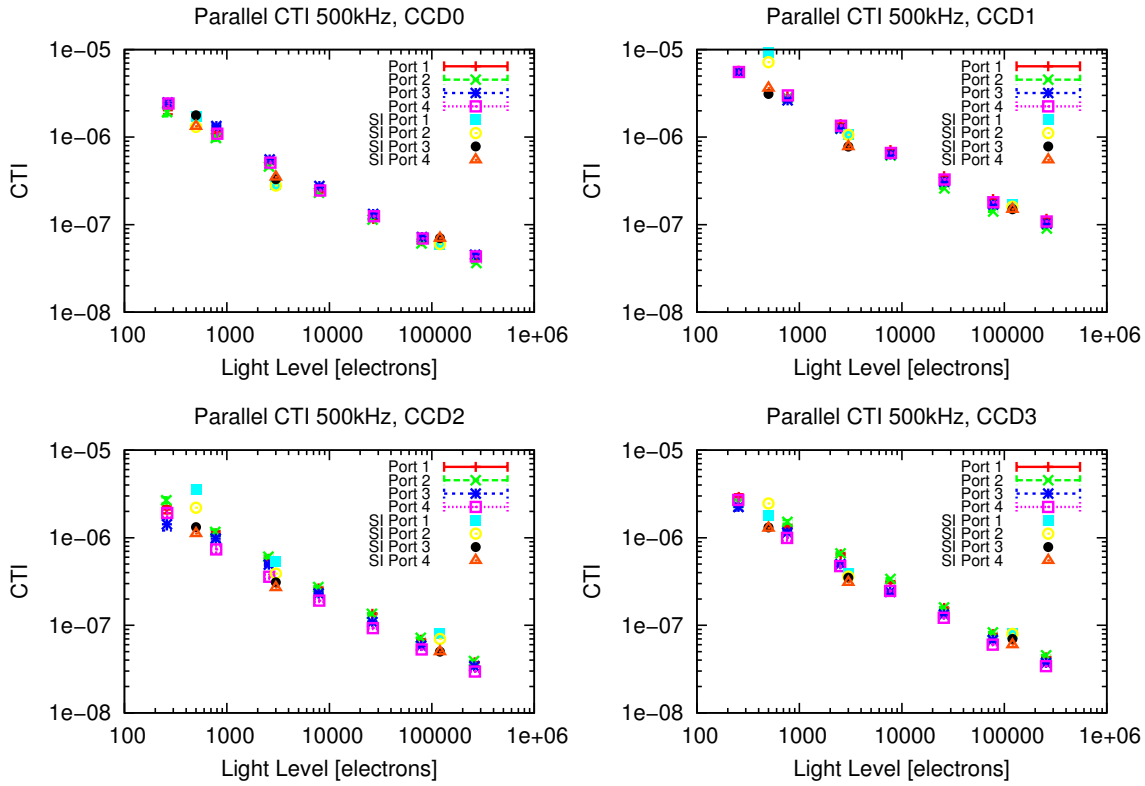

Figure A.1: Parallel CTI for all four CCDs in the 500 kHz readout mode in dependence of illumination, compared to the values given by the manufacturer (SI).

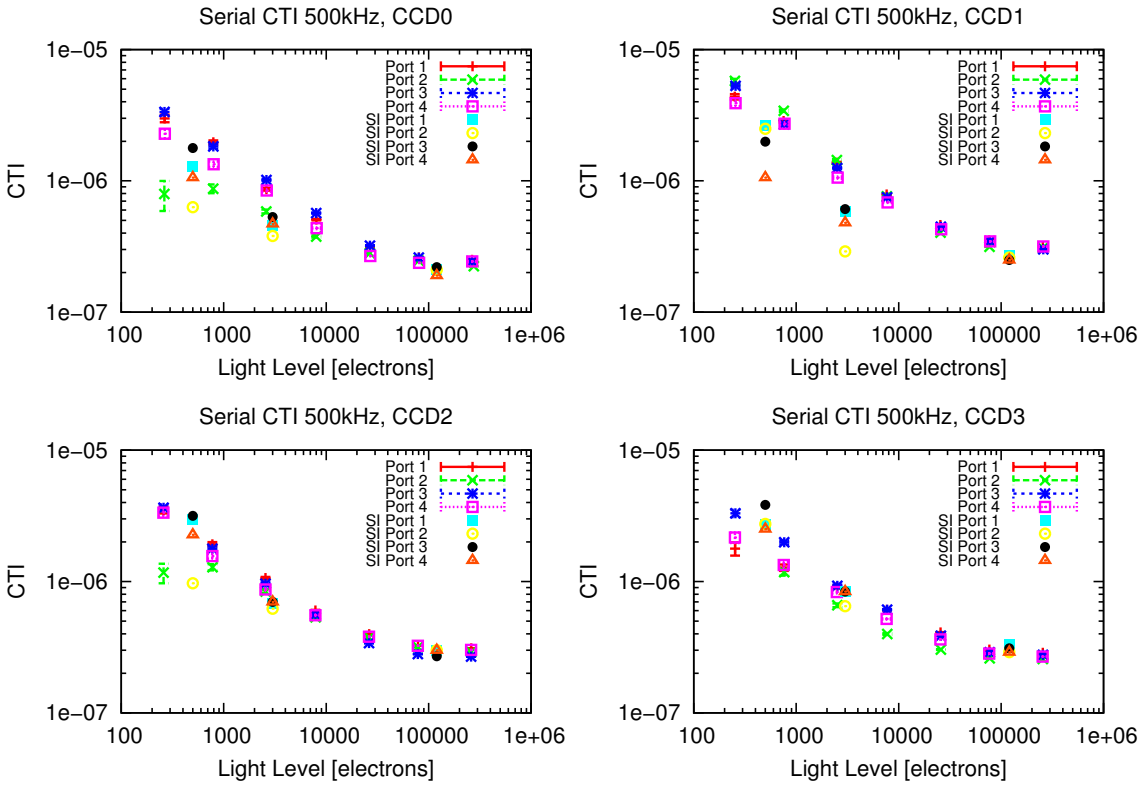

Figure A.2: Serial CTI for all four CCDs in the 500 kHz readout mode in dependence of illumination, compared to the values given by the manufacturer (SI).

Appendix B

Predicting the zero point with an exposure time calculator

The intended purpose of an exposure time calculator is (as the name implies) calculating the needed exposure time on an object of a given magnitude in a given filter to achieve the desired signal to noise ratio. A list of input parameters of our exposure time calculator is shown in table B.1. The exposure time calculator can be "reversed" and used to calculate the instrument's zero point (as we did in sect. 3.3.2) by setting the exposure time to 1 s and varying the input magnitude to find an output signal of 1 e^- inside the aperture. The input magnitude is then equal to the zero point of the instrument in the selected filter.

Aperture diameter refers to the aperture on the detector (in arcsec) inside which the signal is accumulated. *# of exposures* is the amount of exposures that the total *Exposure time* is split into. *Throughput Q* is the integral over the total efficiency of the corresponding filter, considering detector QE, filter transmissivity, mirror reflectivity and lens transmissivity, as shown in Fig. 3.10, while λ_{central} is the central wavelength and λ_{width} is the spectral width of the filter. *Mirrorarea* denotes the effective collecting area, corrected for obscuration by the secondary and tertiary mirror and other components. *RN per pix and exp* is the readout noise per pixel per single exposure, while *RN per pix* is the derived accumulated read noise for the total stack (if *# of exposures*=1, then *RN per pix*=*RN per pix and exp*). # e^- per pix/apert (sky/obj) are the number electrons generated per pixel/in the aperture from the sky background/object respectively.

Table B.1: Input and output parameters of the exposure time calculator for the WWFI.

Variable inputs	**Constant inputs**	**Derived values**	**Output values**
AB-magnitude	Night sky AB	Night sky at AM	# e^- per pix (sky)
Exposure time	Extinction	RN per pixel	# e^- apert (sky)
Seeing at zenith	Throughput Q	Seeing at AM	# e^- per pix (obj)
Aperture diameter	λ_{central}		# e^- apert (obj)
Airmass (AM)	λ_{width}		# ADU apert (obj)
# of exposures	Mirror area		$\frac{\#e^-\text{apert (obj)}}{\#e^-\text{total (obj)}}$
	Pixel size		S/N apert
	RN per pix & exp		

Appendix C

Split sample with respect to galactic distance

As mentioned in section 4.4.4, I found a discrepancy in the results as an underdensity is observed in the background of *Planck* selections for RedMaPPer groups but not for CMASS LRGs. In order to investigate the reason of this difference I split the sample at the median absolute galactic latitude to find out whether the *Planck* selection function depends on the distance to the galactic disk, as it could be caused for example by galactic foreground emission. Our uniformly distributed set of *Planck* random points would not account for such an effect.
The results of the absolute latitude split are shown in figure C.1, the corresponding p-values are found in table C.1 and the best fitting values and 1-σ intervals in table D.1. The split results in a nearly unchanged result for 2pcf at angular distances up to $\sim 30'$. Above that value however, the underdensity vanishes in the low latitude sample while it persists in the high latitude sample.

Table C.1: Same as table 4.1, this time for the split samples with respect to distance to the galactic disk and redshift.

Sample	High abs(lat)	Low abs(lat)	High z	Low z
Plck-Zero	0.012	0.25	0.52	0.018
Comp-Zero	0.17	0.32	0.86	0.0057

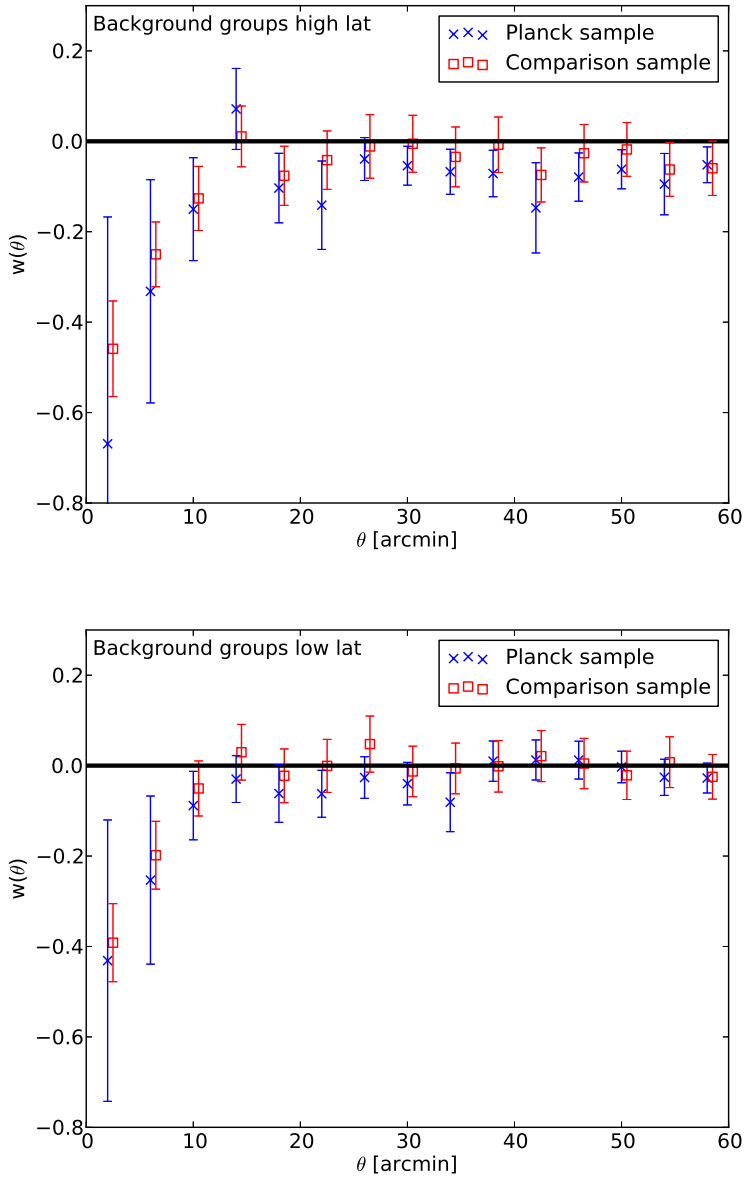

Figure C.1: 2pcf for background groups far from the galactic disk (top) and close to the disk (bottom). The sample has been split at the median absolute galactic latitude.

Appendix D

Split sample with respect to group redshift

As the redshift distributions of RedMaPPer and CMASS are largely different, I investigated the possibility of a redshift dependence of this effect by splitting the RedMaPPer group sample at z=0.45. This value has been chosen to ensure the sample sizes to be approximately equal for the high z and low z sample **after** selecting the background groups.
The results of the redshift split are shown in figure D.1, while the p-values are shown in table C.1 and the best fitting values and 1-σ intervals in table D.1. The split reveals a slightly more distinct underdensity of the *Planck* sample with respect to zero for low redshift background groups, as it might be expected from the null results with the (high redshift) CMASS sample. On the other hand, a similar degree of difference between high z and low z background can be observed in the Comparison sample, making the relative difference non-significant.

Table D.1: Same as table 4.2, but for the split samples with respect to distance to the galactic disk and redshift.

Sample	High abs(lat)	Low abs(lat)	High z	Low z
Plck-zero	-0.029 ± 0.023	-0.023 ± 0.016	-0.037 ± 0.017	-0.059 ± 0.017
Comp-zero	-0.039 ± 0.017	-0.0023 ± 0.015	-0.0079 ± 0.0075	-0.032 ± 0.0099

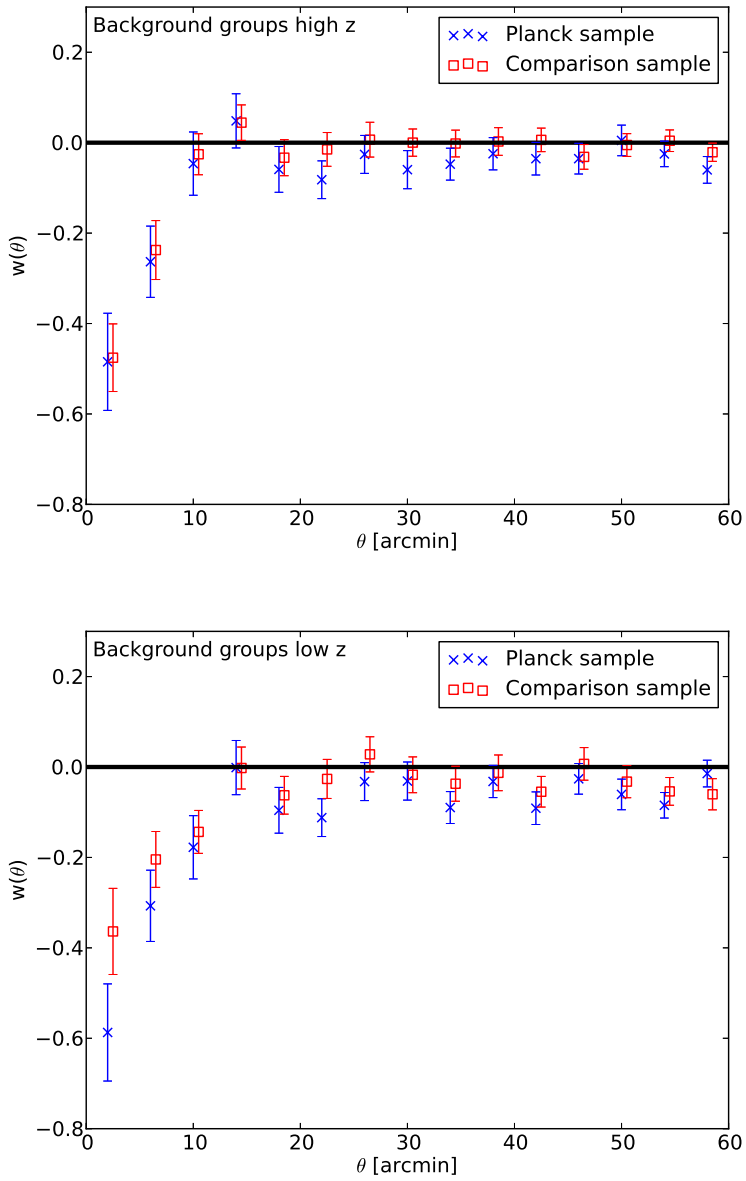

Figure D.1: 2pcf for background groups with redshift >0.45 (top) and with redshift $\leq$ 0.45 (bottom).

Bibliography

T. Abel, P. Anninos, M. L. Norman, and Y. Zhang. First Structure Formation. I. Primordial Star-forming Regions in Hierarchical Models. *ApJ*, 508: 518–529, December 1998. doi: 10.1086/306410.

C. Alcock, R. A. Allsman, D. R. Alves, T. S. Axelrod, A. C. Becker, D. P. Bennett, K. H. Cook, N. Dalal, A. J. Drake, K. C. Freeman, et al. The MACHO Project: Microlensing Results from 5.7 Years of Large Magellanic Cloud Observations. *ApJ*, 542:281–307, October 2000. doi: 10.1086/309512.

S. W. Allen, A. E. Evrard, and A. B. Mantz. Cosmological Parameters from Observations of Galaxy Clusters. *ARA&A*, 49:409–470, September 2011. doi: 10.1146/annurev-astro-081710-102514.

D. An, J. A. Johnson, J. L. Clem, B. Yanny, C. M. Rockosi, H. L. Morrison, P. Harding, J. E. Gunn, C. Allende Prieto, T. C. Beers, et al. Galactic Globular and Open Clusters in the Sloan Digital Sky Survey. I. Crowded-Field Photometry and Cluster Fiducial Sequences in ugriz. *ApJS*, 179: 326–354, December 2008. doi: 10.1086/592090.

L. Anderson, É. Aubourg, S. Bailey, F. Beutler, V. Bhardwaj, M. Blanton, A. S. Bolton, J. Brinkmann, J. R. Brownstein, A. Burden, et al. The clustering of galaxies in the SDSS-III Baryon Oscillation Spectroscopic Survey: baryon acoustic oscillations in the Data Releases 10 and 11 Galaxy samples. *Mon. Not. Roy. Astron. Soc.*, 441:24–62, June 2014. doi: 10.1093/mnras/stu523.

M. Arnaud, G. W. Pratt, R. Piffaretti, H. Böhringer, J. H. Croston, and E. Pointecouteau. The universal galaxy cluster pressure profile from a

representative sample of nearby systems (REXCESS) and the Y_{SZ} - M_{500} relation. *A&A*, 517:A92, July 2010. doi: 10.1051/0004-6361/200913416.

D. Baade, K. Meisenheimer, O. Iwert, J. Alonso, T. Augusteijn, J. Beletic, H. Bellemann, W. Benesch, A. Böhm, H. Böhnhardt, et al. The Wide Field Imager at the 2.2-m MPG/ESO telescope: first views with a 67-million-facette eye. *The Messenger*, 95:15–16, March 1999.

N. A. Bahcall and R. M. Soneira. The spatial correlation function of rich clusters of galaxies. *ApJ*, 270:20–38, July 1983. doi: 10.1086/161094.

I. Baraffe, A. Heger, and S. E. Woosley. On the Stability of Very Massive Primordial Stars. *ApJ*, 550:890–896, April 2001. doi: 10.1086/319808.

G. A. Barrick, J. Ward, and J.-C. Cuillandre. Persistence and charge diffusion in an E2V CCD42-90 deep-depletion CCD. In *Society of Photo-Optical Instrumentation Engineers (SPIE) Conference Series*, volume 8453, July 2012. doi: 10.1117/12.926409.

M. Bartelmann and P. Schneider. Weak gravitational lensing. *Phys. Rep.*, 340:291–472, January 2001. doi: 10.1016/S0370-1573(00)00082-X.

R. Bender, I. Appenzeller, A. Böhm, N. Drory, K. J. Fricke, A. Gabasch, J. Heidt, U. Hopp, K. Jäger, M. Kümmel, et al. The FORS Deep Field: Photometric Data and Photometric Redshifts. In S. Cristiani, A. Renzini, and R. E. Williams, editors, *Deep Fields*, page 96, 2001. doi: 10.1007/10854354_18.

R. Bender, J. Kormendy, M. E. Cornell, and D. B. Fisher. The Cluster Velocity Dispersion of the Abell 2199 cD Halo of NGC 6166. *ArXiv e-prints*, November 2014.

E. Bertin and S. Arnouts. SExtractor: Software for source extraction. *A&AS*, 117:393–404, June 1996.

A. Bindel. Atmospheric Transmission on the Wendelstein Obseratory. Master's thesis, Ludwig-Maximilians-Universität München, October 2011.

S. Borgani and A. Kravtsov. Cosmological Simulations of Galaxy Clusters. *Advanced Science Letters*, 4:204–227, February 2011. doi: 10.1166/asl.2011.1209.

D. R. V. Buckley and A. J. Longmore. The distance to M13 via a subdwarf fit in the optical-infrared colour-magnitude plane. *Mon. Not. Roy. Astron. Soc.*, 257:731–736, August 1992.

P. Carvalho, G. Rocha, and M. P. Hobson. A fast Bayesian approach to discrete object detection in astronomical data sets - PowellSnakes I. *Mon. Not. Roy. Astron. Soc.*, 393:681–702, March 2009. doi: 10.1111/j.1365-2966.2008.14016.x.

P. Carvalho, G. Rocha, M. P. Hobson, and A. Lasenby. PowellSnakes II: a fast Bayesian approach to discrete object detection in multi-frequency astronomical data sets. *Mon. Not. Roy. Astron. Soc.*, 427:1384–1400, December 2012. doi: 10.1111/j.1365-2966.2012.22033.x.

F. Castelli, R. G. Gratton, and R. L. Kurucz. Notes on the convection in the ATLAS9 model atmospheres. *A&A*, 318:841–869, February 1997.

A. Cavaliere and R. Fusco-Femiano. X-rays from hot plasma in clusters of galaxies. *A&A*, 49:137–144, May 1976.

A. W. J. Cousins. VRI standards in the E regions. 81:25, 1976.

K. S. Dawson, D. J. Schlegel, C. P. Ahn, S. F. Anderson, É. Aubourg, S. Bailey, R. H. Barkhouser, J. E. Bautista, A. Beifiori, A. A. Berlind, et al. The Baryon Oscillation Spectroscopic Survey of SDSS-III. *AJ*, 145:10, January 2013. doi: 10.1088/0004-6256/145/1/10.

S. Dodelson. *Modern cosmology*. Academic Press. ISBN 0-12-219141-2, 2003, XIII + 440 p., 2003.

E. Donoso, C. Li, G. Kauffmann, P. N. Best, and T. M. Heckman. Clustering of radio galaxies and quasars. *Mon. Not. Roy. Astron. Soc.*, 407:1078–1089, September 2010. doi: 10.1111/j.1365-2966.2010.16907.x.

A. G. Doroshkevich, M. I. Khlopov, R. A. Sunyaev, A. S. Szalay, and I. B. Zeldovich. Cosmological impact of the neutrino rest mass. *Annals of the New York Academy of Sciences*, 375:32–42, December 1981. doi: 10.1111/j.1749-6632.1981.tb33688.x.

T. Eichner, S. Seitz, S. H. Suyu, A. Halkola, K. Umetsu, A. Zitrin, D. Coe, A. Monna, P. Rosati, C. Grillo, et al. Galaxy Halo Truncation and Giant

Arc Surface Brightness Reconstruction in the Cluster MACSJ1206.2-0847. *ApJ*, 774:124, September 2013. doi: 10.1088/0004-637X/774/2/124.

A. Einstein. Die Grundlage der allgemeinen Relativitätstheorie. *Annalen der Physik*, 354:769–822, 1916. doi: 10.1002/andp.19163540702.

D. J. Eisenstein and W. Hu. Baryonic Features in the Matter Transfer Function. *ApJ*, 496:605–614, March 1998. doi: 10.1086/305424.

D. J. Eisenstein, D. H. Weinberg, E. Agol, H. Aihara, C. Allende Prieto, S. F. Anderson, J. A. Arns, É. Aubourg, S. Bailey, E. Balbinot, et al. SDSS-III: Massive Spectroscopic Surveys of the Distant Universe, the Milky Way, and Extra-Solar Planetary Systems. *AJ*, 142:72, September 2011. doi: 10.1088/0004-6256/142/3/72.

A. Finoguenov, L. Guzzo, G. Hasinger, N. Z. Scoville, H. Aussel, H. Böhringer, M. Brusa, P. Capak, N. Cappelluti, A. Comastri, et al. The XMM-Newton Wide-Field Survey in the COSMOS Field: Statistical Properties of Clusters of Galaxies. *ApJS*, 172:182–195, September 2007. doi: 10.1086/516577.

A. Friedmann. Über die Krümmung des Raumes. *Zeitschrift fur Physik*, 10: 377–386, 1922. doi: 10.1007/BF01332580.

M. Fukugita, T. Ichikawa, J. E. Gunn, M. Doi, K. Shimasaku, and D. P. Schneider. The Sloan Digital Sky Survey Photometric System. *AJ*, 111: 1748, April 1996. doi: 10.1086/117915.

L. Girardi, E. K. Grebel, M. Odenkirchen, and C. Chiosi. Theoretical isochrones in several photometric systems. II. The Sloan Digital Sky Survey ugriz system. *A&A*, 422:205–215, July 2004. doi: 10.1051/0004-6361:20040250.

M. D. Gladders and H. K. C. Yee. The Red-Sequence Cluster Survey. I. The Survey and Cluster Catalogs for Patches RCS 0926+37 and RCS 1327+29. *ApJS*, 157:1–29, March 2005. doi: 10.1086/427327.

N. Y. Gnedin and J. P. Ostriker. Reionization of the Universe and the Early Production of Metals. *ApJ*, 486:581–598, September 1997.

K. M. Górski, E. Hivon, A. J. Banday, B. D. Wandelt, F. K. Hansen, M. Reinecke, and M. Bartelmann. HEALPix: A Framework for High-Resolution Discretization and Fast Analysis of Data Distributed on the Sphere. *ApJ*, 622:759–771, April 2005. doi: 10.1086/427976.

C. Gössl, R. Bender, F. Grupp, U. Hopp, F. Lang-Bardl, W. Mitsch, W. Altmann, A. Ayres, S. Clark, M. Hartl, et al. A 64 Mpixel camera for the Wendelstein Fraunhofer Telescope Nasmyth wide-field port: WWFI. In *Society of Photo-Optical Instrumentation Engineers (SPIE) Conference Series*, volume 7735, July 2010. doi: 10.1117/12.856432.

C. Gössl, R. Bender, M. Fabricius, U. Hopp, A. Karasz, R. Kosyra, and F. Lang-Bardl. Commissioning of the WWFI for the Wendelstein Fraunhofer Telescope. In *Society of Photo-Optical Instrumentation Engineers (SPIE) Conference Series*, volume 8446, September 2012. doi: 10.1117/12.926341.

C. A. Gössl and A. Riffeser. Image reduction pipeline for the detection of variable sources in highly crowded fields. *A&A*, 381:1095–1109, January 2002. doi: 10.1051/0004-6361:20011522.

Claus Gössl. *Finding Cepheid Variable Stars in Northern Dwarf Galaxies of the Local Group*. PhD thesis, Ludwig-Maximilians-Universität München, December 2007. URL `http://nbn-resolving.de/urn:nbn:de:bvb:19-79489`.

M. Gramann, N. A. Bahcall, R. Cen, and J. R. Gott. Large-scale motions in the universe: Using clusters of galaxies as tracers. *ApJ*, 441:449–457, March 1995. doi: 10.1086/175370.

D. Gruen, F. Brimioulle, S. Seitz, C.-H. Lee, J. Young, J. Koppenhoefer, T. Eichner, A. Riffeser, V. Vikram, T. Weidinger, et al. Weak lensing analysis of RXC J2248.7-4431. *Mon. Not. Roy. Astron. Soc.*, 432:1455–1467, June 2013. doi: 10.1093/mnras/stt566.

D. Gruen, S. Seitz, F. Brimioulle, R. Kosyra, J. Koppenhoefer, C.-H. Lee, R. Bender, A. Riffeser, T. Eichner, T. Weidinger, et al. Weak lensing analysis of SZ-selected clusters of galaxies from the SPT and Planck surveys. *Mon. Not. Roy. Astron. Soc.*, 442:1507–1544, August 2014. doi: 10.1093/mnras/stu949.

Alan H. Guth. The Inflationary Universe: A Possible Solution to the Horizon and Flatness Problems. *Phys.Rev.*, D23:347–356, 1981. doi: 10.1103/PhysRevD.23.347.

A. J. S. Hamilton. Formulae for growth factors in expanding universes containing matter and a cosmological constant. *Mon. Not. Roy. Astron. Soc.*, 322:419–425, April 2001. doi: 10.1046/j.1365-8711.2001.04137.x.

D. S. Hayes and D. W. Latham. A rediscussion of the atmospheric extinction and the absolute spectral-energy distribution of VEGA. *ApJ*, 197:593–601, May 1975. doi: 10.1086/153548.

D. Herranz, J. L. Sanz, M. P. Hobson, R. B. Barreiro, J. M. Diego, E. Martínez-González, and A. N. Lasenby. Filtering techniques for the detection of Sunyaev-Zel'dovich clusters in multifrequency maps. *Mon. Not. Roy. Astron. Soc.*, 336:1057–1068, November 2002. doi: 10.1046/j.1365-8711.2002.05704.x.

H. Hoekstra, M. Franx, K. Kuijken, R. G. Carlberg, H. K. C. Yee, H. Lin, S. L. Morris, P. B. Hall, D. R. Patton, M. Sawicki, et al. Weak-Lensing Study of Low-Mass Galaxy Groups: Implications for Ω_m. *ApJ*, 548:L5–L8, February 2001. doi: 10.1086/318917.

U. Hopp, R. Bender, C. Goessl, W. Mitsch, H. Barwig, A. Riffeser, F. Lang, S. Wilke, C. Ries, F. Grupp, et al. Improving the Wendelstein Observatory for a 2m-class telescope. In *Society of Photo-Optical Instrumentation Engineers (SPIE) Conference Series*, volume 7016, July 2008. doi: 10.1117/12.787071.

U. Hopp, R. Bender, F. Grupp, H. Barwig, C. Gössl, F. Lang-Bardl, W. Mitsch, H. Thiele, P. Aniol, M. Schmidt, et al. The compact, low scattered-light 2m Wendelstein Fraunhofer Telescope. In *Society of Photo-Optical Instrumentation Engineers (SPIE) Conference Series*, volume 7733, July 2010. doi: 10.1117/12.856461.

E. Hubble. A Relation between Distance and Radial Velocity among Extra-Galactic Nebulae. *Proceedings of the National Academy of Science*, 15: 168–173, March 1929. doi: 10.1073/pnas.15.3.168.

O. Iwert, D. Baade, A. Balestra, A. Baruffolo, A. Bortolussi, F. Christen, C. Cumani, S. Deiries, M. Downing, C. Geimer, et al. The OmegaCAM

16K x 16K CCD detector system for the ESO VLT Survey Telescope (VST). In *Society of Photo-Optical Instrumentation Engineers (SPIE) Conference Series*, volume 6276, July 2006. doi: 10.1117/12.671599.

J. Janesick and T. Elliott. History and Advancement of Large Array Scientific CCD Imagers. In S. B. Howell, editor, *Astronomical CCD Observing and Reduction Techniques*, volume 23 of *Astronomical Society of the Pacific Conference Series*, page 1, 1992.

J.R. Janesick. *Scientific Charge-Coupled Devices*. Spie Press Monograph, Pm83. Society of Photo Optical, 2001. ISBN 9780819436986. URL `http://books.google.de/books?id=rkgBkbDie7kC`.

F. Jansen, D. Lumb, B. Altieri, J. Clavel, M. Ehle, C. Erd, C. Gabriel, M. Guainazzi, P. Gondoin, R. Much, et al. XMM-Newton observatory. I. The spacecraft and operations. *A&A*, 365:L1–L6, January 2001. doi: 10.1051/0004-6361:20000036.

A. Jenkins, C. S. Frenk, S. D. M. White, J. M. Colberg, S. Cole, A. E. Evrard, H. M. P. Couchman, and N. Yoshida. The mass function of dark matter haloes. *Mon. Not. Roy. Astron. Soc.*, 321:372–384, February 2001. doi: 10.1046/j.1365-8711.2001.04029.x.

H. L. Johnson and W. W. Morgan. Fundamental stellar photometry for standards of spectral type on the revised system of the Yerkes spectral atlas. *ApJ*, 117:313, May 1953. doi: 10.1086/145697.

M. H. Jones and R. J. A. Lambourne. *An Introduction to Galaxies and Cosmology*. June 2004.

N. Kaiser. Evolution and clustering of rich clusters. *Mon. Not. Roy. Astron. Soc.*, 222:323–345, September 1986.

M. Kerscher, I. Szapudi, and A. S. Szalay. A Comparison of Estimators for the Two-Point Correlation Function. *ApJ*, 535:L13–L16, May 2000. doi: 10.1086/312702.

M. Kilbinger, C. Bonnett, and J. Coupon. athena: Tree code for second-order correlation functions, February 2014. Astrophysics Source Code Library.

M. Kodric, A. Riffeser, U. Hopp, S. Seitz, J. Koppenhoefer, R. Bender, C. Goessl, J. Snigula, C.-H. Lee, C.-C. Ngeow, et al. Properties of M31. II. A Cepheid Disk Sample Derived from the First Year of PS1 PAndromeda Data. *AJ*, 145:106, April 2013. doi: 10.1088/0004-6256/145/4/106.

B. P. Koester, T. A. McKay, J. Annis, R. H. Wechsler, A. Evrard, L. Bleem, M. Becker, D. Johnston, E. Sheldon, R. Nichol, et al. A MaxBCG Catalog of 13,823 Galaxy Clusters from the Sloan Digital Sky Survey. *ApJ*, 660: 239–255, May 2007. doi: 10.1086/509599.

E. Komatsu, J. Dunkley, M. R. Nolta, C. L. Bennett, B. Gold, G. Hinshaw, N. Jarosik, D. Larson, M. Limon, L. Page, et al. Five-Year Wilkinson Microwave Anisotropy Probe Observations: Cosmological Interpretation. *ApJS*, 180:330–376, February 2009. doi: 10.1088/0067-0049/180/2/330.

E. Komatsu, K. M. Smith, J. Dunkley, C. L. Bennett, B. Gold, G. Hinshaw, N. Jarosik, D. Larson, M. R. Nolta, L. Page, et al. Seven-year Wilkinson Microwave Anisotropy Probe (WMAP) Observations: Cosmological Interpretation. *ApJS*, 192:18, February 2011. doi: 10.1088/0067-0049/192/2/18.

J. Koppenhoefer, R. P. Saglia, L. Fossati, Y. Lyubchik, M. Mugrauer, R. Bender, C.-H. Lee, A. Riffeser, P. Afonso, J. Greiner, et al. A hot Jupiter transiting a mid-K dwarf found in the pre-OmegaCam Transit Survey. *Mon. Not. Roy. Astron. Soc.*, 435:3133–3147, November 2013. doi: 10.1093/mnras/stt1512.

J. Koppenhofer and T. Henning. Results from the Pan-Planets Observing Campaign 2010. In *American Astronomical Society Meeting Abstracts #218*, May 2011.

J. Kormendy and R. Bender. A Revised Parallel-sequence Morphological Classification of Galaxies: Structure and Formation of S0 and Spheroidal Galaxies. *ApJS*, 198:2, January 2012. doi: 10.1088/0067-0049/198/1/2.

R. Kosyra, C. Gössl, U. Hopp, F. Lang-Bardl, A. Riffeser, R. Bender, and S. Seitz. The 64 Mpixel wide field imager for the Wendelstein 2m telescope: design and calibration. *Experimental Astronomy*, 38:213–248, November 2014. doi: 10.1007/s10686-014-9414-1.

R. Kosyra, D. Gruen, S. Seitz, A. Mana, E. Rozo, E. Rykoff, A. Sanchez, and R. Bender. Environment-based selection effects of Planck clusters. *Mon. Not. Roy. Astron. Soc.*, 452:2353–2366, September 2015. doi: 10.1093/mnras/stv1362.

R. Kurucz. ATLAS9 Stellar Atmosphere Programs and 2 km/s grid. *ATLAS9 Stellar Atmosphere Programs and 2 km/s grid. Kurucz CD-ROM No. 13. Cambridge, Mass.: Smithsonian Astrophysical Observatory, 1993.*, 13, 1993.

R. L. Kurucz. Model atmospheres for G, F, A, B, and O stars. *ApJS*, 40: 1–340, May 1979. doi: 10.1086/190589.

A. U. Landolt. UBV photoelectric sequences in the celestial equatorial Selected Areas 92-115. *AJ*, 78:959, November 1973. doi: 10.1086/111503.

A. U. Landolt. UBVRI photometric standard stars around the celestial equator. *AJ*, 88:439–460, March 1983. doi: 10.1086/113329.

A. U. Landolt. UBVRI photometric standard stars in the magnitude range 11.5-16.0 around the celestial equator. *AJ*, 104:340–371, July 1992. doi: 10.1086/116242.

A. U. Landolt. UBVRI Photometric Standard Stars Around the Celestial Equator: Updates and Additions. *AJ*, 137:4186–4269, May 2009. doi: 10.1088/0004-6256/137/5/4186.

S. D. Landy and A. S. Szalay. Bias and variance of angular correlation functions. *ApJ*, 412:64–71, July 1993. doi: 10.1086/172900.

D. Larson, J. Dunkley, G. Hinshaw, E. Komatsu, M. R. Nolta, C. L. Bennett, B. Gold, M. Halpern, R. S. Hill, N. Jarosik, et al. Seven-year Wilkinson Microwave Anisotropy Probe (WMAP) Observations: Power Spectra and WMAP-derived Parameters. *ApJS*, 192:16, February 2011. doi: 10.1088/0067-0049/192/2/16.

C.-H. Lee, A. Riffeser, J. Koppenhoefer, S. Seitz, R. Bender, U. Hopp, C. Gössl, R. P. Saglia, J. Snigula, W. E. Sweeney, et al. PAndromeda - First Results from the High-cadence Monitoring of M31 with Pan-STARRS 1. *AJ*, 143:89, April 2012. doi: 10.1088/0004-6256/143/4/89.

A. Lewis and A. Challinor. 21cm angular-power spectrum from the dark ages. *Phys. Rev. D*, 76(8):083005, October 2007. doi: 10.1103/PhysRevD.76.083005.

A. Mantz, S. W. Allen, D. Rapetti, and H. Ebeling. The observed growth of massive galaxy clusters - I. Statistical methods and cosmological constraints. *Mon. Not. Roy. Astron. Soc.*, 406:1759–1772, August 2010. doi: 10.1111/j.1365-2966.2010.16992.x.

P. Marigo, L. Girardi, C. Chiosi, and P. R. Wood. Zero-metallicity stars. I. Evolution at constant mass. *A&A*, 371:152–173, May 2001. doi: 10.1051/0004-6361:20010309.

I.S. McLean. *Electronic Imaging in Astronomy: Detectors and Instrumentation*. Springer Praxis Books / Astronomy and Planetary Sciences. Springer, 2008. ISBN 9783540765820. URL `http://books.google.de/books?id=FGHhZf-k8SkC`.

J.-B. Melin, J. G. Bartlett, and J. Delabrouille. Catalog extraction in SZ cluster surveys: a matched filter approach. *A&A*, 459:341–352, November 2006. doi: 10.1051/0004-6361:20065034.

H. J. Mo and S. D. M. White. An analytic model for the spatial clustering of dark matter haloes. *Mon. Not. Roy. Astron. Soc.*, 282:347–361, September 1996.

A. Monna, S. Seitz, N. Greisel, T. Eichner, N. Drory, M. Postman, A. Zitrin, D. Coe, A. Halkola, S. H. Suyu, et al. CLASH: z ˜6 young galaxy candidate quintuply lensed by the frontier field cluster RXC J2248.7-4431. *Mon. Not. Roy. Astron. Soc.*, 438:1417–1434, February 2014. doi: 10.1093/mnras/stt2284.

P. Murdin. *Encyclopedia of astronomy and astrophysics*. 2001.

J. F. Navarro, C. S. Frenk, and S. D. M. White. A Universal Density Profile from Hierarchical Clustering. *ApJ*, 490:493–508, December 1997.

A. von der Linden, A. Mantz, S. W. Allen, D. E. Applegate, P. L. Kelly, R. G. Morris, A. Wright, M. T. Allen, P. R. Burchat, D. L. Burke, et al. Robust weak-lensing mass calibration of Planck galaxy clusters. *Mon. Not.*

Roy. Astron. Soc., 443:1973–1978, September 2014. doi: 10.1093/mnras/stu1423.

H. Nyquist. Certain topics in telegraph transmission theory. 47:617–644, May 1928. doi: 10.1109/T-AIEE.1928.5055024.

J. B. Oke and J. E. Gunn. Secondary standard stars for absolute spectrophotometry. *ApJ*, 266:713–717, March 1983. doi: 10.1086/160817.

J. A. Peacock. *Cosmological Physics*. pp. 704. ISBN 052141072X. Cambridge University Press., January 1999.

S. Perlmutter, G. Aldering, M. della Valle, S. Deustua, R. S. Ellis, S. Fabbro, A. Fruchter, G. Goldhaber, D. E. Groom, I. M. Hook, et al. Discovery of a supernova explosion at half the age of the universe. *Nat*, 391:51, January 1998. doi: 10.1038/34124.

R. Piffaretti, M. Arnaud, G. W. Pratt, E. Pointecouteau, and J.-B. Melin. The MCXC: a meta-catalogue of x-ray detected clusters of galaxies. *A&A*, 534:A109, October 2011. doi: 10.1051/0004-6361/201015377.

Planck Collaboration, P. A. R. Ade, N. Aghanim, C. Armitage-Caplan, M. Arnaud, M. Ashdown, F. Atrio-Barandela, J. Aumont, H. Aussel, C. Baccigalupi, et al. Planck 2013 results. XXIX. Planck catalogue of Sunyaev-Zeldovich sources. *ArXiv e-prints*, March 2013a.

Planck Collaboration, P. A. R. Ade, N. Aghanim, C. Armitage-Caplan, M. Arnaud, M. Ashdown, F. Atrio-Barandela, J. Aumont, C. Baccigalupi, A. J. Banday, et al. Planck 2013 results. VI. High Frequency Instrument data processing. *ArXiv e-prints*, March 2013b.

Planck Collaboration, P. A. R. Ade, N. Aghanim, C. Armitage-Caplan, M. Arnaud, M. Ashdown, F. Atrio-Barandela, J. Aumont, C. Baccigalupi, A. J. Banday, et al. Planck 2013 results. XII. Component separation. *ArXiv e-prints*, March 2013c.

Planck Collaboration, P. A. R. Ade, N. Aghanim, C. Armitage-Caplan, M. Arnaud, M. Ashdown, F. Atrio-Barandela, J. Aumont, C. Baccigalupi, A. J. Banday, et al. Planck 2013 results. XX. Cosmology from Sunyaev-Zeldovich cluster counts. *ArXiv e-prints*, March 2013d.

Planck Collaboration, N. Aghanim, C. Armitage-Caplan, M. Arnaud, M. Ashdown, F. Atrio-Barandela, J. Aumont, C. Baccigalupi, A. J. Banday, R. B. Barreiro, et al. Planck 2013 results. II. Low Frequency Instrument data processing. *ArXiv e-prints*, March 2013e.

Planck Collaboration, P. A. R. Ade, N. Aghanim, C. Armitage-Caplan, M. Arnaud, M. Ashdown, F. Atrio-Barandela, J. Aumont, C. Baccigalupi, A. J. Banday, et al. Planck 2013 results. XVI. Cosmological parameters. *A&A*, 571:A16, November 2014. doi: 10.1051/0004-6361/201321591.

M. Postman, L. M. Lubin, J. E. Gunn, J. B. Oke, J. G. Hoessel, D. P. Schneider, and J. A. Christensen. The Palomar Distant Clusters Survey. I. The Cluster Catalog. *AJ*, 111:615, February 1996. doi: 10.1086/117811.

W. H. Press and P. Schechter. Formation of Galaxies and Clusters of Galaxies by Self-Similar Gravitational Condensation. *ApJ*, 187:425–438, February 1974. doi: 10.1086/152650.

Derek J Raine and Edward G Thomas. *An introduction to the science of cosmology*. Astronomy and Astrophysics. IOP, Bristol, 2001.

K. Reif, G. Klink, P. Müller, and H. Poschmann. High Precision "Bonn Shutters" for the largest CCD Mosaic Cameras. *Astronomische Nachrichten*, 326:666–+, August 2005.

Y. Rephaeli. Cosmic microwave background comptonization by hot intracluster gas. *ApJ*, 445:33–36, May 1995. doi: 10.1086/175669.

J. Rhodes, A. Leauthaud, C. Stoughton, R. Massey, K. Dawson, W. Kolbe, and N. Roe. The Effects of Charge Transfer Inefficiency (CTI) on Galaxy Shape Measurements. *PASP*, 122:439–450, April 2010. doi: 10.1086/651675.

A. G. Riess, A. V. Filippenko, P. Challis, A. Clocchiatti, A. Diercks, P. M. Garnavich, R. L. Gilliland, C. J. Hogan, S. Jha, R. P. Kirshner, et al. Observational Evidence from Supernovae for an Accelerating Universe and a Cosmological Constant. *AJ*, 116:1009–1038, September 1998. doi: 10.1086/300499.

A. Riffeser, S. Seitz, and R. Bender. The M31 Microlensing Event WeCAPP-GL1/POINT-AGAPE-S3: Evidence for a MACHO Component in the

Dark Halo of M31? *ApJ*, 684:1093–1109, September 2008. doi: 10.1086/590072.

A. Riffeser, S. Seitz, and R. Bender. PAndromeda - A Dedicated Deep Survey of M31 with Pan-STARRS 1. In *American Astronomical Society Meeting Abstracts #218*, May 2011.

H. P. Robertson. Kinematics and World-Structure. *ApJ*, 82:284, November 1935. doi: 10.1086/143681.

P. Rosati, S. Borgani, and C. Norman. The Evolution of X-ray Clusters of Galaxies. *ARA&A*, 40:539–577, 2002. doi: 10.1146/annurev.astro.40.120401.150547.

E. Rozo and E. S. Rykoff. redMaPPer II: X-Ray and SZ Performance Benchmarks for the SDSS Catalog. *ApJ*, 783:80, March 2014. doi: 10.1088/0004-637X/783/2/80.

E. Rozo, E. S. Rykoff, J. G. Bartlett, and J. B. Melin. redMaPPer III: A Detailed Comparison of the Planck 2013 and SDSS DR8 RedMaPPer Cluster Catalogs. *ArXiv e-prints*, January 2014.

V. C. Rubin and W. K. Ford, Jr. Rotation of the Andromeda Nebula from a Spectroscopic Survey of Emission Regions. *ApJ*, 159:379, February 1970. doi: 10.1086/150317.

E. S. Rykoff, B. P. Koester, E. Rozo, J. Annis, A. E. Evrard, S. M. Hansen, J. Hao, D. E. Johnston, T. A. McKay, and R. H. Wechsler. Robust Optical Richness Estimation with Reduced Scatter. *ApJ*, 746:178, February 2012. doi: 10.1088/0004-637X/746/2/178.

E. S. Rykoff, E. Rozo, M. T. Busha, C. E. Cunha, A. Finoguenov, A. Evrard, J. Hao, B. P. Koester, A. Leauthaud, B. Nord, et al. redMaPPer. I. Algorithm and SDSS DR8 Catalog. *ApJ*, 785:104, April 2014. doi: 10.1088/0004-637X/785/2/104.

K. Sato. First-order phase transition of a vacuum and the expansion of the Universe. *Mon. Not. Roy. Astron. Soc.*, 195:467–479, May 1981.

D. Schaerer. On the properties of massive Population III stars and metal-free stellar populations. *A&A*, 382:28–42, January 2002. doi: 10.1051/0004-6361:20011619.

E. F. Schlafly and D. P. Finkbeiner. Measuring Reddening with Sloan Digital Sky Survey Stellar Spectra and Recalibrating SFD. *ApJ*, 737:103, August 2011. doi: 10.1088/0004-637X/737/2/103.

D. J. Schlegel, D. P. Finkbeiner, and M. Davis. Maps of Dust Infrared Emission for Use in Estimation of Reddening and Cosmic Microwave Background Radiation Foregrounds. *ApJ*, 500:525, June 1998. doi: 10.1086/305772.

P. Schneider and C. Seitz. Steps towards nonlinear cluster inversion through gravitational distortions. 1: Basic considerations and circular clusters. *A&A*, 294:411–431, February 1995.

C. Seitz and P. Schneider. Steps towards nonlinear cluster inversion through gravitational distortions II. Generalization of the Kaiser and Squires method. *A&A*, 297:287, May 1995.

C. Seitz and P. Schneider. Steps towards nonlinear cluster inversion through gravitational distortions. III. Including a redshift distribution of the sources. *A&A*, 318:687–699, February 1997.

M. Sereno, S. Ettori, and L. Moscardini. CoMaLit - II. The scaling relation between mass and Sunyaev-Zel'dovich signal for Planck selected galaxy clusters. *ArXiv e-prints*, July 2014.

R. K. Sheth and A. Diaferio. Peculiar velocities of galaxies and clusters. *Mon. Not. Roy. Astron. Soc.*, 322:901–917, April 2001. doi: 10.1046/j.1365-8711.2001.04202.x.

R. K. Sheth and G. Tormen. Large-scale bias and the peak background split. *Mon. Not. Roy. Astron. Soc.*, 308:119–126, September 1999. doi: 10.1046/j.1365-8711.1999.02692.x.

J. Silk. Cosmic Black-Body Radiation and Galaxy Formation. *ApJ*, 151:459, February 1968. doi: 10.1086/149449.

J. Silk. *Horizons of Cosmology*. Templeton Press. p. 208., 2009.

S. Singh. *The Origin of the Universe*. Harper Perennial. p. 560., 2005.

P. F. Spinelli, S. Seitz, M. Lerchster, F. Brimioulle, and A. Finoguenov. Weak-lensing mass estimates of galaxy groups and the line-of-sight contamination. *Mon. Not. Roy. Astron. Soc.*, 420:1384–1404, February 2012. doi: 10.1111/j.1365-2966.2011.20126.x.

Z. Staniszewski, P. A. R. Ade, K. A. Aird, B. A. Benson, L. E. Bleem, J. E. Carlstrom, C. L. Chang, H.-M. Cho, T. M. Crawford, A. T. Crites, et al. Galaxy Clusters Discovered with a Sunyaev-Zel'dovich Effect Survey. *ApJ*, 701:32–41, August 2009. doi: 10.1088/0004-637X/701/1/32.

I. Suhhonenko and M. Gramann. The rms peculiar velocity of galaxy clusters for different cluster masses and radii. *Mon. Not. Roy. Astron. Soc.*, 339: 271–279, February 2003. doi: 10.1046/j.1365-8711.2003.06175.x.

R. A. Sunyaev and I. B. Zeldovich. The velocity of clusters of galaxies relative to the microwave background - The possibility of its measurement. *Mon. Not. Roy. Astron. Soc.*, 190:413–420, February 1980.

R. A. Sunyaev and Y. B. Zeldovich. The Observations of Relic Radiation as a Test of the Nature of X-Ray Radiation from the Clusters of Galaxies. *Comments on Astrophysics and Space Physics*, 4:173, November 1972.

J. Tinker, A. V. Kravtsov, A. Klypin, K. Abazajian, M. Warren, G. Yepes, S. Gottlöber, and D. E. Holz. Toward a Halo Mass Function for Precision Cosmology: The Limits of Universality. *ApJ*, 688:709–728, December 2008. doi: 10.1086/591439.

J. L. Tinker, B. E. Robertson, A. V. Kravtsov, A. Klypin, M. S. Warren, G. Yepes, and S. Gottlöber. The Large-scale Bias of Dark Matter Halos: Numerical Calibration and Model Tests. *ApJ*, 724:878–886, December 2010. doi: 10.1088/0004-637X/724/2/878.

J. L. Tonry, S. Isani, and P. Onaka. The PS1 Gigapixel Camera. In *American Astronomical Society Meeting Abstracts*, volume 39 of *Bulletin of the American Astronomical Society*, page 807, December 2007.

J. Tumlinson, J. M. Shull, and A. Venkatesan. Cosmological Reionization by the First Stars: Evolving Spectra of Population III. In P. Crowther, editor, *Hot Star Workshop III: The Earliest Phases of Massive Star Birth*, volume 267 of *Astronomical Society of the Pacific Conference Series*, page 433, October 2002.

K. Umetsu, T. Broadhurst, A. Zitrin, E. Medezinski, and L.-Y. Hsu. Cluster Mass Profiles from a Bayesian Analysis of Weak-lensing Distortion and Magnification Measurements: Applications to Subaru Data. *ApJ*, 729:127, March 2011. doi: 10.1088/0004-637X/729/2/127.

A. Vikhlinin, A. V. Kravtsov, R. A. Burenin, H. Ebeling, W. R. Forman, A. Hornstrup, C. Jones, S. S. Murray, D. Nagai, H. Quintana, et al. Chandra Cluster Cosmology Project III: Cosmological Parameter Constraints. *ApJ*, 692:1060–1074, February 2009. doi: 10.1088/0004-637X/692/2/1060.

A. G. Walker. On Milne's Theory of World-Structure. *Proceedings of the London Mathematical Society*, 90:2–42, 1937.

D. Weinberg, D. Bard, K. Dawson, O. Dore, J. Frieman, K. Gebhardt, M. Levi, and J. Rhodes. Facilities for Dark Energy Investigations. *ArXiv e-prints*, September 2013.

M. Weisskopf. The Chandra X-ray Observatory (CXO). In C. Kouveliotou, J. Ventura, and E. van den Heuvel, editors, *The Neutron Star - Black Hole Connection*, page 477, 2001.

S. D. M. White, C. S. Frenk, and M. Davis. Clustering in a neutrino-dominated universe. *ApJ*, 274:L1–L5, November 1983. doi: 10.1086/184139.

M. G. Yates, L. Miller, and J. A. Peacock. The cluster environments of powerful, high-redshift radio galaxies. *Mon. Not. Roy. Astron. Soc.*, 240: 129–166, September 1989.

S. Zaroubi. The Epoch of Reionization. In T. Wiklind, B. Mobasher, and V. Bromm, editors, *Astrophysics and Space Science Library*, volume 396 of *Astrophysics and Space Science Library*, page 45, 2013. doi: 10.1007/978-3-642-32362-1_2.

Y. B. Zeldovich and R. A. Sunyaev. The Interaction of Matter and Radiation in a Hot-Model Universe. *Ap&SS*, 4:301–316, July 1969. doi: 10.1007/BF00661821.

A. Zitrin, P. Rosati, M. Nonino, C. Grillo, M. Postman, D. Coe, S. Seitz, T. Eichner, T. Broadhurst, S. Jouvel, et al. CLASH: New Multiple Images

Constraining the Inner Mass Profile of MACS J1206.2-0847. *ApJ*, 749:97, April 2012. doi: 10.1088/0004-637X/749/2/97.

Acknowledgements

I would like to thank my supervising professor, Ralf Bender, for giving me the opportunity to work on two very exciting projects and for constantly supporting me during the course of this thesis. I enjoyed working in Ralf Bender's group from the first to the last day (and even after that). I would also like to thank Ulrich Hopp, my thesis advisor in the WWFI project, for aiding me with great ideas and his availability and guidance. I thank Stella Seitz, my thesis advisor in the SZ selection effect project, for all her support, her ideas and all the helpful discussions.
Special thanks to Claus Gössl, for all the guidance he gave me, especially in the early phase of my work, when I was an unexperienced newcomer. Without the help from Claus I would never have made it that far. I would like to express my gratitude to Daniel Gruen, who helped me especially in the final phase of my thesis with many suggestions and extensive discussions. I also thank Eduardo Rozo, not only for providing to me the RedMaPPer catalog, but also for constantly supporting me with new ideas.
I would like to thank Annalisa Mana for all the fruitful discussions we had and for her assistance during the final phase of my work. I acknowledge the assistance of Ben Hoyle concerning the Healpix software.
Furthermore I thank Florian Lang-Bardl for his support with the WWFI mechanics. Arno Riffeser helped me with several issues in the commissioning phase of the WWFI and I thank him for doing so. I acknowledge Johannes Koppenhoefer's aid in solving some problems in the data reduction process. I also would like to thank my fellow PhD-students Natascha Greisel, Mihael Kodric, Christian Obermeier, Oliver Friedrich and Markus Rau for many useful discussions.